

QUANTITATIVE FLUORESCENCE MOLECULAR TOMOGRAPHY: ALGORITHMS,
SIMULATIONS, AND PHANTOM/IN VIVO EXPERIMENTS

By

YIYONG TAN

A DISSERTATION PRESENTED TO THE GRADUATE SCHOOL
OF THE UNIVERSITY OF FLORIDA IN PARTIAL FULFILLMENT
OF THE REQUIREMENTS FOR THE DEGREE OF
DOCTOR OF PHILOSOPHY

UNIVERSITY OF FLORIDA

2010

© 2010 Yiyong Tan

To my parents, wife and daughter

ACKNOWLEDGMENTS

I would like to take this chance to convey my gratitude to all those people who have helped me complete this thesis.

Firstly, I am profoundly indebted to my supervisor and mentor Prof. Huabei Jiang. He carefully chose the projects and tailored them to my interest and capacity. Prof. Jiang was always present to listen to me and help me stay in right and most efficiency track. With his encouragements and instructions, I exceeded expectation I set for myself and built my foundation and confidence for my future research career. I will forever be grateful to have been a Ph.D. student of Prof. Jiang.

I would also like to thank Prof. Johannes (Hans) van Oostrom, Prof. David Gilland and Prof. Jorg Peters for being on my committee and guiding my thesis progress. I learned a lot from their professional instructions and academic courses.

I am very thankful to the collaborators on this thesis project: Prof. Lily Yang in Surgery Department of Emory University, Prof. Lei Zhou from Cancer/Genetics Center of Univ. of Florida and Dr. Steven L. Ponder from Imaging Diagnostic Systems Inc. It was their efforts that facilitated the application and highlighted the significance of this thesis.

Finally, I want to thank Dr Qizhi Zhang, Dr. Zhen Yuan and Dr. Lei Yao whose tireless efforts and help made possible much of what appears in this thesis. I learned a lot from my labmates, and I thank all the lab members for their help and constructive discussion.

TABLE OF CONTENTS

	<u>page</u>
ACKNOWLEDGMENTS.....	4
LIST OF TABLES.....	7
LIST OF FIGURES.....	8
ABSTRACT	10
CHAPTER	
1 INTRODUCTION	12
Principle of Fluorescence.....	12
Fluorescent Dye.....	13
Fluorescence Measurement	13
Sensing Devices.....	14
Data Acquisition Techniques	15
Fluorescence Molecular Tomography (FMT)	17
Theory and Algorithm	17
Forward problem.....	18
Inverse problem	20
Experimental System	22
Macro-scale FMT experimental systems	22
Meso-scale FMT experimental systems.....	23
Hybrid system with other imaging methodology.....	25
Applications.....	26
Whole-body <i>in vivo</i> fluorescence imaging	26
Brain imaging	26
Clinical applications	27
The Aims, Novelty, Significance and Contents of the Dissertation	28
2 FMT ALGORITHM IMPLEMENTATION AND SIMULATIONS.....	32
Diffusion Equation Based Method.....	33
Algorithm	33
Simulation.....	35
Radiative Transfer Equation (RTE) Based Method.....	35
Algorithm	35
Simulation.....	39
DOT Guided FMT	39
Algorithm	40
Simulation.....	42

3	EXPERIMENTAL SYSTEM AND METHOD	47
	Experimental System	47
	Shape Extraction for Arbitrarily Shaped Objects	49
	Camera Calibration	49
	Multi Camera Calibrations	51
	Visual Hull Method	52
	Free Space Data Extraction Model	54
	Detector Model	54
	Source Model	55
	Implementation in FMT System	56
4	PHANTOM EXPERIMENTS	66
	Regular Shaped Objects	67
	2D Experiments	70
	3D Experiments	71
	Arbitrarily Shaped Objects	71
5	APPLICATION IN A MOUSE MODEL	80
	Introduction	80
	Method and Experiments	82
	3D DOT Reconstruction of Mice	83
	Quantification of Cy 5.5 –ATF Labeled Tumor Cell	83
	Evaluation of Affinity	85
	Conclusions	87
6	APPLICATION IN A DROSOPHILA PUPA MODEL	91
	Static Fluorophore Concentration Imaging	93
	Cy5.5 Microtube Imaging	93
	DsRed Whole Body Imaging	94
	Dynamic DsRed Concentration Imaging	95
	Dynamic measurement of DNA accessibility in live animals via FMT	96
	Fluorescence Recovery after Photobleaching (FRAP) and FMT	97
7	CONCLUSIONS	106
	LIST OF REFERENCES	109
	BIOGRAPHICAL SKETCH	122

LIST OF TABLES

<u>Table</u>		<u>page</u>
4-1	Optical properties of the embedded “organs” and the background used in the experiments.....	74

LIST OF FIGURES

<u>Figure</u>	<u>page</u>
2-1	Diffusion approximation based FMT simulation for centimeter scale. A) Reconstructed bar target B) Reconstructed two cylinder targets: pink dots indicate exact position. 45
2-2	RTE based FMT reconstruction at different target depths. Green circle indicates the exact size and position of the target. 45
2-3	2D simulation comparison between FMT without A) and with B) DOT guidance 46
3-1	DOT guided FMT experiment system..... 58
3-2	Graphic user interface of the system 59
3-3	Coordinates system definition: top view from observe point above the sample stage and Y axis direction is from paper internal to outside. 60
3-4	Use calibrated CCD model parameters and universe world coordinate of grids to predict pixel values of corners in the image. 60
3-5	Visual hull scheme demonstration..... 61
3-7	Sources (red dots) and detectors (blue dots) of different projections. 62
3-8	Lambert's cosine law 63
3-9	Scattering geometry for a diffusive object of volume V surrounded by air for free space model..... 63
3-10	Photon density model of source on the air/sample interface 64
3-11	Outline of experimental procedures..... 65
4-1	Photograph of the CCD based CW FMT system..... 74
4-2	Reconstructed μ_a , μ'_s , and $\mu_{a \rightarrow m}$ images for a representative experimental case..... 75
4-3	Reconstructed $\mu_{a \rightarrow m}$ values in the target with and without DOT recovered μ_a and μ'_s distributions when different ICG concentration was used..... 76
4-4	Reconstructed 3D images for a representative case (ICG concentration in the target= $1 \mu M$). 77

4-5	Arbitrarily shaped phantom experiment. A) Phantom and imaging system. Inclusion is the arbitrarily phantom. B) Raw boundary signal	77
4-6	Exact positions of the targets in the finite element mesh A), and reconstructed μ_a B) , μ'_s C), and $\mu_{a \rightarrow m}$ D) images for a representative case (ICG concentration= $1 \mu M$).....	78
4-7	Reconstructed $\mu_{a \rightarrow m}$ values in the fluorescent targets with and without DOT guidance when different ICG concentration was used.....	79
5-1	Mouse in Experiment.....	88
5-2	Reconstructed 3D μ_a and μ'_s images of a typical mouse (mm^{-1}): (a) μ_a image (b) μ'_s image	88
5-3	Recovered 3D FMT images from a mouse.....	89
5-4	Comparison of signal intensity of the mammary tumor in the mice received uPAR-targeted NIR-830-ATF-IONPs and non-targeted NIR-830-MSA-IONP (with ATF vs without ATF)..	89
5-5	Detection of local recurrent mammary tumor and lung metastasis using reconstructed 3D images of FMT method and NIR-830-ATF peptide optical imaging probes.....	90
6-1	A pupa in experiment.....	100
6-2	Comparative Cy5.5 tube experiment of the diffusion and RTE based FMT reconstruction for a microtube embedded pupa.	101
6-3	3D view of reconstructed Cy 5.5 microtube in the pupa.	101
6-4	Reconstructed <i>in vivo</i> FMT (top row a-f) , <i>in vitro</i> confocal microscope (bottom row a-d) and epifluorescence microscope (bottom row e & f) images: Column a, b, c and d: transverse slices ; Column e and f : sagittal slices.	102
6-5	3D FMT tomography of 15 stages during the pupation development.	102
6-6	Microscope images of pupa (shell removed) in early stage.....	103
6-7	Quantifying the change of DNA accessibility in live animals with FMT and FRAP.....	104
7-1	Workflow framework of the dissertation.....	108

Abstract of Dissertation Presented to the Graduate School
of the University of Florida in Partial Fulfillment of the
Requirements for the Degree of Doctor of Philosophy

QUANTITATIVE FLUORESCENCE MOLECULAR TOMOGRAPHY: ALGORITHMS,
SIMULATIONS AND PHANTOM/IN VIVO EXPERIMENTS

By

Yiyong Tan

December 2010

Chair: Huabei Jiang
Major: Biomedical Engineering

A novel method for quantitative fluorescence molecular tomography (FMT) is developed in this thesis research, including image reconstruction algorithms and imaging hardware. Numerical simulations and phantom experiments are performed to test and validate the implemented reconstruction software and experimental system. Both macro- and meso-scale animal experiments are conducted to evaluate the developed quantitative FMT method.

The image reconstruction algorithms are implemented in the framework of finite element method, while the experimental system is constructed using a non-contact, multi-angle transmission scheme. Shape-from-silhouette based volume carving approach is used to render the 3D models of the actual samples. With a free-space light propagation model, the readout from the CCD is converted into the photon density normal to sample surface in order to match the model-based tomographic reconstruction.

Depending on the sample size, light propagation in biological tissue is described with two different models. For macro-scale objects, a diffusion equation based FMT

reconstruction algorithm is implemented. For meso-scale objects, a radiative transfer equation (RTE) based FMT reconstruction algorithm is adopted. In particular, diffuse optical tomography (DOT) guided FMT reconstruction method is developed to improve the quantification of image reconstruction. The method utilizes measurements at both the excitation and emission wavelengths to reconstruct fluorophore absorption coefficient, the absorption coefficient, and the reduced scattering coefficient in turbid media. Simulations and phantom experiments using targets containing indocyanine green (ICG) indicate that with the optical property distribution reconstructed by DOT, the qualitative and quantitative accuracy of the recovered fluorophore absorption coefficient is improved significantly over that without such *a priori* knowledge.

The applications are demonstrated using both macro- and meso-scale animals. The macro-scale animal experiments are conducted using a mouse model containing a near-infrared (NIR) fluorophore-magnetic nanoparticle hybrid probe which allows the studies of tumor cell quantification and affinity. The meso-scale animal experiments are performed using a *Drosophila* pupae model for dynamic monitoring of the red fluorescent protein (DsRed) reporter. The DsRed is an indicator of stem cell stress-induced death events in *Drosophila* pupae. The *in vivo* FMT results obtained are cross-validated with fluorescence and confocal microscopy using *in vitro* samples.

The reconstructed results presented suggest that the DOT guided FMT method described in this thesis provides a promising noninvasive tool for *in vivo* quantitative tomographic molecular imaging.

CHAPTER 1 INTRODUCTION

Fluorescent molecules are extremely valuable tools in biological research, preclinical study and clinical diagnosis. Fluorescence can be used to analyze the regulation and expression of genes, to locate proteins in cells and tissues, to follow metabolic pathways, to map the tumor, to reveal neuron activity and to study the location, migration, communication of cells. Fluorescence molecular tomography (FMT), as a novel method to obtain *in vivo* information of fluorescent probe in whole-body small animals under natural state instead of cells in culture dishes and slides, has transferred from pure numerical simulations to a fast evolving approach for real *in vivo* experiments and preclinical applications in the past ten years. Thanks to extensive fluorescent probe research, new signal acquisition techniques and its unique *in vivo* depth penetration compared to traditional widely-used *in vitro* fluorescence microscope, FMT receives more and more attentions and becomes a promising tool for small animal imaging.¹⁻⁵ Pilot clinical research using indocyanine green (ICG) for the breast cancer diagnosis and brain blood volume monitor have also been reported.^{6, 7}

Principle of Fluorescence

Different from incandescence resulted from high temperature, fluorescence is induced by excitation light instead and produces very little heat. For this reason fluorescence has also been referred to as "cold light" with exterior excitation. Bioluminescence, which is self emitting and requires no exterior excitation, is another well known "cold light".

In the standard model of molecules, the electrons occupy orbits and energy levels. A molecule that absorbs light will result in that electrons are moved into a higher energy

orbit states. All these excited electronic states are unstable, and later the electrons will lose absorbed energy and fall back to lower energy states. Most absorbed energy is transferred to heat in form of vibrations within the molecule, but a small portion of electrons emit part of the absorbed energy as photons. These emitted photons are so called fluorescence.

Fluorescent Dye

Recently, bio-compatible fluorophore in the visible and near-infrared spectral bands have been developed with stunning speed: organic dyes such as carbocyanines, fluorescein derivatives and tetrapyrroles, inorganic molecules including lanthanide chelates, various artificial made inorganic quantum dots, hairpin shaped oligonucleotide molecular beacons, protein fluorescent dye (YFP, GFP, DsRed derivatives etc) and so on. Especially, quantum dots, the artificially made inorganic semiconductor crystal, recently receives increased attention as tunable fluorophores, because their emission spectra can be tweaked by design the size of the nanocrystal, and can be excited using a monochromatic source while provide desired spectrum of emission. Study also shows quantum dots can increase anisotropy factor contrast as well.⁸ Moreover, most fluorophore can be bound into any desired carrier such as ligand, aptamer, nanoparticles and micro-bubbles to have desired function and enhanced specificity.

Fluorescence Measurement

On the other hand, advances in fluorescence sensing techniques and acquisition approach enable high quality non-invasively *in vivo* fluorescence imaging. Photomultiplier Tube (PMT), Photodiode and charge-coupled device (CCD) are three widely used light sensing techniques. Fluorescence acquisition techniques have also been evolved to new generations: confocal microscope, multi-photon microscope, time-

correlated single photon counting (TCSPC), laser scanning microscopy, full spectrum filterless fluorescent microscope and planar fluorescence imaging systems.

Sensing Devices

PMT based systems have been widely used for past two decades and gradually been replaced by high performance photodiode based system in the last ten years. PMT is a high sensitive and high gain light detector providing current output directly proportional to light intensity. PMT is quite expensive and need careful maintenance: the vacuum in the PMT will degrade over time; the high voltage supply need regular checking as contaminants attracted to terminals can cause current leakage and failure. PMTs are susceptible to shocks and vibration and can be easily damaged by overexposure light.

Photodiode is a semiconductor device containing a p-n structure for the detection of light. Light absorbed in the p-n structure generates a photocurrent. A Photodiode is a simple, robust, low cost, low voltage device and is less susceptible to shocks, movement and overexposure damages. Avalanche photodiode can also get high sensitive and quantum yield comparable to PMT, but it needs preamplifiers to obtain high gain and the detector area is usually 1mm*1mm which is much smaller than 1cm*1cm of PMT.

CCD becomes increasingly popular recently in optical imaging field to provide more boundary data and fast data acquisition time. Intensified CCD (ICCD) and Electron Multiplying CCD (EMCCD) are two major advancements for detect ultralow and ultrafast light signal. ICCD uses an image intensifier coupled to the CCD chip to increase the sensitivity down to single photon level and can capture nanosecond phenomena. Since readout and dark current noises are negligible, no cooling

component is needed for ICCDs. The image intensifier will bring distortion and amplify signal with high gain, so ICCD is only suitable to work at very low light. EMCCD technology is relative new and is introduced in 2000. EMCCDs unite the quantum efficiency of CCDs and the gain of ICCDs, so it can be used as a regular CCD or ICCD by controlling gain. The performance is depended on charge transfer and dark current noises, so EMCCDs must be strongly cooled ($<-60^{\circ}\text{C}$) and milliseconds scale read out time is necessary for best performance.

Data Acquisition Techniques

Traditionally, biological fluorescence imaging has been performed in microscopy of *in vitro* specimens stained with fluorescent dyes. The rich biology information provided by fluorescent dyes has promoted the advance of microscope and in return is much better understood with unprecedented resolution and clarity. Microscopic techniques have also been applied *in vivo* to study skin or other exposed structures using confocal microscope, multiphoton microscope, Time-Correlated Single Photon Counting (TCSPC) Laser Scanning Microscopy and full spectrum filterless fluorescent microscope. However, these approaches are typically limited by the depth limit (50 – 600um), and have been restricted to observe subsurface fluorescence.

Confocal microscope enables the reconstruction of three-dimensional structures from the obtained photons of different focus depth by using a spatial pinhole to eliminate out-of-focus light from specimens. The increased resolution is at the cost of decreased signal intensity, so long exposures are often required. The imaging depth of confocal microscope is around 200 micrometers.

Multiple-photon absorption requires less energy of each photon with longer wave length which can greatly decrease the scattering effect and increase penetration depth.

The widely used multi-photon microscope is two photon fluorescent microscope (2PFM) which enhances the penetration depth and at the same time provides clarity image up to 500um depth and allows imaging 1mm deeper regions for low scattering sample.⁹ Photo-bleaching and photo-damage are limited to the focal region in 2PFM while in 1PFM the whole light path is affected. Although 2PFM has a lower resolution and requires special excitation lasers, it provides longer observation time, deeper tissue penetration, more efficient light detection and less phototoxicity.

Hyperspectral fluorescence microscopy (HFM) is an emerging field based on hyperspectral or multispectral imaging concepts. HFM reveals fluorescence emission associated spectrum profile of biological samples for each pixel by using tunable optical filter like liquid crystal tunable filters (LCTF) or acousto-optic tunable filter (AOTF). The HFM has been used to differentiate the contributions of autofluorescence from exogenous fluorescent signals present in the sample and greatly increase signal/noise ratio. Wavelength scanning provides full spectrum information of fluorophore dye, while the extra scan time greatly decreases temporal resolution. Snapshot techniques have been developed for hyperspectral imaging to capture the spatial and spectral information simultaneously.¹⁰

The fluorescence lifetime is obtained by measurement of the time delays between the excitation pulse and the fluorescence photons. Time-Correlated Single Photon Counting (TCSPC) laser scanning microscope contains information on both the fluorescence lifetime and the fluorescent intensity for each pixel. The fluorescence lifetime is the average time the molecules remain in excited state before emitting a photon and can indicate fluorophore dynamic state under different environments.

As a widely used tool for *in vivo* imaging of small animals, conventional planar fluorescence imaging systems create a two-dimensional fluorescence distribution projectional map.¹¹⁻¹³ When signal is relative strong, the planar method can reveal 2D location of fluorophore in living small animal. However, it is difficult to recover the depth, size, and fluorophore concentration accurately from the projection images.

Fluorescence Molecular Tomography (FMT)

Fluorescence molecular tomography (FMT) can provide valuable *in vivo* information in living subjects with unparalleled depth penetration and accurate 3D localization.¹⁴ Unlike above described fluorescence measurement methods which usually imaging surface fluorophore, fluorescence molecular tomography can image fluorophore up to 5 centimeter deep. FMT images are reconstructed by an optimization process to minimize the discrepancy between theoretic computation and measured boundary fluorescence intensity distributions. FMT can provide cross-sectional or full three-dimensional (3D) images. Recently, FMT gradually becomes a promising tool for small animal *in vivo* imaging in preclinical research.¹⁻⁵ FMT enables researchers to rapidly and easily obtain tomographic images of *in vivo* biomarkers with various advantages such as unprecedented depth penetration, no invasive via NIR light, whole-body animal imaging and true quantification. Although quantitative accuracy and the resolution need further improvement, FMT is evolving with encouraging advances in resolution and quantitative accuracy.

Theory and Algorithm

Light propagation inside tissue is described based on scales of applications: Maxwell equations are the fundamental theory and are usually used at the microscale (micrometer) and scattering free situations; The radiative transport equation (RTE) is

the approximation of Maxwell equation under assumptions valid at the meso-scale (millimeter) with scattering and absorption heterogeneity; Diffusion equation is the approximation of RTE under assumptions valid at the macro-scale (centimeter). RTE can describe meso-scale and macro-scale, but from engineering point of view, it is impractical and unnecessary when diffusion approximate equation is accurate enough. Biological applications of fluorescence tomography are majorly in macro-scale like mice or rats, and extend recently in meso-scale samples as *Drosophila* pupae.

In radiative transport theory, the propagation of light through a biology tissue medium is formulated based on a conservation law that describes gains and losses of photons in different directions due to scattering and absorption. The diffusion approximation (DA) to the RTE is widely used in small animal applications due to its low computation cost and memory efficiency. The DA is valid when the reduced scattering coefficient is much larger than the absorption coefficient; the point of observation is far away from excitation source point. For both RTE and DA, the tomography algorithms are usually composed of two parts: forward problem and inverse problem.¹⁵

Forward problem

Forward Problem is to calculate light intensity distribution using known or assigned optical property distributions and light source. Forward solution is unique and accurate to predicate light intensity of any location on boundary or internal domain.

Analytical modeling solution. Green's functions provide a method to solve the diffusion equation or the RTE analytically. The Green's function method is accurate when the source is a spatial and temporal function whose induced light distribution can be solved by convolution. Analytical solutions only exist and is practical for simple homogeneous regular shaped objects.¹⁶

Statistical modeling techniques. *Monte Carlo* simulation-based modeling is the most commonly used statistical technique in optical tomography field and is often used as the “gold standard” to validate other techniques. *Monte Carlo* modeling uses a pseudo-random number generator to trace individual photon trajectories. Given enough photons, statistically valid propagation direction, photon diminish rule based on known absorption and reduced scattering coefficients, *Monte Carlo* modeling can reveal how many photons (light intensity) in any interested small volume region of the objects.

Numerical techniques for complex geometries. Finite element method (FEM) is a general technique which can be applied to any geometry. FEM is very suitable to model arbitrarily shaped objects and was first introduced into optical tomography by Arridge *et al.*^{17,18} and later introduced to frequency domain fluorescence molecular tomography.⁵ While FEM has become the standard method of choice for modeling complex domains in optical imaging, the finite difference method (FDM),^{19,20} finite volume method (FVM)²¹ and boundary element method (BEM)²² have also been used in various applications.

It is too computationally expensive to solve the RTE fully by numerical method in a practical application. The RTE can be solved using the P_N approximation,²³ by expansion into a rotated spherical harmonic basis²⁴ and by discrete ordinates approximation.²⁵ Discrete ordinates approximation solves the full RTE on a regular grid using FDM, FVM or FEM by specifying discrete directions of light propagation.

***A priori* information can greatly improve accuracy of forward problem.** One big trend in FMT is to plug *a priori* anatomical information and optical property into the forward problem to improve quantification accuracy. *A priori* information can be obtained

from MRI, CT, photoacoustic tomography (PAT), DOT and anatomy structure. The *a priori* information and the FMT images should be acquired simultaneously for accurate image registration, but MRI, CT and PAT methods all will add extra cost and complicate FMT system even bring extra system error and comprise image quality. Although MRI CT and PAT can provide better resolution of anatomical structure, DOT method requires zero extra effort and cost for existing FMT system. In addition, it provides complete quantitative absorption and reduced scattering coefficient distribution as *a priori* information which can be directly plugged into FMT algorithm.

Inverse problem

Inverse problem is a procedure to use actual observations to reconstruct the value of the characterizing parameters in the system under a defined model. Inverse problem is much more difficult to solve than forward problem because: (1) different spatial values distribution of the model parameters can have same boundary signals; (2) recovering the values of the model parameters may require analysis of a huge parameter combinations which result in more unknown parameter than known boundary observation; (3) inverse problems are typically ill-posed. A little bit of variation in measurement boundary data due to noise will result in significant changes in the reconstructed images. To stabilize this process, regularization of original data is always added into the reconstruction procedure. How much regularization to add is usually experimentally determined by finding a best tradeoff between robust solution and minimum artifacts due to alteration of original data. Therefore, inverse problems only find one of best solution instead of the unique correct solution and the solving process usual becomes an optimization problem to find best probabilistic solution. Three reconstruction algorithms are widely used for FMT inverse problems.

Algebraic reconstruction technique (ART) The Algebraic Reconstruction Technique (ART) is an iterative algorithm for the reconstruction of a two-dimensional image from a series of one-dimensional angular projections, and the method is already successful used in medical Computed Tomography (CT) scanning. Normalized Born method is used to account for optical heterogeneities inside reconstruction domain. In this method the fluorescent signal of each project is normalized with excitation signal of same projection before ART, which simplify experiment because the position-dependent coupling factors are canceled out. One disadvantage of normalized Born is the lost of absolute quantitative information and physics unit due to the normalization process of raw data before reconstruction. In addition, ART based reconstruction simplifies the scattering effect of excitation and emission light.^{26, 27}

Newton's optimization method. In mathematics, Newton's method is a very efficient approach to find roots of equations in one or more dimensions. It can also be used to find local maxima and local minima of functions, as these extrema are the roots of the derivative functions. Based on a set of coupled diffusion equations that describe the propagation of both excitation and fluorescence emission light in highly scattering media, the reconstruction algorithm is centered on Newton's iterative method where the update of variable is calculated based on Jacobian matrix consisting of the derivatives of boundary light intensity at each boundary observation node with respect to fluorescent yield or fluorescent lifetime.^{5,28} Truncated Newton's optimization scheme also demonstrated as a much faster method to handle large inverse problem.^{29, 30,33}

Bayesian framework probability based reconstruction. Bayesian estimation is an approach to the inverse problems that maximum likelihood estimation needs to be

found. It focuses on finding optimal solutions which also honestly includes error bars in the estimate. The general idea is to start with a constant likelihood function describing the experimenter's *a priori* knowledge, then the update of parameter and parameter covariance is estimated by adaptive extended Kalman filter (AEKF) . Bayesian framework is statistically strict and computationally efficient to provide a likelihood function of photon density with error estimation. Large 3-D optical imaging problems can be implemented within clinically practical computational resources by using automatic progressive parameter-reducing inverse zonation and estimation (APPRIZE) and data-driven zonation (DDZ).^{31,32, 33}

Experimental System

There are various methodologies to implement 3D FMT for different application requirements: the pulsed or continuous source, spatially modulated or multispectral illumination, time or frequency-resolved data and polarization or phase sensitive signal.¹³ Typical FMT systems for general purpose collect all boundary signals including highly scattering light to match RTE or diffusion model. Recently for special applications and much better resolution, some new FMT systems especially for meso-scale objects only selectively collect photons with certain scattering rule and theoretical model is also modified to match the data collection scheme. Since only fraction of photons are collected, the signal will be very weak and extra exposure time is required.

Marco-scale FMT experimental systems

Fluorescence Molecular Tomography (FMT) experiment system usually has scanning excitation sources on boundary and paired transmission detectors on opposite side or reflectance detectors on same side. It can be implemented using contact fiber optics or non contact CCD camera. The system can be frequency domain and

continuous wave for different applications. Non contact scheme is a nature choice for *in vivo* applications of arbitrary shaped objects, which is crucial for *in vivo* FMT to be a universal tool as MRI, CT and PET and become a standard medical imaging instrument.

Typical FMT has been implemented for various applications: Godavarty *et al.* described a 3D frequency domain reconstruction algorithm³³ suited for a gain modulated intensified CCD (ICCD) setup and succeed to reconstruct ICG concentration for a breast mimicking phantom using a Bayesian framework. Corlu *et al.* succeeded to use a CCD and optical fiber based continuous wave system to reconstruct ICG concentration of patient's breast using normalized finite element method. The system is a contact system need match fluid to enable regular shape reconstruction. Ntziachristos *et al.* presented a series of *in vivo* applications by using non contact CCD multi-projection transmission system with normalized Born method.³⁴⁻³⁶ Roy *et al.* demonstrated frequency domain based reflectance fluorescent tomography in phantom study.³⁷

Early photons travel preferentially along the shortest path connecting the photon source to the detectors and experience few scattering events compared with the diffuse photons in the medium. Therefore imaging with time-gated detection of early photons is used to reduce the amount of scattered photons contained in the measurements and could lead to better-defined forward problems and inverse reconstruction.³⁸⁻⁴⁰

Meso-scale FMT experimental systems

Recently some new techniques are developed for special applications. In these techniques, only part of scattering photons are collected on boundary, so usually these techniques provide better resolution and with fast reconstruction speed: Laminar optical tomography (LOT) collect scattering on chosen depth; Optical projection tomography

(OPT)²⁷ is good tool for less scattering applications. Early photons method only collects scattering photons within a time window. Single Scattering tomography collects scattering photons with certain angle.

Laminar optical tomography (LOT). LOT bridged the gap between micrometer and millimeter depth resolution, by combining optical tomographic techniques with a microscopy-based setup to allow imaging with 200um resolution over depths of 0–2.5 mm which surpasses the depth capabilities of optical coherence tomography but with a lower spatial resolution. LOT is also suited to spectroscopy when multiple narrowband sources are used.^{41, 42}

Optical projection tomography (OPT). OPT is a linear equation based reconstruction technique using a filtered back projection. The method is suitable for small samples with relatively low scattering. By rejecting multi scattering photons to fit directly CT reconstruction algorithm, OPT produces high-resolution 3D images of both fluorescent and nonfluorescent biological specimens with a thickness up to 15 millimeters. OPT microscopy allows high on-site temporal resolution in mapping the tissue distribution of RNA and protein expression in intact embryos or organs for developmental biology and gene function research.²⁷

Single scattering optical tomography (SSOT). SSOT, unlike early photon method, do not rely on time gating for separating single-scattered photons from strong scattered light. SSOT utilizes angularly selective intensity measurements to reconstruct the total attenuation coefficient of an inhomogeneous meso-scale regime medium. SSOT produces high-quality images even in relatively thick samples where the single-scattering approximation is expected to break down. So far SSOT is a optical

tomography technique and single scattering fluorescence tomography will be reported in near future.⁴³

Hybrid system with other imaging methodology

Commonly used imaging methodology for small animal includes positron emission tomography (PET), single photon emission computed tomography (SPECT), magnetic resonance imaging (MRI), ultrasound, X-ray computed tomography (CT) and hybrid system. The imaging systems for preclinical applications obtain higher resolution and detection sensitivity compared with their clinical counterparts because of smaller imaging domain and better penetration.

Standard imaging methods and FMT method can complement each other using either hardware approach (hybrid experimental system) or software approach (multi-methodology image registration). The hybrid system or multi-methodology imaging are usually for two purposes: 1 FMT has its unique advantage for *in vivo* animal imaging and can provide additional functional information for other methods such as high molecular specificity, nonionizing radiation, optical probe stability (no intensity decay over time like isotope) and the potential for simultaneous investigations of multiple targets using spectral probes without overlapped emission. 2 Other methods provide *a priori* information which improves the qualitative and quantitative accuracy of FMT. *A priori* information has been found to be particularly effective in improving the quantitative accuracy by guiding and constraining the FMT reconstruction algorithm. Hybrid FMT systems reported so far includes: FME/MRI,⁴⁴⁻⁴⁶ FMT/CT,^{47, 48} FMT/PET/CT,⁴⁹ FMT/Photoacoustic tomography (PAT).⁵⁰⁻⁵²

Applications

Over the past decade, *in vivo* Imaging systems for small animals have become increasingly popular. The imaging tool developed for small animal preclinical research includes: MRI, X-ray micro CT, Micro-PET, Micro-SPECT, Ultrasound, PAT, Optical Coherence Tomography (OCT) and Optical Tomography (Bioluminescence & fluorescence).

Fluorescence molecular tomography has high contrast, high specificity, and biggest reagent arsenal for almost every aspect of biology molecular events and has been widely used for fundamental biology research and preclinical research.^{11-13, 53-58}

Whole-body *in vivo* fluorescence imaging

Although *in vivo* tomography imaging allows visualization of biology in its intact and native physiological state, it is a technically challenging process for several reasons. First, thick and opaque animal tissue absorbs and scatters photons and generates strong autofluorescence, which obscures signal and deteriorates quantification. Second, fluorescent dye for complicated *in vivo* application requires biological stability (relative stable value of quantum yield), preferential accumulation at the intended target sites, and high imaging contrast specific to the targets. Third, fast metabolism wash out demands a restricted time window for experiments. Despite these difficulties, great progress is obtained in tumor mapping of murine tumor, lung carcinomas and breast cancer, chemotherapeutic effect monitoring, angiogenesis related vascular volume analysis and genes expression profiling identification.^{2, 4, 40, 59-67}

Brain imaging

The blood-brain barrier (BBB) is the separation between circulating blood and cerebrospinal fluid (CSF) maintained by the choroid plexus in the central nervous

system (CNS). Most commercial dyes are hydrophilic with huge molecular weight and cannot pass BBB: Cy55, ICG, Ca²⁺ indicator (fluo-4, calcium orange and crimson), voltage sensitive dye and enzyme indicator (with huge molecular weight) like ProSense. At present, the delivery of these dyes to brain is achieved only for research purpose with following approaches:

1. Invasive direct injection
2. Permeabilization of tight junctions
 - a. osmotic disruption (mannito
 - b. biochemical opening (RMP-7 Alkermes, histamine).
3. Focused ultrasound (FUS)-induced BBB opening

The dye usually should have a low molecular weight (~ 500) and high lipophilicity (logP 1-4, P=partition coefficient) to cross the blood-brain barrier (BBB) in sufficient amounts. To do noninvasive brain research, some dyes are designed and synthesized to pass BBB and succeed to facilitate *in vivo* applications: Tumor localization and treatment with nanoparticle NPCP-CTX-Cy5.5 and MPAP-Cy5.5; Alzheimer's disease mechanism study with nanoparticle (I-CQ-BCA NPs) and small commercial available dyes such as AOI987 (MW 410.1) and NIAD-4(MW 334).^{47, 68,69,70}

Clinical applications

The clinical applications of fluorescence tomography are even more challenge due to three reasons: Firstly, only one infrared dye (Indocyanine green, ICG) is approved by FDA for clinical usage. Secondly, depth is ten times deeper than small animals and signal is extreme weak compared to mouse experiments. Thirdly, it is hard to get approved for human experiments and patients also are not willing to have chemical fluorophore in body for research purpose. There are still very promising clinical research achievements in breast cancer and brain imaging field despite of those difficulties: Corlu *et al.* reported that it is possible to detect and reconstruct breast tumor fluorescence *in*

vivo with fluorescence molecular tomography. The large tumor contrast obtained with a non-targeted exogenous fluorophore (ICG) pictures a promising future as more molecularly targeted dyes get approved for clinical usage.⁷ Liebert *et al.* first demonstrate that exogenous ICG, introduced intravenously to healthy human volunteers, can be excited and detected noninvasively inside the brain.⁷¹

The Aims, Novelty, Significance and Contents of the Dissertation

The goal of this Ph.D. thesis research is to develop a non-contact 3D fluorescence molecular tomography (FMT) system (both hardware and software) for quantitative *in vivo* imaging of spatial distribution of fluorescent probes/reporters in both macro- and meso-scale animals. The goal is achieved through the completion of the following three major tasks:

Development of robust finite element based reconstruction algorithms for quantitatively accurate recovery of fluorescent concentrations for arbitrarily shaped animals in both macro- and meso-scale. Implementation of a practical experimental system for *in vivo* FMT of meso-scale animals. Realization of quantitative fluorescent imaging for *in vivo* animal applications.

The thesis summarizes all the results obtained during my graduate study and systematically describes the methods developed and their theoretical background.

Development of hardware and finite element based reconstruction algorithms for quantitative FMT. We made considerable effort to develop a robust easy-to-use FMT system for *in vivo* animal imaging. The novel features of this system includes: 1, an automatic system. The data flow from the acquisition of the raw signals to the 3D rendering of reconstructed images is streamlined: Raw data are evaluated with a computer algorithm for signal optimization; Initial state for reconstruction is

autotomatically chosen without the user's intervention; Reconstruction domain is determined by raw fluorescence intensity distribution and 3D representation settings are optimized to highlight the regions of interest (ROI). 2, Capability of imaging both macro- and meso-scale samples using the same hardware and software. The computer program automatically determines the method of processing the experiment data based on the dimension of the samples. 3, Multi-angle non contact measurements for arbitrarily shaped objects and automatic selection of source and detector positions based on the contour of the samples. The coupling coefficients of the free space calibration model are determined and validated through well controlled phantom experiments. 4, Fast computation and efficient memory management for FMT image reconstruction. 5, Compatible data formats for easy coregistration with other imaging modalities such as ICT or MRI.

Implementation of the RTE based reconstruction algorithm for dynamic FMT of meso-scale animals (*Drosophila pupae*). Light propagation in tissue is described in accordance of the sample size: Theoretical studies have shown that the RTE is the most accurate model for meso-scale imaging, but no experimental validation is reported in this regard. We implemented the RTE based model into our non contact FMT system with finite element based algorithm and first applied to FMT imaging of meso-scale animal like *Drosophila pupae*. We monitor DsRed distribution inside *Drosophila pupae* and the results are consistent with confocal slice images. The dynamic change of DsRed are also presented and validated by *in vitro* confocal and microscope session results. The major advantage of *in vivo* FMT over *in vitro* confocal microscope in dynamic monitor applications is that *in vivo* FMT can avoid sacrificing animals and

obtain more reliable information from the same animal over time without changing the experimental setting, thus increasing the statistical validity of the data by minimizing experimental variations. In addition, dynamic monitoring of the meso-scale animals can be realized only by FMT.

Realization of absolute quantitative fluorescent imaging. Currently most FMT methods are based on a linear algorithm and the assumption of uniform optical property distribution or the optical distribution obtained indirectly from other imaging methods like MRI, CT or Photoacoustic Tomography (PAT). These methods usually provide semi-quantitative analysis with arbitrarily units or quantitative analysis based on a calibration curve. We use finite element based diffuse optical tomography (DOT) guided FMT method to provide truly quantitative fluorescent images: DOT guided method provides a priori optical properties of tissue for quantitative analysis of FMT. The DOT guided FMT method is tested and validated by simulations, phantom experiments and mouse experiments. The results consistently show better quantification and image quality over other FMT methods.

This thesis consists of a total of seven chapters:

In Chapter 1, a brief review of fluorescent imaging and FMT is given. The principles of fluorescence light, fluorescent dyes, traditional fluorescent imaging methods and their recent developments are reviewed. For the newly emerging FMT method, the associated forward and inverse problems, hardware for both macro- and meso-scale imaging, and the preclinical applications are discussed.

In Chapter 2, image reconstruction algorithms based on both the diffusion equation and radiative transport equation are implemented using the finite element

method. In addition, the DOT guided FMT reconstruction algorithm is presented. Numerical simulations using all the implemented reconstruction algorithms are conducted.

In Chapter 3, the experimental system for FMT is described in detail. In addition, a method for contour extraction of arbitrarily shaped objects and a model of free space light propagation in non-contact geometry are discussed.

In Chapter 4, tissue-mimicking phantom experiments are used to validate the theoretical models presented in Chapter 2 and with the experimental system described in Chapter 3. Furthermore, the proposed DOT guided quantitative FMT method is tested and evaluated with phantom experiments.

In Chapter 5, Application of the reconstruction algorithms and imaging system described in Chapters 2 and 3 to macro-scale mouse imaging is presented. In these preclinical experiments, tumor-bearing mice containing NIR dye-ATF-nanoparticle probes are imaged. The FMT results obtained indicate that our method has the potential to become a useful tool for monitoring of tumor progression, detection of early stage cancer, chemotherapy evaluation, surgery guidance and drug delivery.

In Chapter 6, *In Vivo* application of the RTE based FMT method to monitoring fluorescent protein (DsRed) in meso-scale *Drosophila* pupae is given. Fluorescence recovery after photobleaching (FRAP) is studied for validating the findings from the dynamic FMT monitoring.

In Chapter 7, the overall conclusions from this thesis research and future directions are given.

CHAPTER 2 FMT ALGORITHM IMPLEMENTATION AND SIMULATIONS

Diffuse Optical Tomography (DOT) has demonstrated promising applications in biomedical imaging field. Examples include detection of cerebral hemorrhages,⁷² functional imaging of brain activity,^{73, 74} diagnosis of rheumatoid arthritis,^{75, 76} and cancer mapping.^{7, 77, 78} These applications rely on the fact that various disease processes and most physiological changes affect the optical properties of biological tissue. The optical properties are the absorption coefficient μ_a , the reduced scattering coefficient μ'_s . The differences in these optical properties between healthy and pathological tissues provide the contrast for optical tomography technology.⁷⁹ The contrast and selectivity of DOT are usually not satisfactory; therefore, exogenous fluorescent dye can greatly enhance contrast and selectivity. On the other hand, DOT reconstruction complements FMT by providing all optical information needed in FMT. We here implement the DOT guided FMT algorithm as a complete optical tomography method and investigate FMT applications in both macro-scale and meso-scale. For meso-scale modeling, RTE based algorithms is implemented; for macro-scale application, diffusion based algorithm is implemented.

Simulation is to model a real-life or hypothetical situation on a computer so that it can be studied to see how the system works in perfect conditions without any experimental errors. By changing optical variables, simulation can be made to predict boundary experimental signal and test inverse algorithms. Simulation also can optimize algorithms and experimental settings. A typical simulation procedure includes: 1, target size and variable value is predefined; 2, simulated experiment data is obtained through forward solutions and used as the input of reverse algorithms; 3, reconstructed targets

are compared to exact predefined targets; 4, change simulation condition (for example source, detector numbers and distribution) and repeat 1-3 to find best settings that can provide best conformity between predefined targets and reconstructed targets.

3D FMT finite element algorithm implementation is tested by numerical simulations in this chapter and phantoms in Chapter 3. Implementation of adjoint sensitive method algorithm, one dimension variable bandwidth storage strategy and fast solver for symmetric matrix dramatically reduce computation time and memory cost. In addition, as an improvement of methodology, we combined fluorescence molecular tomography (FMT) with diffuse optical tomography (DOT), which allows us to study the impact of heterogeneous optical property distribution on FMT and provide quantitative FMT.

Diffusion Equation Based Method

Algorithm

Our finite-element-based algorithms for both DOT and FMT have been described in detail.^{5, 80, 81} Here we outline the algorithms based on the following coupled diffusion equations that describe the propagation of excitation and emission light in tissue:

$$\nabla \cdot [D_x(r)\nabla\Phi_x(r)] - \mu_{a_x}(r)\Phi_x(r) + S_x(r) = 0 \quad (1)$$

$$\nabla \cdot [D_m(r)\nabla\Phi_m(r)] - \mu_{a_m}(r)\Phi_m(r) + \eta\mu_{a_{x \rightarrow m}}(r)\Phi_x(r) = 0 \quad (2)$$

where $\Phi_{x,m}$ is the photon density for excitation (subscript x) or emission light (subscript m), $D_{x,m}$ is the diffusion coefficient, $\mu_{a_{x,m}}$ is the absorption coefficient for excitation and emission light due to contributions from both non-fluorescing chromophores and fluorophores, and $\eta\mu_{a_{x \rightarrow m}}$ is the fluorescence quantum yield. $S_x(r)$ is

the excitation source term, which for a point source can be written as $S = S_0\delta(r - r_0)$, where S_0 is the source strength and $\delta(r - r_0)$ is the Dirac-delta function for a source centered at r_0 . The diffusion coefficient can be written as $D_{x,m} =$

$1/3(\mu_{a_{x,m}}(r) + \mu'_{s_{x,m}}(r))$ where $\mu'_{s_{x,m}}(r)$ is the reduced scattering coefficient.

In this study, we use the non-zero photon density or type III boundary conditions:

$-D_{x,m}\nabla\Phi_{x,m} \cdot \hat{n} = \alpha\Phi_{x,m}$, where \hat{n} is the unit normal vector to the boundary surface,

and α is the coefficient related to the internal reflection at the boundary. Making use of finite element discretization, we obtain the matrix representations of Eqs. (1) and (2)

and realize other derived matrix relationships through differentiation, which lead to a set of equations capable of inverse problem solution:

$$[A_{x,m}]\{\Phi_{x,m}\} = \{b_{x,m}\} \quad (3)$$

$$[A_{x,m}]\left\{\frac{\partial\Phi_{x,m}}{\partial\chi}\right\} = \left\{\frac{\partial b_{x,m}}{\partial\chi}\right\} - \left[\frac{\partial A_{x,m}}{\partial\chi}\right]\{\Phi_{x,m}\} \quad (4)$$

$$(\mathfrak{T}_{x,m}^T \mathfrak{T}_{x,m} + \lambda I)\Delta\chi = \mathfrak{T}_{x,m}^T (\Phi_{x,m}^o - \Phi_{x,m}^c) \quad (5)$$

where $(A_{x,m})_{ij} = \left\langle -D_{x,m}\nabla\psi_j\nabla\psi_i - \mu_{a_{x,m}}\psi_j\psi_i \right\rangle$, $(b_x)_i = -\langle S\psi_i \rangle + \alpha \sum_{j=1}^M (\Phi_x)_j \int \psi_j\psi_i ds$,

$(b_m)_i = -\left\langle \sum_{k=1}^k \eta\psi_k\mu_{a_{x \rightarrow m_k}} \sum_{j=1}^N (\Phi_x)_j\psi_j\psi_i \right\rangle + \alpha \sum_{j=1}^M (\Phi_m)_j \int \psi_j\psi_i ds$ and $\psi_{i,j,k}$ is a set of locally spatially

varying Lagrangian basis functions; χ expresses D_x , μ_{a_x} , or $\eta\mu_{a_{x \rightarrow m}}$; $\mathfrak{T}_{x,m}$ is the Jacobian

matrix consisting of the derivatives of $\Phi_{x,m}$ with respect to χ at each boundary

observation node. $\Delta\chi$ is the update vectors for the optical and fluorescent property

profiles; I is identity matrix; λ may be a scale or a diagonal matrix; $\Phi_{x,m}^o$ and $\Phi_{x,m}^c$ are the

observed and the computed excitation or emission photon density at the boundary sites,

respectively.

In FMT reconstruction, D_x, μ_{a_x} are known or treated as uniform when we calculate Φ_x in forward solution with Eqs (1). D_m, μ_{a_m} are known or treated as uniform as well. We plugged $D_{x,m}, \mu_{a_{x,m}}, \Phi_x$ and boundary Φ_m to reconstruct the only unknown $\eta\mu_{a_{x \rightarrow m}}$ in Eqs.(2) by using equation (3),(4),(5).

Simulation

For brief, we present two typical 3D FMT simulations as shown in Fig. 2-1. Fig. 2-1 A) is the reconstruction of a simulated bar target in a square background; Fig. 2-1 B) is the reconstruction of two simulated cylinder targets in a square background. The reconstruction results show correct value, shape and position of targets.

Radiative Transfer Equation (RTE) Based Method

Algorithm

The RTE in the steady-state for FMT can be described as following equations:

Excitation:

$$\left(\bar{\Omega} \cdot \nabla + \mu_{s_x}(\bar{r}) + \mu_{a_x}(\bar{r})\right)\varphi_x(\bar{r}, \bar{\Omega}) = \mu_{s_x}(\bar{r}) \int_{S^{n-1}} \varphi_x(\bar{r}, \bar{\Omega}') \Theta(\bar{\Omega}, \bar{\Omega}') d\bar{\Omega}' + q_x(\bar{r}, \bar{\Omega}), \quad (1)$$

Emission:

$$\left(\bar{\Omega} \cdot \nabla + \mu_{s_m}(\bar{r}) + \mu_{a_m}(\bar{r})\right)\varphi_m(\bar{r}, \bar{\Omega}) = \mu_{s_m}(\bar{r}) \int_{S^{n-1}} \varphi_m(\bar{r}, \bar{\Omega}') \Theta(\bar{\Omega}, \bar{\Omega}') d\bar{\Omega}' + \frac{1}{4\pi} \eta\mu_{a_{x \rightarrow m}}(\bar{r}) \varphi_x(\bar{r}, \bar{\Omega}) \quad (2)$$

where $\varphi_{x,m}(\bar{r}, \bar{\Omega})$ is the photon density for excitation (subscript x) or emission light (subscript m), $\mu_{s_{x,m}}(\bar{r})$ is scattering coefficient, $\mu_{a_{x,m}}(\bar{r})$ is the absorption coefficient for excitation or emission light due to contributions from both non-fluorescing chromophores and fluorophores respectively, and $\eta\mu_{a_{x \rightarrow m}}(\bar{r})$ is the fluorescent yield.

$\bar{\Omega} \in S^{n-1}$ denotes a unit vector in the direction of interest. Here S^{n-1} is the angular direction, n=2 or 3 denotes the physical domain which is considered isotropic in the

sense that the probability of scattering between two directions depends only on the relative angle between those directions. R is the spatial domain, and ∂R denotes its boundary. The kernel $\Theta(\bar{\Omega}, \bar{\Omega}')$ is the scattering phase function describing the probability density that a photon with an initial direction $\bar{\Omega}'$ will scatter to direction $\bar{\Omega}$. In this study we assume that the scattering phase function depends only on the angle between the incoming and outgoing directions, and thus

$$\Theta(\bar{\Omega}, \bar{\Omega}') = \Theta(\bar{\Omega} \cdot \bar{\Omega}'). \quad (3)$$

The two-dimensional Henyey-Greenstein scattering function, the most widely adopted and highly accurate phase function of scattering kernel for light propagation, is used here: ⁸²

$$\Theta(\bar{\Omega} \cdot \bar{\Omega}') = \frac{1}{2\pi} \frac{1 - g^2}{(1 + g^2 - 2g \cos \gamma)}. \quad (4)$$

where γ is the angle between the input direction $\bar{\Omega}'$ and output direction $\bar{\Omega}$. The anisotropy factor, g ($-1 < g < 1$), defines the shape of the probability density.

Considering the relatively homogenous optical properties and $\mu_s \gg \mu_a$ for early stage *Drosophila* (<4th day) pupae in our current study, g is set to zero for fast computation.

The boundary conditions (BC) for the RTE assume that no photons travel in an inward direction at the boundary ∂R , that is,

$$\varphi(\bar{r}, \bar{\Omega}) = 0, \quad \bar{\Omega} \cdot \hat{n} < 0 \text{ for all } \bar{r} \in \partial R \quad (5)$$

where \hat{n} is the outward unit normal on ∂S . The BC, also known as free surface BC, imply that once a photon escapes the domain it does not reenter it. The BC can be modified to include a boundary source $\varphi^o(\bar{r}, \bar{\Omega})$ at the source position $\varepsilon_i \subset \partial R$, and can be written as follows: ⁸³

$$\mathbf{q}_x(\bar{\mathbf{r}}, \bar{\Omega}) = \begin{cases} \varphi^o(\bar{\mathbf{r}}, \bar{\Omega}), & \mathbf{r} \in \cup_i \varepsilon_i \quad \bar{\Omega} \cdot \hat{\mathbf{n}} < 0 \\ 0, & \mathbf{r} \in \partial S \setminus \cup_i \varepsilon_i \quad \bar{\Omega} \cdot \hat{\mathbf{n}} < 0 \end{cases} \quad (6)$$

The solution to the RTE with the chosen boundary conditions is existent and unique. ⁸⁴

Making use of finite element discretization, we obtain the matrix representations of Eqs. (1) and (2) and realize other derived matrix relationships through differentiation, which leads to a set of equations capable of inverse problem solution:

$$[\mathbf{A}_{x,m}] \{\varphi_{x,m}\} = \{\mathbf{b}_{x,m}\} \quad (7)$$

$$[\mathbf{A}_{x,m}] \left\{ \frac{\partial \varphi_{x,m}}{\partial \chi} \right\} = \left\{ \frac{\partial \mathbf{b}_{x,m}}{\partial \chi} \right\} - \left[\frac{\partial \mathbf{A}_{x,m}}{\partial \chi} \right] \{\varphi_{x,m}\} \quad (8)$$

$$(\mathfrak{S}_{x,m}^T \mathfrak{S}_{x,m} + \lambda \mathbf{I}) \Delta \chi = \mathfrak{S}_{x,m}^T (\varphi_{x,m}^o - \varphi_{x,m}^c) \quad (9)$$

where

$$(\mathbf{A}_{x,m})_{ij} = \begin{aligned} & - \left[\int_{\mathbf{R}} \int_{S^{n-1}} \psi_j(\bar{\mathbf{r}}, \bar{\Omega}) \bar{\Omega} \cdot \nabla \psi_i(\bar{\mathbf{r}}, \bar{\Omega}) d\bar{\Omega} d\bar{\mathbf{r}} \right] \\ & + \left[\oint_{\partial \mathbf{R}} \int_{S^{n-1}} (\bar{\Omega} \cdot \hat{\mathbf{n}})_+ \psi_j(\bar{\mathbf{r}}, \bar{\Omega}) \psi_i(\bar{\mathbf{r}}, \bar{\Omega}) d\bar{\Omega} dS \right] \\ & + \left[\int_{\mathbf{R}} \int_{S^{n-1}} (\mu_a + \mu_s) \psi_j(\bar{\mathbf{r}}, \bar{\Omega}) \psi_i(\bar{\mathbf{r}}, \bar{\Omega}) d\bar{\Omega} d\bar{\mathbf{r}} \right] \\ & - \left[\int_{\mathbf{R}} \int_{S^{n-1}} \mu_s \int_{S^{n-1}} \Theta(\bar{\Omega} \cdot \bar{\Omega}') \varphi(\bar{\mathbf{r}}, \bar{\Omega}') d\bar{\Omega}' \psi_i(\bar{\mathbf{r}}, \bar{\Omega}) d\bar{\Omega} d\bar{\mathbf{r}} \right] \end{aligned} \quad (10)$$

$$(\mathbf{b}_x)_i = \left[\oint_{\partial \mathbf{R}} \int_{S^{n-1}} (\bar{\Omega} \cdot \hat{\mathbf{n}})_- \psi_j(\bar{\mathbf{r}}, \bar{\Omega}) \psi_i(\bar{\mathbf{r}}, \bar{\Omega}) d\bar{\Omega} dS \right] \varphi_j^o \quad (11)$$

$$(\mathbf{b}_m)_i = \int_{\mathbf{R}} \int_{S^{n-1}} \psi_i(\bar{\mathbf{r}}, \bar{\Omega}) \frac{1}{4\pi} \eta \mu_{a_x \rightarrow m}(\bar{\mathbf{r}}) \varphi_x(\bar{\mathbf{r}}, \bar{\Omega}) d\bar{\Omega} d\bar{\mathbf{r}} \quad (12)$$

$\psi_{i,j}$ is a set of locally spatially varying Lagrangian basis functions; χ expresses, μ_{s_x} , μ_{a_x} , or $\eta \mu_{a_x \rightarrow m}$; $\mathfrak{S}_{x,m}$ is the Jacobian matrix consisting of the derivatives of $\varphi_{x,m}$ with respect to χ at each boundary observation node. $\Delta \chi$ is the update vectors for the optical

or fluorescent property profiles; I is an identity matrix; λ may be a scale or a diagonal matrix; $\varphi_{x,m}^o$ and $\varphi_{x,m}^c$ are the observed and the computed excitation or emission photon density at the boundary sites, respectively.

In addition, $\varphi(\vec{r}, \vec{\Omega})$ needs to be expanded as the sum of coefficients multiplied by the Lagrangian basis function:

$$\varphi(\vec{r}, \vec{\Omega}) = \sum_{j=1}^N \psi_j(\vec{r}, \vec{\Omega}) \varphi_j = \sum_{nj=1}^{N_n} \sum_{mj=1}^{N_a} \psi_{nj}(\vec{r}) \psi_{mj}(\vec{\Omega}) \varphi_{nj,mj} \quad (13)$$

where $\psi_{nj}(\vec{r})$ and $\psi_{mj}(\vec{\Omega})$ are the nodal spatial and angular basis functions, $\varphi_{nj,mj}$ is the radiance at the spatial nodal point nj and direction mj , N_n is the number of spatial nodes of the mesh, and N_a is the number of angular directions.

The ray effect may disturb the standard FE-techniques when solving the RTE, since it can produce oscillating results or it can visually be seen as “photon rays” radiating from the source into the direction of the discretization angles.^{85, 86} To overcome the ray effect, the streamline diffusion modification (SDM) is used in the FE-solution of the RTE. In the SDM, the test function is written in the form $(\psi_j(\vec{r}, \vec{\Omega}) + \delta \vec{\Omega} \cdot \nabla \psi_j(\vec{r}, \vec{\Omega}))$ instead of the standard form of a test function $(\psi_j(\vec{r}, \vec{\Omega}))$. The parameter δ is the “smoothing” parameter which is a spatially varying constant that depends on the local absorption and scattering.⁸⁵

In this study, μ_s and μ_a were assumed as uniform and their values, $\mu_a = 0.005 \text{ mm}^{-1}$ and $\mu_s = 0.2 \text{ mm}^{-1}$, were obtained through an optimization scheme⁸⁷ $\varphi_x(\vec{r}, \vec{\Omega})$ was calculated by solving equation (7) (under subscript x). $\eta \mu_{a \rightarrow m}$ was reconstructed by iteratively solving Eqs. (7)-(9) (under subscript m) from presumably uniform initial

estimates until the difference between the measured and computed photon density at the emission wavelength is minimized.

The RTE based fluorescence inverse computation requires over a magnitude more memory and time than the diffusion equation based FMT, and it is usually realized through parallel computation. We have made an effort to realize the RTE based fluorescence inverse computation in a single personal computer by incorporating the following features into our algorithm: Element by element unsymmetric solver using hybrid BiCGStab(1) version to save memory⁸⁸ and one time fast computation of the Jacobian matrix using adjoint sensitivity method.⁸⁹

Simulation

Two-dimensional simulations were conducted to test the RTE reconstruction algorithm described above. The 2D mesh used has 1622 nodes (the direction, $m_j=16$). For the test geometry shown in Fig. 2-2, a total of 14 source and 55 detector positions were used. The initial value used for $\mu_{a_{x \rightarrow m}}$ was $1e-8/\text{mm}$ with the updating constrain of $\eta\mu_{a_{x \rightarrow m}} > 0$. The quantum efficiency η is set to be a constant value 0.016. With a 3GHz personal computer, the RTE based fluorescence reconstruction needed about 0.3 GB memory and 150 minutes to complete. The results are shown in Fig. 2-2. We see that the RTE based method can correctly reconstruct the size, position and $\mu_{a_{x \rightarrow m}}$ value ($1e-4/\text{mm}$) of the target ($R=80\mu\text{m}$) at different depth.

DOT Guided FMT

While exogenous fluorescent probes improve the contrast and selectivity of the targets of interest, unknown absorption coefficient (μ_a) and reduced scattering coefficient (μ'_s) distribution in tissue complicate fluorescent tomographic reconstruction

.^{90, 91} Theoretically, propagation of both excitation and fluorescent emission light in tissue is described by the coupled diffusion equations. The emission photon density is directly related to the excitation photon density, which in turn depends on the optical property distributions in tissue. In fact, the exogenous fluorescent probe itself in a relatively large target usually has strong absorption and becomes a significant heterogeneity affecting excitation photon density distribution.

In the approach, we directly reconstruct optical heterogeneities using DOT and apply reconstructed μ'_s and μ_a distributions to the FMT reconstruction. Both DOT and FMT reconstructions are conducted using an optical fiber free system based on a non-contact multi-angle transmission scheme, coupled with finite element reconstruction algorithms. Our simulation and experimental results suggest that the optical heterogeneous nature of the target itself especially when its size is relatively large must be considered for quantitatively correct FMT in the framework of finite element based reconstruction methods.

Algorithm

DOT guidance information is a natural way to improve the quantification and qualification of FMT. DOT method provides information on reduced scattering coefficient distribution, absorption distribution and excitation light distribution. All these distributions are the prerequisite for accurate fluorescence modeling and FMT reconstruction. The challenge of this algorithm is to get DOT reconstruction as accurate as possible, since incorrect reconstruction will bring in extra error propagation from DOT to FMT. Although DOT reconstruction error is inevitable due to experiment error and inverse procedure of DOT, due to our simulation and experimental results, DOT guidance information can

help improve the quantification and qualification of FMT reconstruction. In some case boundary artifacts, which defined as extra high value within 3 millimeter close to the boundary of DOT, will cause error in FMT. To overcome this issue, we assign background value to boundary artifacts when plugging into FMT reconstructions.

In our DOT guided FMT procedure, D_x and μ_{a_x} are reconstructed by iteratively solving Eqs. (3)-(5) (under subscript x) from presumably uniform initial estimates until the difference between the measured and computed photon density at the excitation wavelength is minimized. The recovered D_x and μ_{a_x} are then used to interpolate D_m and μ_{a_m} at the emission wavelength using optical property spectra available from the literature.¹⁹ Similar iterative procedure is applied to reconstruct $\eta\mu_{a_{x \rightarrow m}}$ with the interpolated D_m and μ_{a_m} in place in order to minimize the difference between the measured and computed photon density at the emission wavelength.

We note that the accuracy for obtaining quantitative recovery of absorption and reduced scattering coefficient is critical for the DOT guided FMT method presented here. We have made great efforts in improving our DOT reconstruction algorithm and experimental system to obtain accurate optical property reconstruction. It has been demonstrated in recent years by several groups including our own⁹²⁻⁹⁵ that quantitative reconstruction of both absorption and scattering coefficients is possible using CW DOT when *a priori* information coupled with effective normalization schemes are used. In our CW DOT method, in addition to the use of *a priori* information obtained by initial search based on raw experimental signal and normalization scheme, the hybrid regularization schemes of Marquardt and Tikhonov play an important role in combating the ill-posed problem involved.⁸⁷ Our previous phantom study shows that with DOT guidance,

statistically we can obtain better FMT reconstruction in mouse-mimicking phantom experiments.⁹⁶

Heterogeneity can also be addressed by normalized Born method and using *a priori* information from CT, MRI and PAT. Like low resolution disadvantage in DOT guided method, these approaches also have their own issues need to be solved for better performance. Using boundary excitation data to normalize emission data can reveal the heterogeneity distribution and cancel out boundary geometry effects, but it averages the heterogeneity effect and optical property distributions hidden inside boundary signal are not fully utilized. In addition, the heterogeneity of inside tumor or tissue adjacent to fluorophore will affect the fluorescent reconstruction most.

Fluorophore targeted tumor has very high heterogeneity, which cannot be recovered by boundary data. In some cases when boundary heterogeneities (moles, surgery scars and subdermal tumors) are high and the boundary data will not reveal internal heterogeneity and will bring extra error in internal FMT reconstruction. Although MRI, CT and PAT can provide better resolution of anatomical structure, DOT method requires zero extra effort and cost for existing FMT systems. In addition, it provides quantitative absorption and reduced scattering coefficient distribution as *a priori* information which can be directly plugged into FMT algorithm.

Simulation

Numerous simulation studies reported to date have shown that tissue optical property distribution does pose significant impact on fluorescent image reconstruction.

^{26, 31, 97-101} Experimental results using various FMT approaches were generally consistent with the simulation findings in presence of heterogeneity, although most reported FMT experiments were limited to homogeneous optical property approximation

or a *priori* optical property distribution,^{2, 4, 37, 80, 102} Soubret *et al.* described a normalized Born approximation approach and studied FMT image quality under optical heterogeneity using phantom and animal data.¹⁰³ Roy *et al.* investigated the impact of optical heterogeneity using a gradient-based constrained truncated Newton method.³⁷ Milstein *et al.* presented a phantom study in presence of optical heterogeneity with a Bayesian framework based FMT method.¹⁰¹ Hervé *et al.* reported improved FMT reconstruction using a normalized Born approximation approach with reconstructed μ_a distribution while assuming μ'_s is homogeneous.¹⁰⁴ We propose the FEM based DOT guided FMT for better quantitative accuracy and simulations mimicking experiment situations are administered.

Prior to the phantom experiments, we have conducted considerable numerical simulations using various ICG-containing target positions, and target-to-background contrast levels in terms of fluorophore concentration. These simulations have demonstrated that much improved image quality especially quantitative accuracy of the recovered $\mu_{a \rightarrow m}$ image can be obtained with *a priori* knowledge of the μ_a and μ'_s distributions, whereas in uniform optical property treatment the quality of the recovered fluorescence images are significantly degraded with overestimated target size, poor spatial resolution and underestimated value of recovered $\mu_{a \rightarrow m}$. Since the focus of the study is the phantom evaluation and preclinical applications, we just show a representative simulation case for brevity (Fig. 2-3), where the $\mu_{a \rightarrow m}$ image was reconstructed without (a) and with (b) *a priori* μ_a and μ'_s information. In this simulation, a 6mm diameter target was positioned at (-5, -6). The target had $\mu_a = 0.025/\text{mm}$, $\mu'_s = 2/\text{mm}$

and $\mu_{a_{x \rightarrow m}} = 0.02/\text{mm}$. The background had $\mu_a = 0.005/\text{mm}$, $\mu'_s = 1/\text{mm}$ and $\mu_{a_{x \rightarrow m}} = 4 \times 10^{-12}/\text{mm}$. we see that when *a priori* μ_a and μ'_s distributions are used, the $\mu_{a_{x \rightarrow m}}$ image is accurately reconstructed in terms of the size (estimated from the full width at half maximum (FWHM) of the fluorescent profiles), location and $\mu_{a_{x \rightarrow m}}$ value of the target, whereas when μ_a and μ'_s distributions are assumed uniform, the recovered target size is overestimated and the recovered $\mu_{a_{x \rightarrow m}}$ value of the target contains over 60% error compared to the exact value of 0.02/mm.

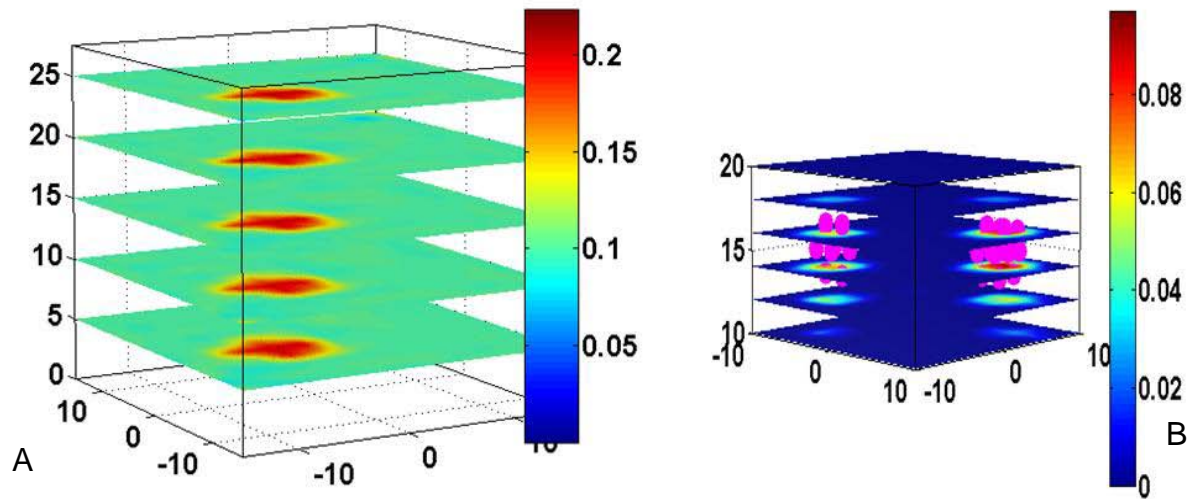


Figure 2-1. Diffusion approximation based FMT simulation for centimeter scale. A) Reconstructed bar target B) Reconstructed two cylinder targets: pink dots indicate exact position.

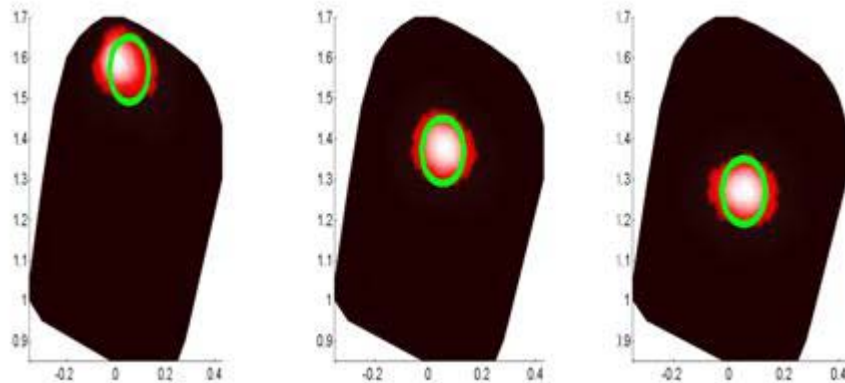


Figure 2-2. RTE based FMT reconstruction at different target depths. Green circle indicates the exact size and position of the target.

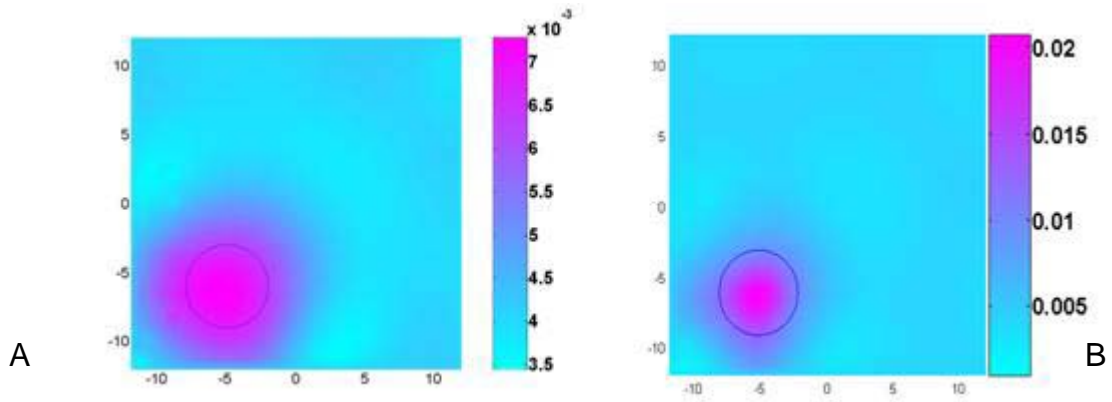


Figure 2-3. 2D simulation comparison between FMT without A) and with B) DOT guidance

CHAPTER 3 EXPERIMENTAL SYSTEM AND METHOD

A desirable signal collecting platform in small animal preclinical research should have following features: noncontact with objects like modern MRI , CT and PET, robust signal collecting independent of spatial position, adaptive to different size sample and practical image registration method for easy comparison to the results of other medical imaging instruments. Fig.3-1 is the CCD based non-contact continuous wave (CW) DOT guided FMT system developed to fulfill stated requirements: The animals like rat ,mice and Drosophila can be measured in their nature state, the data acquisition is same for both big and tiny objects and reconstructed images have spatial coordinates for easy registration to other imaging method.

The no-contact method used in our small animal system can be handily transferred to implement noncontact breast cancer diagnosis. Currently commercial mammal graph for breast cancer diagnosis need to compress breast, which make it unpleasant experience for the patient and lose true spatial information for image registration to other methodology and post-surgery. DOT guided quantitative FMT noncontact system can have several advantages compared with current methods: Non contact scheme to avoid unwanted compress effects; Original uncompressed shape will help register optical tomography results with other methods; Functional imaging for soft tissue; Comfortable test environment for patients.

Experimental System

In our imaging system (see Fig. 3-1), the excitation light can be delivered to the phantom at multiple points in both X and Y directions via linear stages (300nm precision). For each source position, one set of excitation light data from the opposite

side of the phantom is recorded by a 1024x1024 pixels CCD camera (Princeton Instrument, Trenton, NJ). Emission light is collected by placing a band pass filter in front of the CCD. Our system has been constructed such that multi-angle transmission light can be collected for more accurate image reconstruction (four angles are used in most case with 0.5 arcsecond angle resolution). This is realized by rotating the phantom three 90° to collect transmission light at four different phantom projections.

A graphic user interface (Fig.3-2) coded with Visual C++ 6.0 is used to control the entire data acquisition. The software contains a host of device control features and is designed to maximize the flexibility of image acquisition and analysis. Motorized linear stage control and rotator control help improve precision and repeatability of data in experiments. The scanner controller and CCD camera are synchronized, so the sampling can be controlled to ensure that when the camera is actively acquiring a frame, sample, laser and CCD are all remain still. Some routine experiments are programmed so that only human intervention is to initiate the experiment by hitting mouse on “start” button. Each procedure is fully automated and streamlined to ensure fastest speed to obtain tomography images after signal sampling.

In some extreme experiments with low light level, to reduce systematic errors, baseline measurements need to be performed once on a homogeneous phantom in the absence of fluorophores.¹⁰⁵ Thus the ratio of the baseline measurements to calculated forward simulation data with the same homogeneous geometry, multiplying the measured data from the inhomogeneous phantoms, served as the true input for both DOT and FMT reconstruction.

Shape Extraction for Arbitrarily Shaped Objects

It is our aim to develop a noncontact system and able to accurately locate position and concentration of fluorophore accumulated on the organ or tumor of live mouse in its nature state. To improve the accuracy on shape extraction of live mouse and simplify experimental procedure, shape-from-silhouette (also referred as visual hull) method is implemented to render 3D model of sample. The 3D model is utilized in the whole experiment data process pipeline: finite element mesh generation, mesh optimization and post process, data mapping and extraction from raw experimental data, 3D fluorescent imaging inverse reconstruction algorithm and image registration method for MRI and CT imaging. A rubber alligator is used to demonstrate the shape-from-silhouette method for 3D modeling of arbitrarily shaped objects.

Camera Calibration

Camera calibration often referred to as camera resectioning, is a way of examining an image, or a video, and deducing what the camera situation was at the time the image was captured. Camera calibration is used primarily in robotic applications, and when object model virtually based on real input. Rendering programs are all based on a virtual camera. In order for the modeled objects to be the equivalent of the real objects, we need to make sure that our virtual camera is in match with our real camera when we shot the photograph. Camera calibration achieves this and deducts where the real camera was relative to the scene. Our system uses Tsai's camera model which is based on the pinhole model of perspective projection. Given the position of a point in 3D world coordinates the camera model predicts the position of the point's 2D pixel coordinates. 11-parameter-pinhole camera model is used to describe our CCD. The internal parameters describe how the camera forms an image while the external parameters

describe the camera's position and orientation in the world coordinate frame. Calibration data for the model consists of 3D (x,y,z) world coordinates of a set of points and corresponding 2D coordinates (X_f, Y_f) (typically in pixels) of the feature points in chessboard photo. In Tsai's model, following 11 parameters fully determine a virtual camera.¹⁰⁶

5 intrinsic camera parameters:

- f - equivalent focal length as in the pin hole camera model
- K - 1st order radial lens distortion coefficient
- C_x, C_y - coordinates of center of field of view
- ξ - uncertainty factor for experimental system error and situations

6 extrinsic camera parameters:

- $R_x, R_y, R_z, T_x, T_y, T_z$ - rotational and translational components in the world's coordinate frame

C_x, C_y do not need to be experimentally determined, we can obtain the value from camera parameter for Princeton 1024*1024 CCD with 13um pixel size, , when bin =4 $C_x=C_y=128$, for the field of view close to lens center $K=0 \xi=1$. $f, R_x, R_y, R_z, T_x, T_y$ and T_z are determined using calibration data obtained from chess board method.¹⁰⁶ We define the center of chess board picture is zero and calculate each corner's coordinates based on the true side length of each square. The square corner position is estimated by eye and then the subpixel accuracy is obtained determined by corner finder algorithm based on autocorrelation method (Harris corner finder method).¹⁰⁷

Multi Camera Calibrations

To get 3D model with millimeter accuracy, 72 projection (one projection every 5 degree) silhouettes are used to render 3D sample contour. Therefore we need to do camera calibration for each angle of all 72 projections. Calibrate same camera in different project separately usually result in different focus length and scale factor value due to non uniqueness of optimization problem (>10 parameters) when using imperfect experimental data. In experiments, since the CCD rotation center and sample rotation center is not perfectly centric and CCD focus plane is not perfectly parallel to calibrate plane, it is impractical and tedious to calibrate CCD camera for all 72 angles. In order to obtain virtual CCD parameter to describe our CCD camera for all 72 angle projections by modifying only rotation angle of y axis (R_y) value of one virtual camera, the multi-camera calibration is implemented through following procedure:

1. Find the camera rotation center. If the center of chess board is the rotation center of the CCD camera, center of chess board corners should have same pixel value 128 for different angles of view (256*256 region of interest). Z direction of chess board can be moved forward or backward for better center alignment. For tiny objects like Drosophila pupae, the sample stage is a needle tip. As long as the needle tip is in the center of image and remains the same pixel value while the needle tip spin, the needle tip is right in center position.

- 2 Mount chessboard pattern on the stage, the center of chessboard is in the center of rotation. 3.6mm square is used for big macrolens 0.7mm square is used for small microlens. The coordinates is defined as in Fig. 3-3.

Calibrate -30, 0,30 degree CCD camera and obtain 3 set of calibration parameters. Use each of this 3 calibration parameter to generate CCD model for -30 0 30 degree by

modifying R_y and predict CCD pixel positions for all three positions. The best calibration parameter model among the three model set gives minimum error in predicted pixels of 30, 0, 30 degree. Fig. 3-4 shows the raw input data of calibration data and predicted pixel positions of corners from calibrated CCD model at 0 degree.

3 Modify R_y value (New R_y value of new position = R_y of chosen CCD model position ($-\pi/6, 0, \pi/6$) + Radius difference between the new position and chosen CCD model position) of the best camera model in accordance with 72 different angle positions of the CCD camera.

If CCD camera and sample stage are always fixed, the calibration is a one-time-only process. In addition, camera calibration model is the foundation that determines performance of all following data process. Therefore, multiple repeated calibrations and extra effort are worthwhile to obtain the best camera model for following procedures.

Visual Hull Method

Visual hull is a geometric entity created by shape-from-silhouette 3D reconstruction technique. This technique assumes the foreground object in an image can be separated from the background. Under this assumption, the original photos can be converted into a foreground/background binary silhouette image by defining a threshold. The foreground silhouette is the 2D projection of the corresponding 3D foreground object. Along with the camera viewing parameters, the silhouette defines a back-projected generalized cone that contains the actual object. The visual hull is the maximal object that has the same silhouettes of all projects as the original object,^{108, 109}

Visual hull algorithm has been explored extensively recently and has three major categories: volume-based (e.g. voxel carving methods),¹¹⁰ polygon-based (e.g.. polyhedral visual hull)¹¹¹ or image-based¹¹² and model fitting helps to obtain a

smoother result.¹¹³ The basic principle of algorithm is implemented through following steps:

First, convert digital photo to binary silhouette images of each projection by defining a threshold for boundary.

Second, the true camera projection position (note: position for the virtual camera model, not the camera position) is determined through camera calibrations. Compute camera projection matrices according to determined coordinates.

Third, the space of interest is divided into discrete voxels. Test every voxel by projecting it into image planes defined by projection matrices of all camera projection. If the projected point is contained in the silhouette for all 72 camera positions, the voxel is inside the visual hull. The union of all the voxels tested be inside visual hull is the 3D model of the objects. The resolution of visual hull is determined by the voxels size and could be improved by adding more camera projections. As Fig. 3-5 shows: the overlap of three camera projections is the visual hull of the sample and the visual hull can be refined by adding more camera positions.

We use a rubber alligator to access our visual hull method and a mock FMT experiment is used to test performance. As Fig. 3-6 and 3-7 shows, the alligator's shape is well reconstructed and the detector and source positions are mapped and the error is less than 1mm.

The major drawback is that concave surfaces cannot be reconstructed very well. Fortunately, very few regions of the small animals used for imaging actually are concave (i.e., the regions under the forearm and hind legs) and no current research focused on these convexity parts. When the complete (convex and concave) surface

areas are needed, more advanced surface extraction approaches should be used such as 3D surface cameras^{114, 115} or spatially modulated illumination patterns.

Because DOT and FMT has a resolution about 1~5 millimeters, and the variations of the order of the mean free path do not have an impact on the reconstructed images. Therefore, Visual Hull approximation can provide adequate accuracy. In addition, this means that while the surface may change during silhouette acquisition due to breathing, an average surface rendered by 72 camera position is accurate enough for FMT or DOT.

Free Space Data Extraction Model

Detector Model

Arbitrarily shaped objects need extra process since CCD collect signal from image plane instead of sample boundary. Ntziachristos *et al.* proposed a model to collect light intensity signal from arbitrarily shaped objects and experimentally testified by reconstructing a fluorescent target with normalized Born approximation method.^{35, 116}

$$\mathbf{J}_{\text{det}}(\mathbf{r}_d) = \frac{1}{\pi} \int_s \mathbf{J}_n(\mathbf{r}') \Gamma(\mathbf{r}, \mathbf{r}_d) dS' \quad (6)$$

$$\Gamma(\mathbf{r}, \mathbf{r}_d) = \xi(\mathbf{r}, \mathbf{r}_d) \frac{f(\text{NA} - \sin \theta_d)}{|\mathbf{r}_d - \mathbf{r}|^2} \cos \theta \cos \theta_d dA \quad \mathbf{r} \in S \quad (7)$$

The focus plane of CCD is treated as 2D virtual pixel detector array with certain number aperture (NA) . When small aperture assumption is met, $\mathbf{J}_{\text{det}}(\mathbf{r}_d)$ is the actual signal obtained by each virtual detector on CCD focus plane. As we can see, $\mathbf{J}_n(\mathbf{r}')$ is related to $\mathbf{J}_{\text{det}}(\mathbf{r}_d)$ by above equation (6) and (7), under some simplification $\Gamma(\mathbf{r}, \mathbf{r}_d)$ can be calculated for corresponding experimental situation in Fig. 3-9:

$f(NA - \sin \theta_d)$: The NA is considered through this Gaussian function, which modeled as a Gaussian of full width at half maximum of $2NA$, NA is determined by parameters of lens, CCD and actual experimental dimension situations.

$\xi(\mathbf{r}, \mathbf{r}_d)$: define the visibility or directivity calibration factor and discard surface points not visible from the detector. It is determined by projection area on the sample surface of each virtual detector on focus plane, detection area dA and experimental calibration factor. The value can be set as 1 for most experiments.

$1/|\mathbf{r}_d - \mathbf{r}|^2$: solid angle term $|\mathbf{r}_d - \mathbf{r}|$ is the distance between specific surface detector node and corresponding virtual detector on focus plane.

$\cos \theta$: Lambert's cosine dependence term (Fig. 3-8). θ is the angle between the normal vector of surface node and normal vector of virtual detector on focus surface

θ_d is the angle between light path and the virtual detection surface normal vector, in most in focus case, θ_d can be treated as 0.

Source model

When an arbitrarily shaped object is measured, each source have different incident angle which results in various reflection lost, so true photon density of each source that propagated into the object should be calculated individually. As in Fig. 3-10:

$$t_{\parallel} = E_{0t} / E_{0i} = 2n_i \cos(\theta_i) / [n_i \cos(\theta_t) + n_t \cos(\theta_i)] \quad (8)$$

These equations are called the Fresnel Equations for parallel polarized light.

$$t_{\perp} = E_{0t} / E_{0i} = 2n_i \cos(\theta_i) / [n_i \cos(\theta_i) + n_t \cos(\theta_t)] \quad (9)$$

These equations are called the Fresnel Equations for perpendicularly polarized light.

In scenario of our experiments, finite element mesh of the arbitrarily shaped object has absolute coordinates centered at rotation center of rotator stage. For each node, surface normal vector towards free space and distance from focus plane of CCD lens could be obtained. Numerical aperture and visibility factor were determined for each virtual CCD detectors based on experimental situation and manufacturing parameters of the lens and CCD camera. Thereafter, solid angle value of each virtual detector on the CCD focus plane and Lambert's cosine law were used to convert detectable CCD signal into photon density of each surface detector node on the finite element mesh. With known surface normal vector of each source and Fresnel equations, light reflection loss of each source was calculated to obtain actual photon density which was used as assigned light intensity value of each source node on the finite element mesh.

Implementation in FMT System

The complete experimental procedure is described in Fig. 3-11. The DOT guided FMT for arbitrarily objects is established and tested. The data acquisition and processing programs are streamlined for maximum repeatability.

The well-known shape-from-silhouette 3D recovery approach was used to render the 3D model of the actual sample used.¹¹⁷ In this method, the CCD camera was modeled as a pinhole camera positioned in a coordinate system where its intrinsic and extrinsic parameters (i.e., space projective transformation matrices) were calibrated using the widely used chess board method,¹¹⁸ allowing the calculation of the extrinsic parameters for a new position while the intrinsic parameters stayed the same for all the positions. A total of 72 projection images (one projection every 5° by rotating CCD 360°) were used in our calculation giving a submillimeter resolution. The projection images were then converted into foreground/background binary silhouette images (the 2D

projections of the 3D foreground object). Each silhouette defined a back-projection of a cone that contained the geometrical information of the actual phantom. Thus the overlapped volume of all 72 cones defined by silhouettes gave the 3D visual hull model of the arbitrarily shaped phantom. A photoluminescent plate was used as the background screen which provided evenly distributed illumination and good contrast.

A 3D finite element mesh of the 3D model was then generated with the point cloud obtained by visual hull method: use point wrap function in Amira 3.1 to obtain the surface. The surface need to be post-processed to obtain a good uniform surface which is the prerequisite of good mesh generation to minimize mesh effect on final tomography reconstruction. The process includes: 1, Flip the edges in triangle element which have aspect ratio (maximum length/minimum length) bigger than 4; 2, Remove dihedral angle below 60 degree; 3, Remove coplanar face; 4, Remove all intersection to ensure a closed surface. After these post processes, the surface is smoothed and refined. We can simplify the refined mesh to any desired face number based on desired mesh node numbers (for example, a 3000 faces surface usually can generate a 4500 nodes 3D mesh). The “compute tetragen” function in Amira 3.1 can be used to generate 3D finite element mesh and optimized the mesh quality. The generated mesh is optimized to decrease half band width for a fast computation.

There is also a need to map the photon density read from the CCD camera (actually the virtual detector along the focal plane of the CCD camera) onto the arbitrarily shaped surface of the phantom. We have adopted a method developed by Ntziachristos *et al.*^{35, 116} that was able to realize the mapping accurately in their FMT studies. In this method, a Lambert's cosine law and solid angle based light propagation

model is established to correlate the photon density at the virtual detector and that at the animal surface. With this model, given the relative geometric relationship between the virtual detector and the phantom surface, the numerical aperture of the virtual detectors and the visibility factor that can be experimentally calibrated, one can accurately convert the read out from the CCD into the photon density at the phantom surface for tomographic reconstruction.

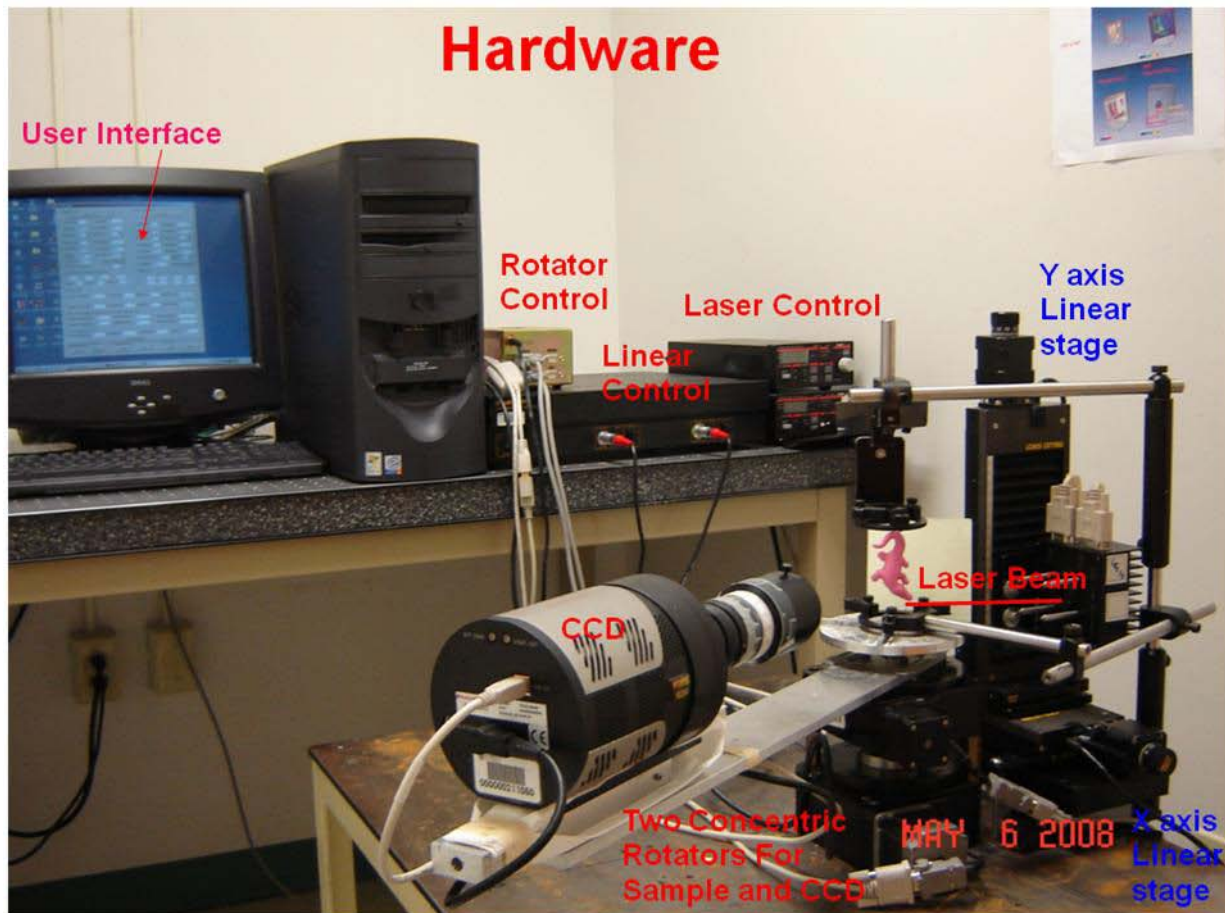


Figure 3-1. DOT guided FMT experiment system.

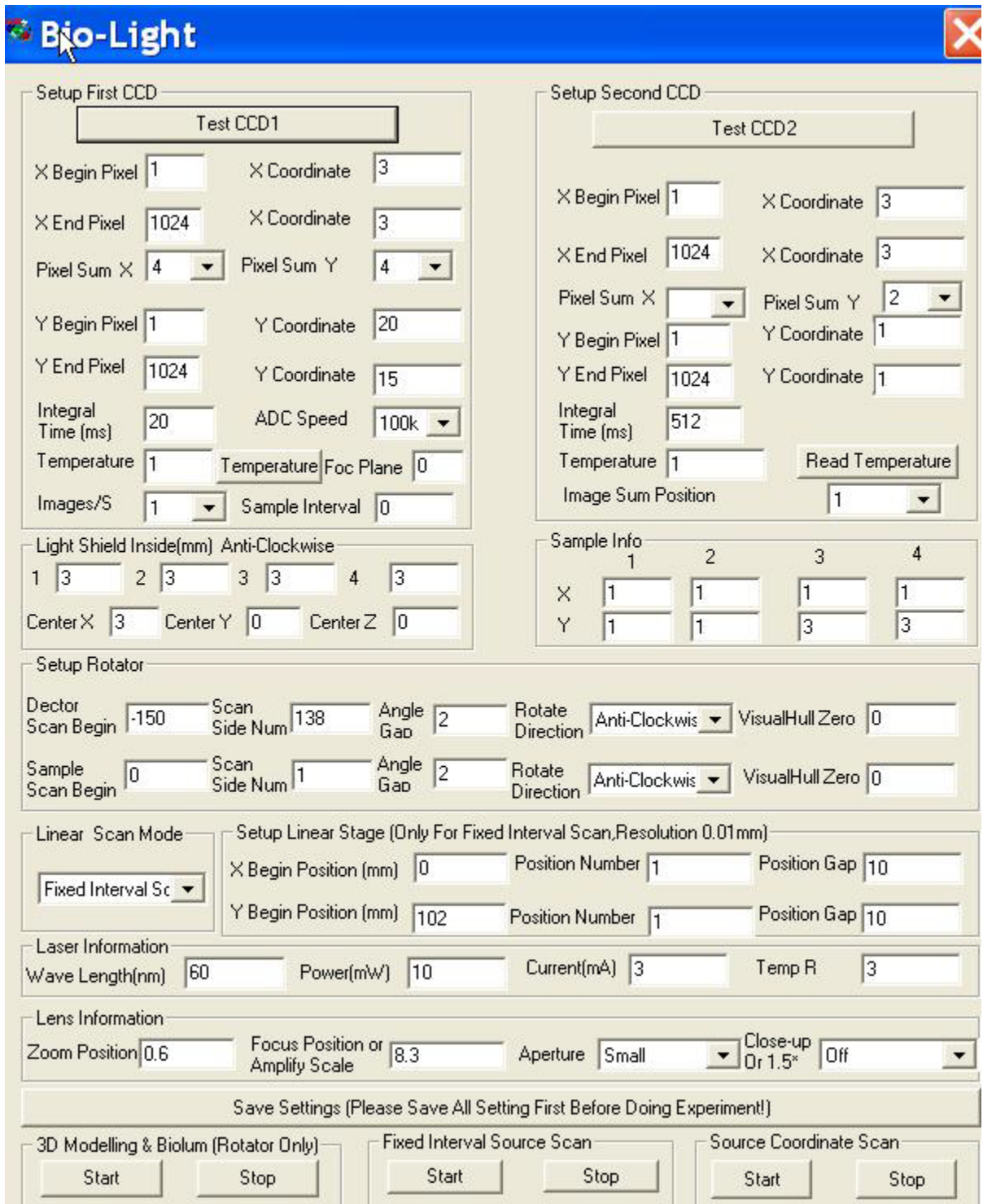


Figure 3-2. Graphic user interface of the system

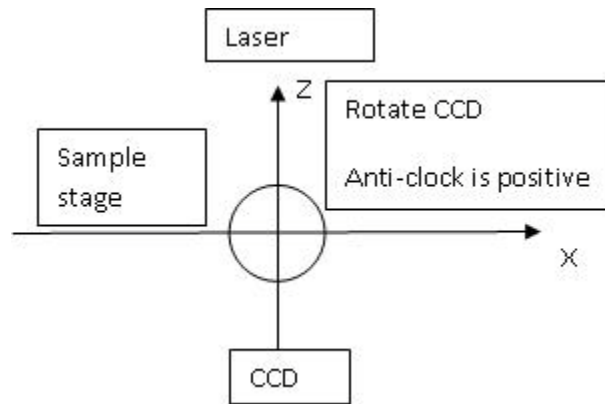


Figure 3-3. Coordinates system definition: top view from observe point above the sample stage and Y axis direction is from paper internal to outside.

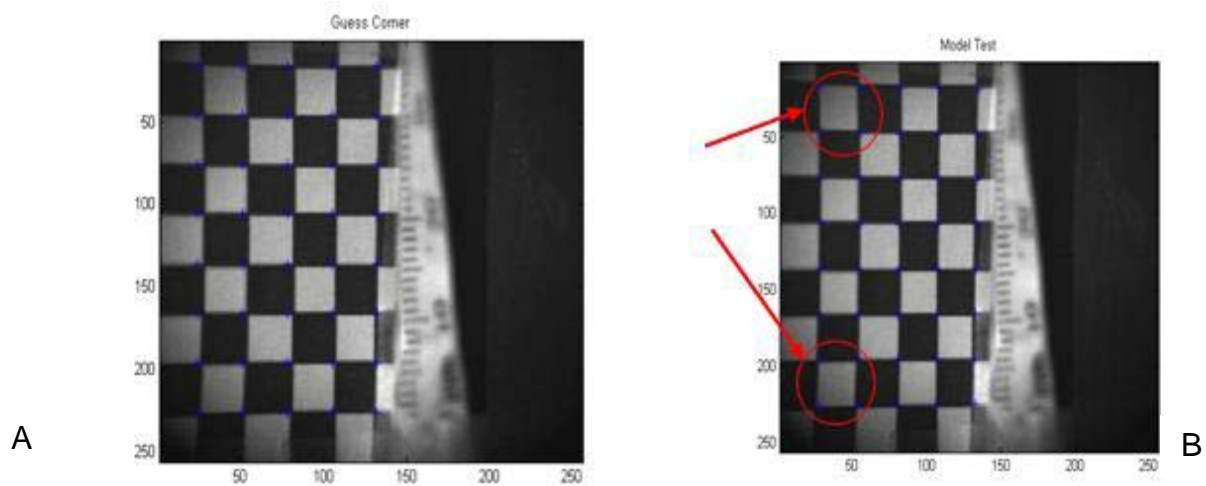


Figure 3-4. Use calibrated CCD model parameters and universe world coordinate of grids to predict pixel values of corners in the image. A) original input data for CCD calibration, B) pixel positions predicted by CCD model obtained by CCD calibration

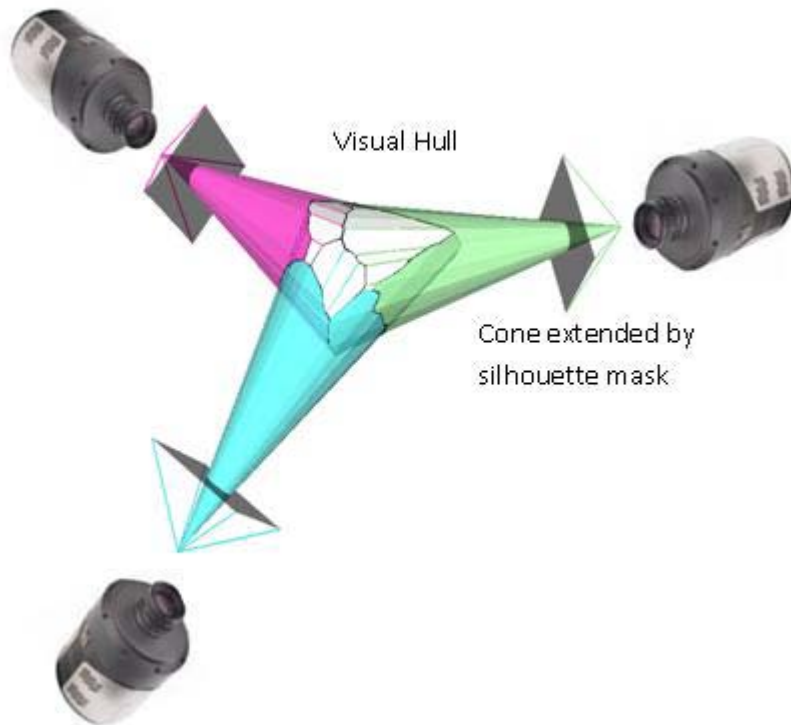


Figure 3-5. Visual hull scheme demonstration. The intersection of the silhouette projection cone (shown in pink, blue and green) is a cross-section of the visual hull. Additional silhouette photos from new viewpoints will further constrain the intersection region, carve and refine 3D visual hull.



Figure 3-6. Original rubber alligator and its 3D finite element mesh. Finite element mesh is generated based on 3D dot contour obtained by visual hull method.

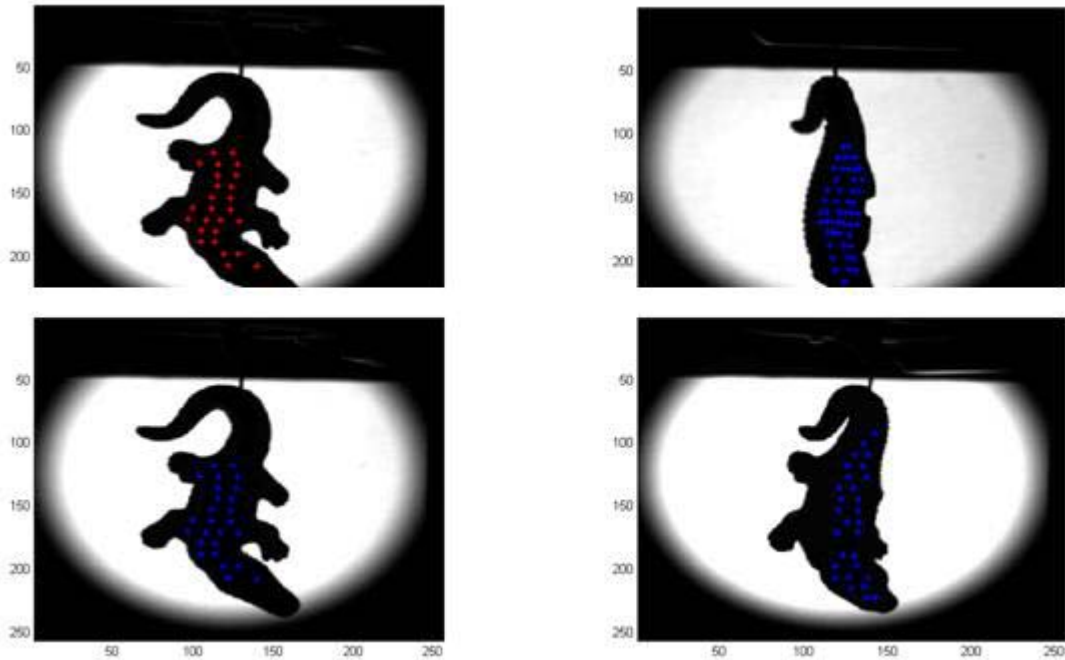


Figure 3-7. Sources (red dots) and detectors (blue dots) of different projections.

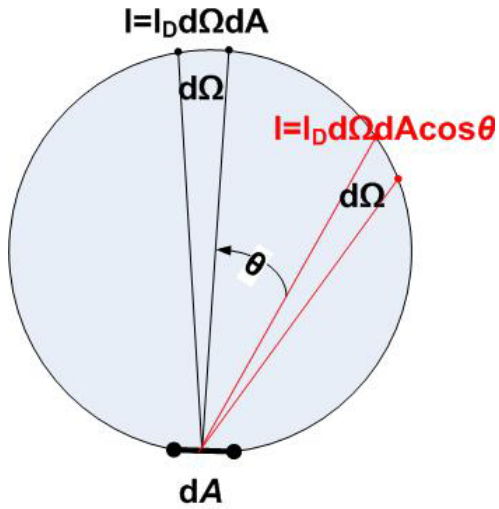


Figure 3-8. Lambert's cosine law

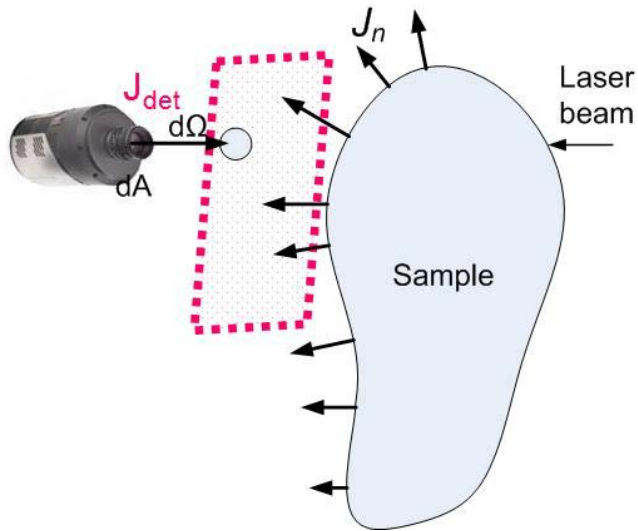


Figure 3-9. Scattering geometry for a diffusive object of volume V surrounded by air for free space model. ¹¹⁶

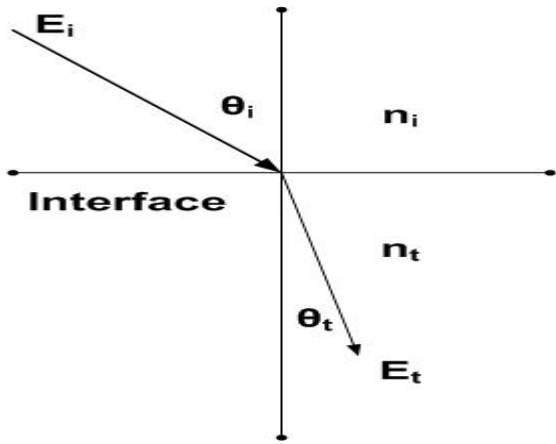


Figure 3-10. Photon density model of source on the air/sample interface

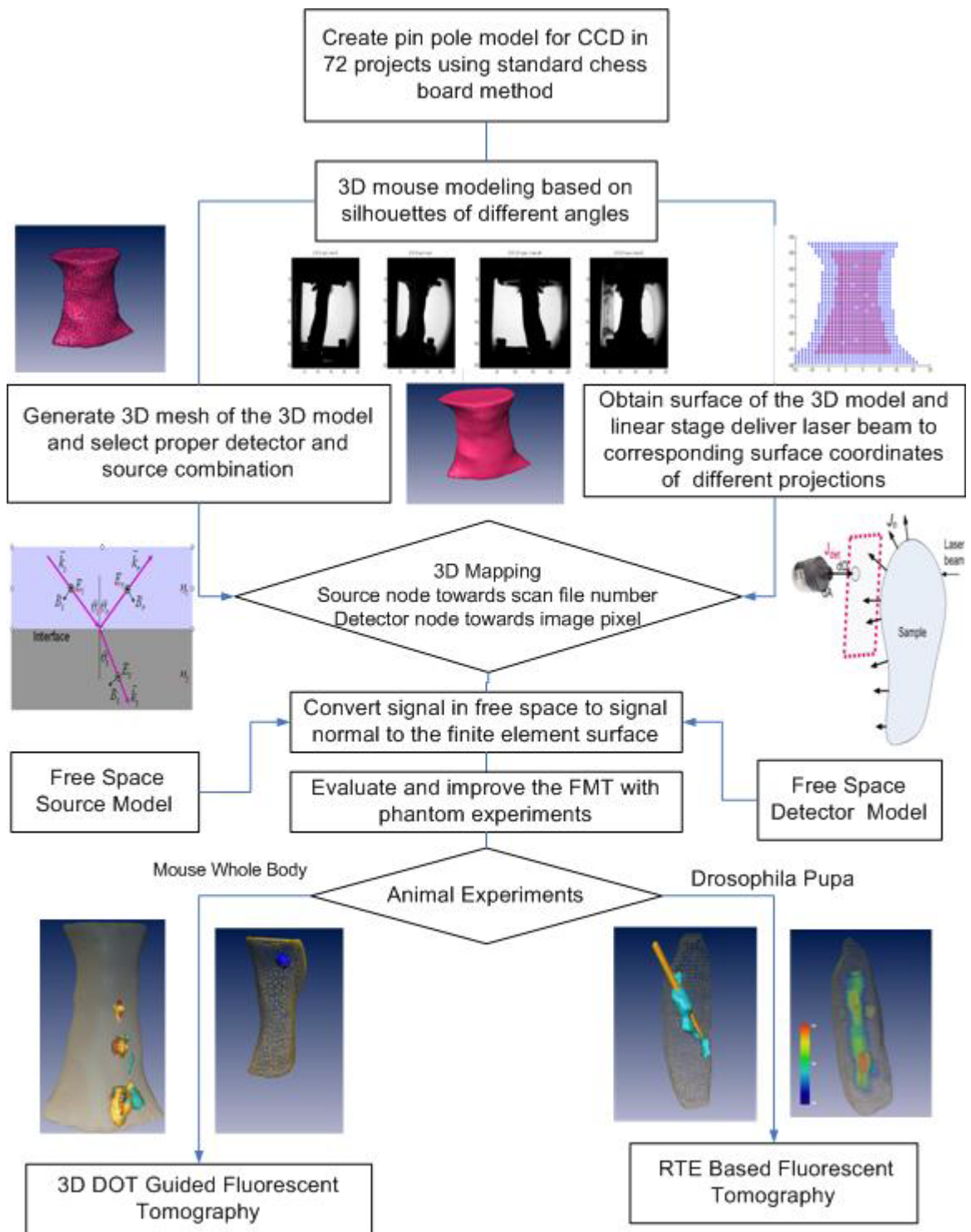


Figure 3-11. Outline of experimental procedures

CHAPTER 4 PHANTOM EXPERIMENTS

Algorithms and hardware system are evaluated by using regular shaped and arbitrarily shaped 3D phantoms. Targets of arbitrarily shaped phantoms also mimic mouse anatomy structures as *in vivo* situation.

Indocyanine green (ICG) is the only FDA-Approved dye with strong optical absorption in the near-infrared (NIR) region, where light can penetrate deepest into biological tissue. ICG is well characterized with quantum yield data and fluorophore absorption coefficient $\mu_{a_{x \rightarrow m}}$. In our phantom experiments, ICG is used to evaluate our DOT guided FMT algorithm. According to Beers' law, fluorophore absorption coefficient $\mu_{a_{x \rightarrow m}}$ is proportional to fluorophore concentration since quantum yield is stable at low concentration in most preclinical applications.

Here we present a systematic study using phantom experiments under the condition of heterogeneous μ'_s and μ_a distributions for fluorescence image reconstruction. In our approach, we directly reconstruct optical heterogeneities using DOT and apply reconstructed μ'_s and μ_a distributions to the FMT reconstruction. Both DOT and FMT reconstructions are conducted using a noncontact multi-angle transmission scheme, coupled with finite element reconstruction algorithms. Our experimental results suggest that the optical heterogeneous nature of the target itself, especially when its size is relatively large, must be considered for quantitatively correct FMT in the framework of finite element based reconstruction methods.

We note that several methods (CT, MRI and PAT) to address heterogeneity issue in real experimental study have been combined with FMT.¹¹⁹⁻¹²² Guided methods like

MRI and CT also can only indirectly reveal optical property by heuristic or anatomical assignment. PAT can provide distribution of absorption coefficient, but it cannot provide the distribution of scattering coefficient. This information is critical for quantitative FMT as it was demonstrated in our former experimental results²⁸ and Milstein *et al.*'s simulation results.¹⁰¹ While it is true that PAT offers better spatial resolution than DOT, its ability of tissue penetration is not as good as DOT. In addition, all-optical based DOT-guided FMT can be conveniently implemented without adding extra hardware, while additional ultrasonic detection/data acquisition is needed for PAT/FMT combination.

Regular Shaped Objects

We have performed a series of regular phantom experiments (Fig. 4-1) to evaluate the merits of considering the heterogeneous μ_a and μ'_s distributions in the fluorescence reconstruction. Reconstructed optical and fluorescence images for a representative 2D case is given in Fig. 4-2, while the recovered $\mu_{a \rightarrow m}$ values from a number of 2D cases having different ICG concentrations are presented in Fig. 4-3. Validation of 3D image reconstruction algorithm is given in Fig. 4-4 for a representative 3D case.

In the representative case, the 6mm diameter target contained 1 μM ICG and was positioned at (-5,-6). The DOT recovered μ_a and μ'_s distributions are given in Figs. 4-2 (a) and 4-2 (b). Fluorescence image is reconstructed under four scenarios: DOT recovered μ_a and μ'_s distributions (Fig. 4-2. (c)), uniform μ'_s but DOT recovered μ_a distributions (Fig. 4-2 (d)), uniform μ_a but DOT recovered μ'_s distributions (Fig. 4-2 (e)), and uniform μ_a and μ'_s distributions (Fig. 4-2 (f)). Examining the images shown in Fig. 4-

2, it can be seen that when the DOT recovered μ_a and μ'_s distributions are used, the fluorescence image is most accurately reconstructed in terms of the size/shape and $\mu_{a_{x \rightarrow m}}$ value of the target. We can clearly see that the uniform μ_a and μ'_s assumption results in the worst $\mu_{a_{x \rightarrow m}}$ reconstruction (Fig. 4-2 (f)), where the recovered target size is significantly overestimated, and the recovered $\mu_{a_{x \rightarrow m}}$ of the target has about 75% error relative to the literature value of 0.03.

We can also see that the μ'_s distribution plays a critical role in determining an accurate FMT reconstruction. With heterogeneous μ'_s but uniform μ_a distributions (Fig. 4-2 (e)), the recovered image quality is better and the reconstructed $\mu_{a_{x \rightarrow m}}$ value is closer to the literature value ($\mu_{a_{x \rightarrow m}} = 0.03$), compared with that using heterogeneous μ_a but uniform μ'_s distributions as shown in Fig. 4-2 (d). This finding is consistent with our simulations and the simulations conducted by Epstein *et al.*³¹

For fluorescence reconstruction, the μ_a and μ'_s distributions at the excitation wavelength (785nm) were used to interpolate their values at the emission wavelength (830nm) using the absorption spectrum data available in the literature.¹²³⁻¹²⁶ Based on the literature,¹²⁷ the quantum efficiency η of ICG is stable under the condition of low ICG concentrations as used in our experiments. Thus, the reconstructed fluorescent yield ($\eta\mu_{a_{x \rightarrow m}}$) under different ICG concentrations should be solely determined by $\mu_{a_{x \rightarrow m}}$, which is directly proportional to the ICG concentration according to the Beer-Lambert Law. $\mu_{a_{x \rightarrow m}}$ value was also used to provide a basis of comparison between calculated $\mu_{a_{x \rightarrow m}}$ and that obtained via spectroscopic methods.^{91, 128} In this work we used a

quantum yield value of 0.016 which was measured under nearly the same experimental condition as in our experiments.⁹¹ Quantitative performance of our reconstruction approach is further evaluated using the 6mm diameter target containing different ICG concentrations (0.1, 0.2, 0.4, 0.6 and 1.0 μM). In the image reconstructions, the $\mu_{a_{x \rightarrow m}}$ values ($4 \times 10^{-12} \text{mm}^{-1}$) of the background phantom were used as the initial guess for all these experimental cases. Reconstructed $\mu_{a_{x \rightarrow m}}$ values with and without DOT recovered μ_a and μ'_s distributions are plotted in Figs. 4-3, where values from the literature are also presented for comparison. For better comparison, the $\mu_{a_{x \rightarrow m}}$ value at 0.1 μM from the literature was used to calibrate the $\mu_{a_{x \rightarrow m}}$ value at 0.1 μM from the FMT reconstructions. It is clear that the results with the DOT recovered optical property distributions are in good agreement with that from the literature, whereas the recovered $\mu_{a_{x \rightarrow m}}$ value, with the uniform optical property distribution assumption, is significantly away from the “exact” value and basically not quantitatively correct, compared to that of spectroscopy method.

While the 2D reconstruction described above is simple, computationally fast and yet able to provide reasonably accurate results, we have also implemented the DOT guided FMT approach in 3D and tested it using several phantom experiments. 3D cases' results are consistent with results of 2D cases. In the 3D phantom experiments, a 6x6mm cylindrical solid target containing ICG was embedded in a 30x30x30mm cubic background. A total of 260 source and 260 detector positions were used for image reconstruction with a finite element mesh of 4354 nodes.

2D Experiments

Experiments were conducted using a continuous wave (CW) 785nm diode laser at 65mW for the FMT experiments and at 2mW for the DOT experiments. It takes less than 1 minute (Integral time 50ms per source) for a set of excitation light data and less than 10 minutes (Integral time 5s per source) for a set of emission light data. Since experiment running requires CCD, X axis linear stage, Y axis linear stage, sample rotator, CCD rotator works together and each one need work with respect to status of others. System is synchronized to make sure every move of each component is desired and happens on specific time window.

In the experiments, the laser beam was focused directly onto the sample to serve as a point source. The focal plane of the CCD represented a collection of virtual detectors. The excitation source positions at the phantom surface were determined precisely by the X, Y linear stage, while the detector positions for both the excitation and emission light collection were accurately with an accuracy of coordinate mapping of $\pm 0.25\text{mm}$. For each set of transmission imaging data, we used 25 detectors and 25 sources that covered a 24x24mm central area of a 30x30mm phantom. A finite element mesh with 1186 nodes was used for all the image reconstructions.

In the phantom experiments, a 6mm diameter solid cylindrical target containing ICG was embedded in a 30x30x90mm solid cuboid, mouse-size background phantom. The background phantom was composed of 1% Intralipid, India ink and 1% Agar powder, providing a μ'_s of 1.0/mm and a μ_a of 0.005/mm. The target had a μ'_s of 2.0/mm and μ_a was contributed by both the India ink (0.005/mm) and $\mu_{a_{x \rightarrow m}}$ of ICG. To test the

quantitative performance of the system, we prepared a series of targets containing low concentration ICG (0.1uM, 0.2uM, 0.4uM, 0.6uM and 1uM).

3D Experiments

In the experiments, the laser beam was focused directly onto the sample to serve as a point source. The focal plane of the CCD represented a collection of virtual detectors of area $dA= 1\text{mm}^2$. 7 layers of sources with averagely 13 sources at each layer were used. Signals from a total of 363 source (corresponding to 4 CCD positions/angles) and 363 detector positions were collected transmission data for both DOT and FMT. We used a finite element mesh of 4598 nodes and 22539 tetrahedron elements. Regular shaped DOT guided FMT qualitative and quantitative performance improvements for a representative case (1uM ICG in the target) , as we can see in Fig. 4-4 where the exact fluorescent target (red), the recovered fluorescent target with (gold) and without (blue) DOT guidance are fused together for easy comparison.

Examining the images shown in Fig. 4-4, it can be seen that when the DOT recovered μ_a and μ'_s distributions are used, the FMT image is most accurately reconstructed in terms of the size/shape, position (partially overlapped with the exact position) and $\mu_{a \rightarrow m}$ value (0.026 mm^{-1}) of the target. We can clearly see that the uniform μ_a and μ'_s assumption results in unsatisfied $\mu_{a \rightarrow m}$ reconstruction, where the recovered target shape is distorted, the recovered $\mu_{a \rightarrow m}$ value of 0.01 mm^{-1} has about 67% error with respect to the exact value of 0.03 mm^{-1} , and the target position is shifted.

Arbitrarily Shaped Objects

Herein, we first demonstrate the combination of CW FEM based DOT/FMT with 3D free-space non-contact detection and fully consider the distribution of both

absorption and scattering coefficients with arbitrarily shaped phantom geometries. In addition, the phantom mimics a realistic *in vivo* (mouse) anatomy heterogeneous optical situation and animal boundary shape. The experiments were conducted using an optical fiber free system based on a non-contact multi-angle transmission scheme, and the 3D fluorescence images were recovered using our finite element-based FMT reconstruction algorithm with DOT guidance. Our approach is demonstrated using a series of phantom experiments with low ICG concentration (0.1, 0.2, 0.4 and 1.0 μM) targets.

In the phantom experiments, a 6x6mm cylindrical solid target containing ICG was embedded in a mouse-size arbitrarily shaped phantom. The background phantom was composed of 1% intralipid, India ink and 1% agar powder, providing a μ'_s of 1.0/mm and a μ_a of 0.03/mm. Five optical heterogeneities mimicking lung, heart, liver and stomach in a mouse were embedded in the background and their optical properties are listed in Table 4-1 according to the literature.¹²⁹ The “stomach” also served as the fluorescent target containing ICG at a variety of low concentrations (0.1, 0.2, 0.4 and 1 μM). Based on the literature,¹²⁷ the quantum efficiency η of ICG is stable under the condition of low concentrations as used in our experiments. Thus, the reconstructed fluorescent yield ($\eta\mu_{a_{x \rightarrow m}}$) under different ICG concentrations should be solely determined by $\mu_{a_{x \rightarrow m}}$, which is directly proportional to the ICG concentration as the Beer-Lambert Law states. Reconstructed $\mu_{a_{x \rightarrow m}}$ value was compared with $\mu_{a_{x \rightarrow m}}$ obtained via spectroscopic methods.^{91, 128} In this work we used the reported quantum yield, $\eta = 0.016$ from the literature which was measured under nearly the same experimental conditions as in our experiments.⁹¹

Reconstructed optical and fluorescence images for a representative case are given in Fig. 4-6: μ_a , μ'_s and $\mu_{a \rightarrow m}$ images are given in Fig. 4-6 (b), Fig. 4-6. (c) and Fig. Fig. 4-6 (d) respectively.

While the recovered $\mu_{a \rightarrow m}$ values from a number of cases having different ICG concentrations are presented in Fig. 4-7. For the representative case, the phantom, the exact position, shape and size of the optical heterogeneities are shown in Fig. 4-6 (a) and table 4-1 while the recovered μ_a , μ'_s and $\mu_{a \rightarrow m}$ images are given in Fig. 4-6 (b), Fig. 4-6 (c) and Fig. 4-6 (d) respectively.

In Fig. 4-6(d), the exact fluorescent target (orange), and the fluorescent target reconstructed with (yellow) and without (blue) DOT guidance are fused together for easy comparison where the isosurface plot of μ_a image is also depicted in black mesh. Examining the images shown in Fig. 4-6(d), it can be seen that when the DOT recovered μ_a and μ'_s distributions are used, the FMT image is most accurately reconstructed in terms of the size/shape, position (partially overlapped with exact position) and $\mu_{a \rightarrow m}$ value (0.025 mm^{-1}) of the target. We can clearly see that the uniform μ_a and μ'_s assumption results in unsatisfied $\mu_{a \rightarrow m}$ reconstruction, where the recovered target shape is distorted, the recovered $\mu_{a \rightarrow m}$ value of 0.007 mm^{-1} has about 80% error with respect to the exact value of 0.03 mm^{-1} , and the target position is significantly shifted.

Reconstructed $\mu_{a \rightarrow m}$ values with and without DOT recovered μ_a and μ'_s distributions for target containing different ICG concentrations are plotted in Fig.4- 7. Values determined by spectroscopic method from the literature are also presented for

comparison. It is clear that the results with the DOT guidance are in good agreement with that from the literature whereas the $\mu_{a_x \rightarrow m}$ values recovered with the uniform optical property distribution assumption is shifted significantly away from the literature values.

Table 4-1. Optical properties of the embedded “organs” and the background used in the experiments

	Lung	Heart	Liver	Stomach (also the ICG Target)	Background
μ_a (mm^{-1})	0.3	0.11	0.45	0.2	0.03
μ'_s (mm^{-1})	2.5	1.1	2.5	1.8	1.0

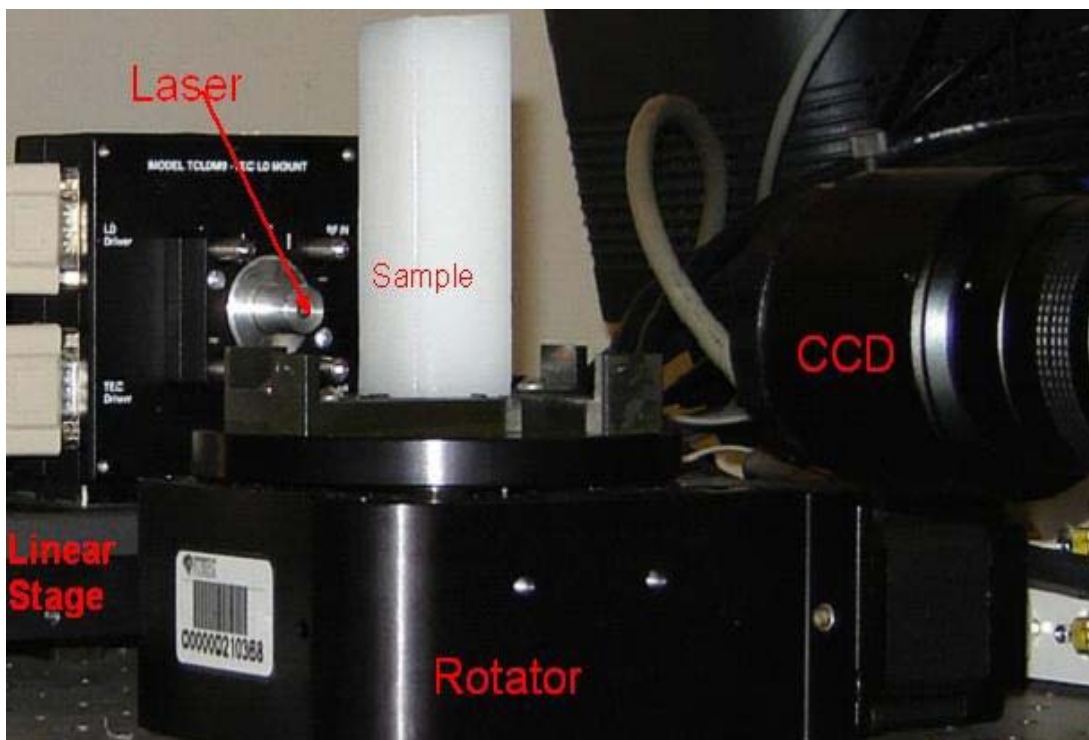


Figure 4-1. Photograph of the CCD based CW FMT system.

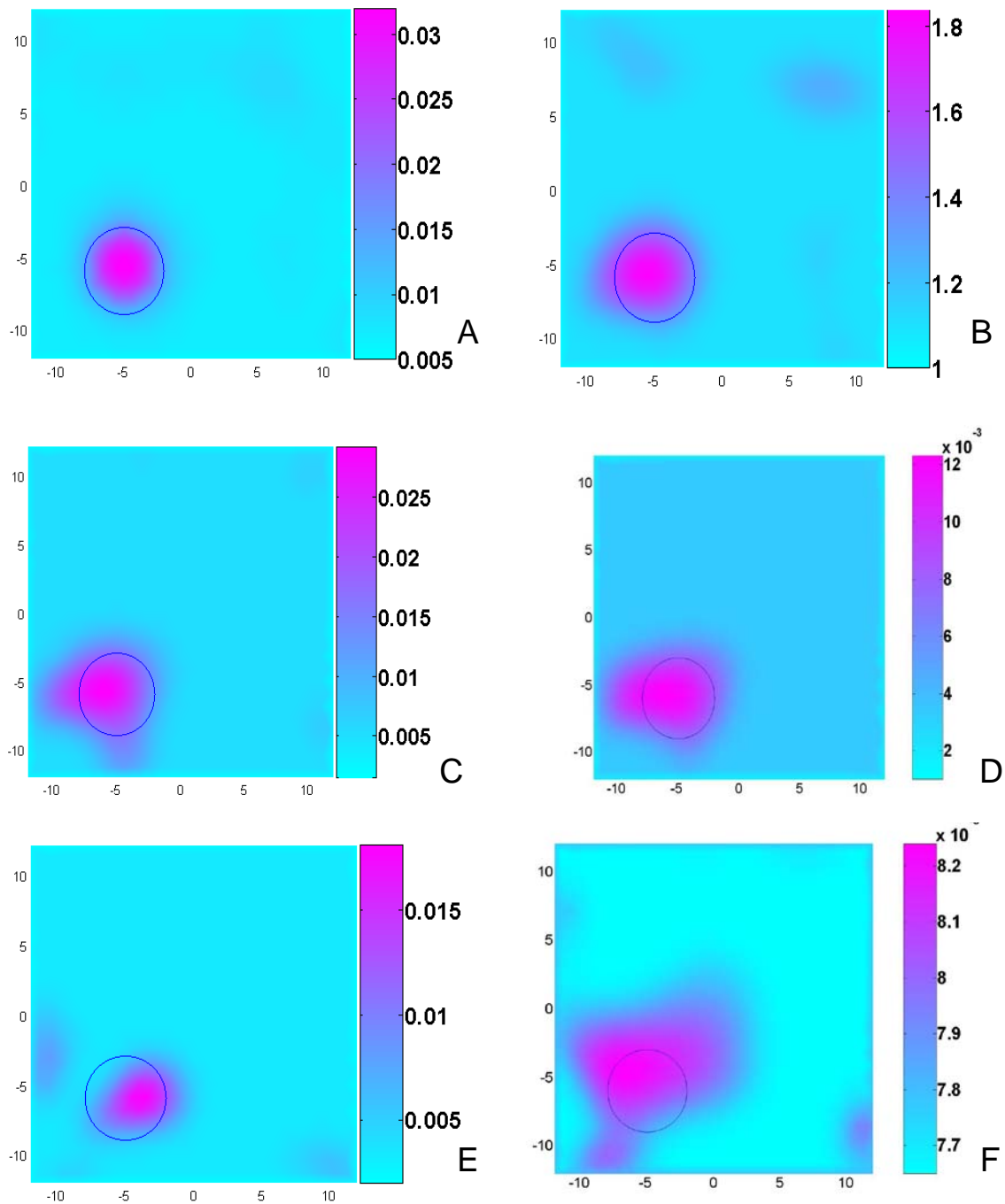


Figure 4-2. Reconstructed μ_a , μ'_s , and $\mu_{a \rightarrow m}$ images for a representative experimental case. A) μ_a image B) μ'_s image C) $\mu_{a \rightarrow m}$ with DOT recovered μ_a and μ'_s distributions D) $\mu_{a \rightarrow m}$ with uniform μ'_s but DOT recovered μ_a distributions, E) $\mu_{a \rightarrow m}$ with uniform μ_a but DOT recovered μ'_s distributions, and F) $\mu_{a \rightarrow m}$ with uniform μ_a and μ'_s distributions.

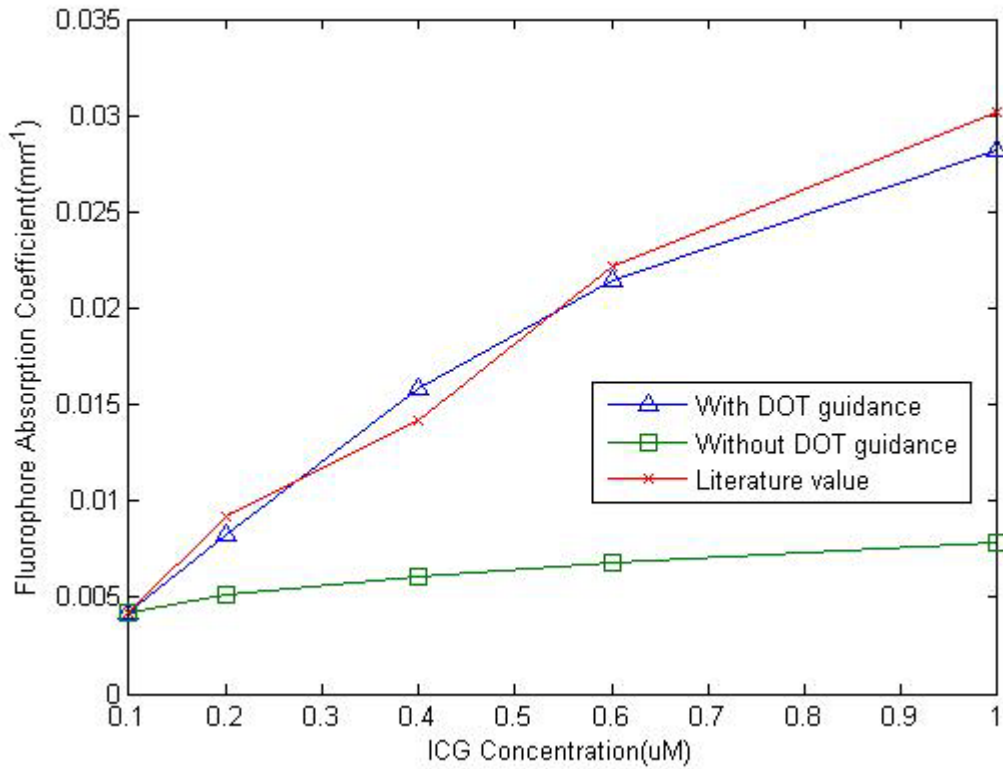


Figure 4-3. Reconstructed $\mu_{a \rightarrow m}$ values in the target with and without DOT recovered μ_a and μ'_s distributions when different ICG concentration was used. The $\mu_{a \rightarrow m}$ value from literature (0.1, 0.2, 0.4 and 0.6 μM) were obtained by spectroscopic methods,²¹ while the $\mu_{a \rightarrow m}$ literature value (1 μM) was obtained by a micromolar aqueous solution with a spectrofluorometer [8].

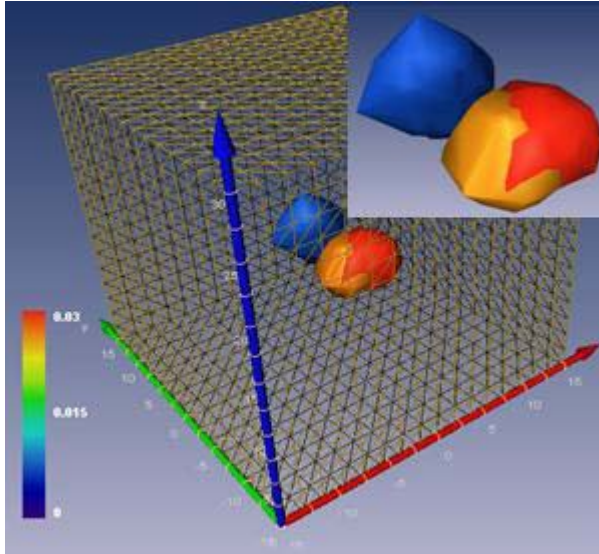


Figure 4-4. Reconstructed 3D images for a representative case (ICG concentration in the target= $1 \mu\text{M}$).



Figure 4-5. Arbitrarily shaped phantom experiment. A) Phantom and imaging system. Inclusion is the arbitrarily phantom. B) Raw boundary signal

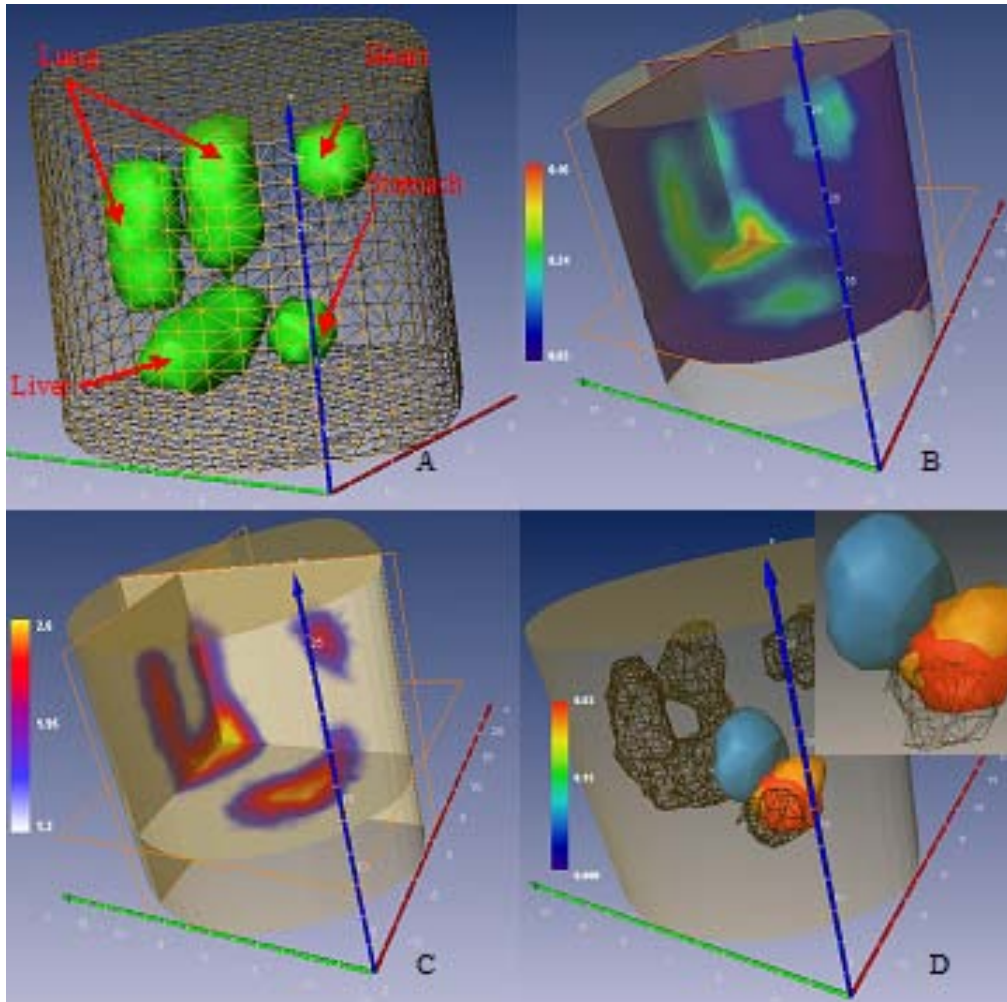


Figure 4-6. Exact positions of the targets in the finite element mesh A), and reconstructed μ_a B), μ'_s C), and $\mu_{a_{x \rightarrow m}}$ D) images for a representative case (ICG concentration = $1 \mu\text{M}$). In (d), the exact fluorescent target (orange), and the fluorescent target recovered with (yellow) and without (blue) DOT guidance are all shown. The insert is a close view of the recovered fluorescent target with and without DOT guidance relative to the exact target. Here the isosurface plot of the absorption image is also depicted (black mesh).

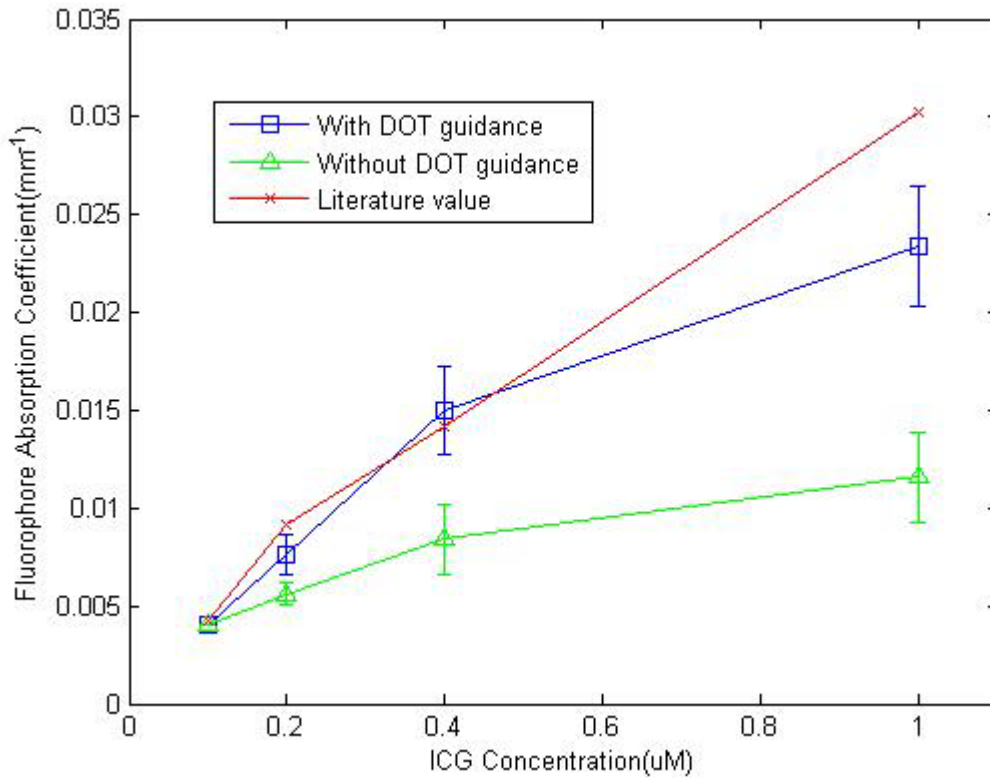


Figure 4-7. Reconstructed $\mu_{a_{x \rightarrow m}}$ values in the fluorescent targets with and without DOT guidance when different ICG concentration was used. For easy comparison, the recovered data shown were calibrated against the $\mu_{a_{x \rightarrow m}}$ value at 0.1 μM from the literature. Error bars are the deviation of each concentration point value and individual concentration point values are the mean value of five different experiments. The significance of differences was assessed between data with DOT guidance and data without DOT guidance using t-test, reconstructed value of 0.2, 0.4 and 1 μM ICG shows significant higher value with DOT guidance method (all p-values less than 0.05).

CHAPTER 5 APPLICATION IN A MOUSE MODEL

Diffuse optical tomography (DOT) guided fluorescence molecular tomography (FMT) is utilized to provide quantitative analysis in our breast cancer preclinical study. In this method, we conducted a full body optical property reconstruction of mice and applied the reconstructed optical property into FMT reconstruction as functional *a priori* information to minimize the heterogeneity effects. First, we conducted a well controlled experiment in which the volume, quantity and location of the tumor cells are known to validate quantitative and qualitative performance of the method in mice. In this experiment, mouse mammary tumor 4T1 cells were pre-labeled with a tumor targeting peptide conjugated with a near infrared fluorescence (NIR) dyes, Cy5.5. Following injection of different numbers of the NIR dye-targeting peptide-labeled living cancer cells into three subcutaneous locations of the mice. FMT was performed on the mice. Results of FMT reconstruction show that cell quantification and tumor localization are improved with DOT guidance. We further applied this method to evaluate target specificity and detection sensitivity of a newly synthesized NIR dye (NIR 830)-labeled urokinase plasminogen activator receptor (uPAR) targeted magnet iron oxide nanoparticles (IONPs) after systemic delivery. Our results show the signal intensity in the orthotopic mammary tumor in mouse that received NIR-830 dye labeled and uPAR-targeted IONPs is 10 times higher than that of the mouse injected with NIR-830 dye labeled and non-targeted mouse serum albumin (MSA)-IONPs.

Introduction

Theoretically, propagation of both excitation and fluorescent emission light in tissue is described by the coupled diffusion equations where the emission photon

density of the fluorophores is directly related to the excitation photon density, which in turn depends on the optical property distribution in tissue. Research conducted by several groups has shown the impact of optical property distribution^{97, 98, 101} and methods have been reported to improve image quality of FMT in the presence of heterogeneities FMT in phantom study.^{98, 103} FMT is already proved as a promising tool to track cancerous tissue in mice.^{4, 59} In these studies, inhomogeneities in tissue are usually treated by normalizing the excitation signal towards emission signal via normalized Born approximation method.¹⁰³ The normalized Born method uses original boundary data to minimize the error resulted from uniform optical property assumption. Heterogeneities of mouse can also be better evaluated for FMT reconstruction with a *priori* MRI or CT information.^{45, 130} To our best knowledge, whole body optical heterogeneities of mice are not systematically evaluated by directly using diffusion optical tomography. Diffusion equation based full optical property reconstruction can reveal information hidden in raw experimental data and further improve the FMT reconstruction. The resolution of the reconstructed heterogeneity is not as good as MRI or CT method, but DOT can directly reconstruct optical property and it is easily implemented into FMT system with zero extra cost, requiring only few extra minutes to regular FMT experimental procedure. Our method has proved be an efficient and practical method to improve FMT imaging reconstruction for both regular and arbitrarily shaped phantom experiments in presence of heterogeneous reduced scattering coefficient (μ'_s) and absorption coefficient (μ_a) distributions.^{28, 96} Here we first applied DOT guided FMT method and evaluate its performance in mice. To help evaluate the method qualitatively and quantitatively, we labeled the living 4T1 breast tumor cells with

amino-terminal fragment (ATF) peptides conjugated to Cy 5.5 dye and then injected different amount of tumor cell (100000,200000 and 500000) in three marked positions on the mouse. The results proved that with DOT guidance, tumor cell quantification and localization are both improved. We further applied proposed method to evaluate affinity and sensitive limit of a newly developed nanoparticle NIR-830 -ATF-IONP with tumor cell targeting amino-terminal fragment (ATF). The ATF modified dye and pure dye are injected in tail of live mouse induced with breast tumor. Based on DOT guided FMT results, the affinity of ATF modified dye toward tumor cell is increased ten folds. Further FMT test indicated that NIR-830 -ATF-IONP can localize trace amount of cancer tumor cells (recurrent tumor and metastasis cases).

Method and Experiments

Data acquisition and process procedure were described in detail in our previous phantom studies.^{28, 96} Briefly, for each angle, the source and detector nodes in the finite element mesh were automatically chosen to cover the region of interest and absolute coordinates of detectors were mapped automatically towards CCD pixel grid. For each angle, XY-positioner delivered laser beam according to coordinates of source positions in 3D finite mesh and CCD collected transmission signal of the opposite side. For example, in tumor cell quantification experiments, signals from a total of 238 source positions (corresponding about 60 per side in all 4 projections by rotating mouse 0,90,180 and 270 degree) and 284 detector positions on opposite side were collected. Mesh is generated according to the shape of the mice and we used a finite element mesh of 3855 nodes and 17999 tetrahedron elements.

3D DOT Reconstruction of Mice

Reconstructed optical property images of a typical mouse are given in Fig. 2 and isosurface is plotted using 70% of the maximum reconstructed value. The 3D absorption and scattering images show that the lung (upper part), and liver (lower part) are reconstructed with high absorption and scattering value.

We note that the accuracy of reconstructed absorption and scattering coefficient is critical for the DOT guided FMT method presented here. We have made great efforts in improving our DOT reconstruction algorithm and experimental system to obtain accurate optical property reconstruction. It has been demonstrated in recent years by several groups including our own⁹²⁻⁹⁵ that quantitative reconstruction of both absorption and scattering coefficients is possible using CW DOT when *a priori* information coupled with effective normalization schemes are used. In our CW DOT method, in addition to the use of *a priori* information and normalization scheme, the hybrid regularization schemes of Marquardt and Tikhonov play an important role in combating the ill-posed problem involved.⁸⁷ Our previous phantom study shows that with DOT guidance, statistically we can obtain better FMT reconstruction in mouse-mimicking phantom experiments.⁹⁶

Quantification of Cy 5.5 –ATF Labeled Tumor Cell

According to Beers' law, fluorophore absorption coefficient $\mu_{a_{x \rightarrow m}}$ is proportional to fluorophore concentration since quantum efficiency is stable at low concentration in most preclinical applications. In FMT reconstruction algorithm, $\mu_{a_{x \rightarrow m}}$ value is determined by light intensity distribution, optical heterogeneity distribution and boundary data, which are all related to heterogeneous absorption coefficient (μ_a) distributions and reduced

scattering coefficient (μ'_s) distributions. Since mice have highly heterogeneous optical property in different organs and tissues, same concentration of dye in different parts of mouse body will be reconstructed with different $\mu_{a_{x \rightarrow m}}$ value when optical property distributions are treated uniform. In addition, DOT reconstruction itself can provide additional information to reveal tumor position since high μ_a value correlates high blood volume which can result from angiogenesis of the late stage tumor and high μ'_s value reveal tumor with big particle size distribution since tumor cells/nuclei are considerably enlarged relative to normal ones.^{131, 132} Therefore, DOT reconstructed reduced scattering coefficient (μ'_s) and absorption coefficient (μ_a) distributions are introduced in our study to help obtain reliable quantitative analysis in FMT.

The recombinant amino terminal fragment (ATF) of uPA was produced from a bacterial expressing system using our established protocol ATF peptides were then labeled with Cy5.5 dye and used to label breast cancer 4T1 cells. After labeling, the intercellular dye and nonspecific binding are washed thoroughly. Cells were counted and specific numbers of cells (top:100,000 cells, middle:200,000, bottom:500,000) were injected into the haired Balb/C mouse for optical imaging. Experiments were conducted using a continuous wave (CW) diode laser at 660 nm (25mW) as excitation and 710 nm band pass filter for emission light acquisition.

The injected tumor shape may vary depending on the anatomic structure of the injection site but its volume is remained approximately same and proportional to tumor cell number. Isosurface of the reconstructed fluorophore absorption coefficient $\mu_{a_{x \rightarrow m}}$ is used to present the 3D reconstruction where the volume of the isosurface indicates the

tumor cell amount. The reconstructed tumor images are given in Fig. 3 where it can be seen that when the DOT recovered μ_a and μ'_s distributions are used, the fluorescence image is most accurately reconstructed in terms of the volume (which is proportional to tumor cell number) and position (partially overlapped with the exact position). We can also see that the uniform μ_a and μ'_s assumption results in unsatisfied

$\mu_{a_{x \rightarrow m}}$ reconstruction where the recovered target positions are shifted from the exact positions and the recovered sizes are not proportional to their tumor cell number. We also noticed that DOT guided FMT may somehow increase the sensitivity in tumor imaging, the 100,000 cells in up position is not revealed by FMT without DOT guidance.

Evaluation of Affinity

Oxy-hemoglobin and deoxy-hemoglobin have same absorption at about 790nm and the sum of absorption of oxy-hemoglobin and deoxy-hemoglobin reach minimum at about 800 nm in visible light region. We developed NIR-IR830-ATF-IONPs (excitation at 785nm and emission at 830nm) to improve preclinical mouse imaging quality. The NIR-830 dyes can yield much higher signal/noise ratios with less absorption than Cy 5.5, and is also much stable than indocyanine green (ICG). We here use DOT guided FMT to characterize NIR-830 dye-ATF-IONP, $\mu_{a_{x \rightarrow m}}$ is reconstructed by DOT guided FMT and is used to quantify affinity.

Quantification of the affinity in the mouse can improve specificity and facilitate probe development. Affinity are normally measured *in vitro* by using confocal scanning-laser microscopy, quartz crystal microbalance (QCM), atomic force microscopy (AFM) and surface plasmon resonance (SPR).¹³³⁻¹³⁵ Planar or FMT based whole body

monitoring methods are also reported.¹³⁶⁻¹³⁷ These methods usually can just provide qualitative or semi-quantitative analysis.

The affinity to targeted organs or tumors in the mouse is the key parameter to evaluate developed probe in preclinical applications. Although quantitative measurement of the adsorption kinetics and affinity in a live mouse is extremely challenging, the variation in affinity is the frequently used substitute index for most applications. We tentatively utilized FMT to quantify affinity of a newly developed NIR-830-ATF-IONP by comparing reconstructed $\mu_{a_{x \rightarrow m}}$ value of NIR-830 -IONP dye with and without ATF.

We administrated un-targeted NIR-830-MSA IONP and NIR-830 -ATF-IONP via the tail vein of the tumor-bearing mice, DOT guided FMT reconstruction, at the exact same measurement and reconstruction settings, was used. The ATF-targeting greatly increases the signal intensity in the tumors over non-targeted, NIR-830 dye-MSA-IONP with a difference over 10-fold as shown in Fig. 5-4.

The high specific affinity of NIR-830-ATF-IONPs can greatly increase the sensitivity thus makes challenging cases like early stage tumor, recurrent tumor and metastasis detectable. To confirm whether NIR-830-ATF-IONPs dye can help detect spontaneous recurrent tumors and lung metastasis of breast cancer, we excised the original breast cancer tumor. After the mouse recovered, both the planar fluorescent (IVIS system) and FMT measurement detected metastasis and recurrent tumor with consistent results.

Conclusions

DOT guided FMT can help to obtain more accurate quantitative and qualitative results in a well controlled tumor cell count experiment using Cy5.5-ATF nanoparticle dye. We further used the method to characterize NIR-830-ATF-IONPs nanoparticle dye developed by an established protocol¹³⁸. We tentatively evaluate the affinity with FMT, our study suggested that the affinity to tumor cell increased over 10 fold compared to NIR-830-IONP without ATF. Trace cancer cells in recurrent tumor and metastasis can be detected and FMT results are consistent with planar fluorescence imaging. Our results show that NIR-830-ATF-IONP is very suitable for preclinical cancer research. Its high specificity to tumor cell and stability after administration could help follow up pathology study, mark surgical margins more accurately and detect possible circulating cancer cells in blood; DOT guided quantitative FMT can be a promising tool in preclinical study such as fluorescent dye quality assess, tumor progression monitor, early stage cancer detection, chemotherapy evaluation and drug delivery.

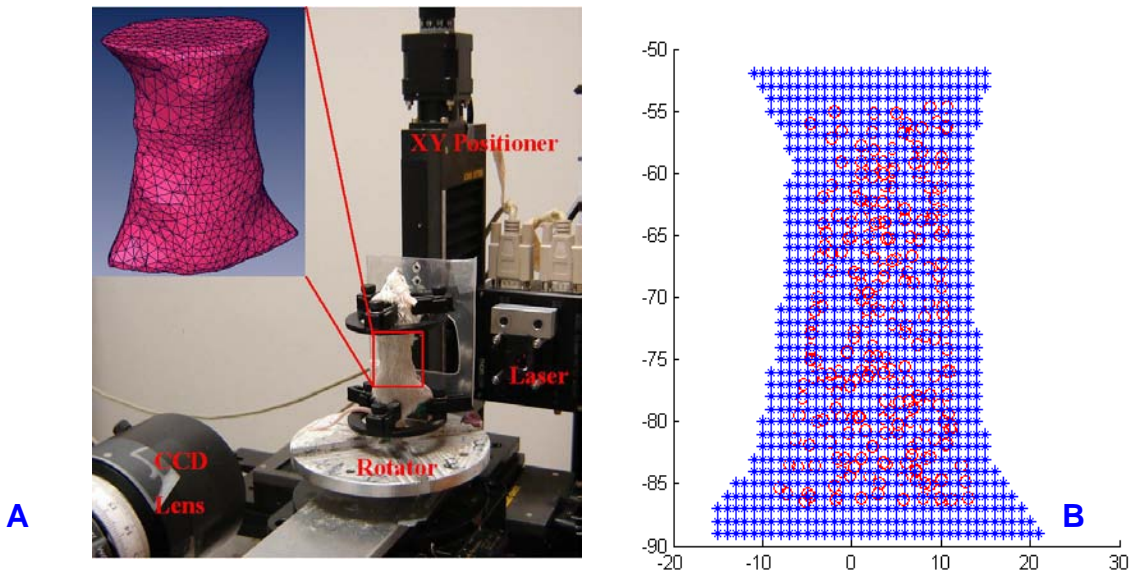


Figure 5-1. Mouse in Experiment. A) Photography of the experimental system, where the insert is the 3D finite element mesh of the mouse for the region of interest B) The detector node distribution of a typical sagittal projection. Blue stars are the voxel of 3D mouse model and red circles are the projected detector nodes on the finite element mesh used.

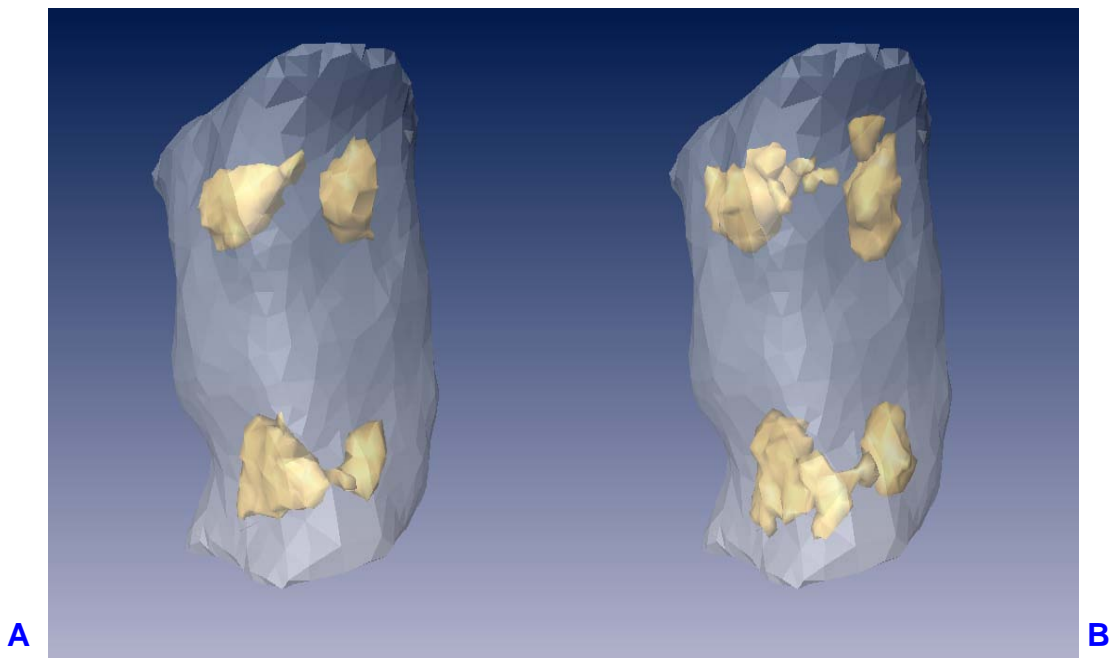


Figure 5-2. Reconstructed 3D μ_a and μ'_s images of a typical mouse (mm^{-1}): A) μ_a image

B) μ'_s image

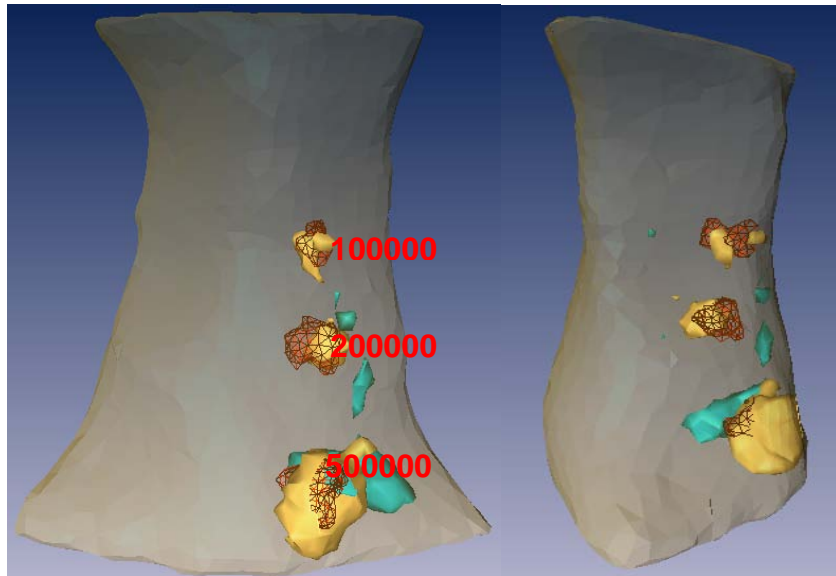


Figure 5-3. Recovered 3D FMT images from a mouse in sagittal A) and coronal projection B). The exact tumor location (red mesh), and the isosurface plot of the fluorescent target recovered with (in golden) and without (in green) DOT guidance are shown together for comparison.

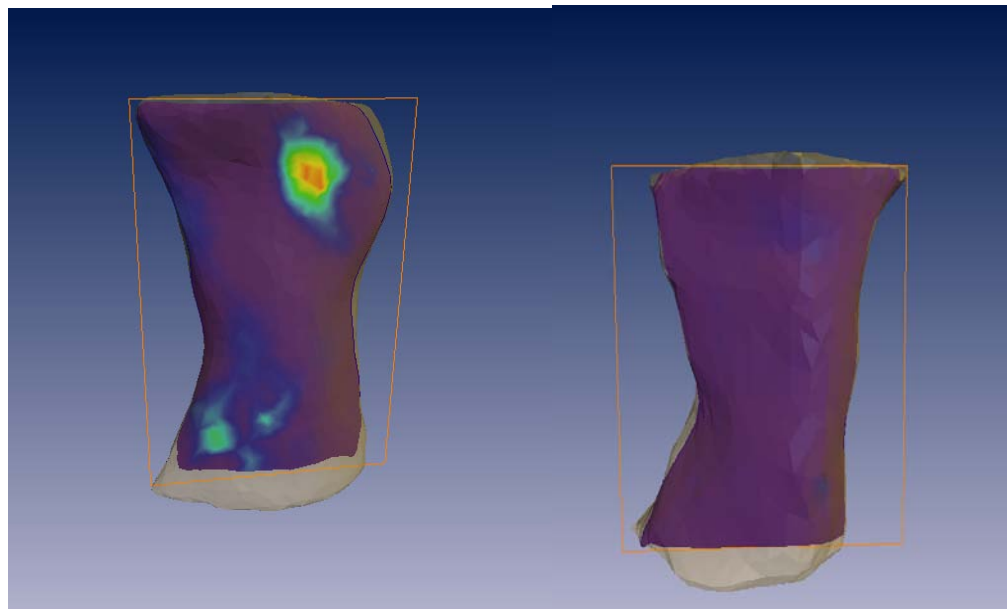


Figure 5-4. Comparison of signal intensity of the mammary tumor in the mice received uPAR-targeted NIR-830-ATF-IONPs and non-targeted NIR-830-MSA-IONP (with ATF vs without ATF). (A) Tail vein injection of 40 pmol of NIR-830-ATF-IONPs for 6 days (B) Tail vein injection of 40 pmol of NIR-830-MSA-IONPs for 6 days

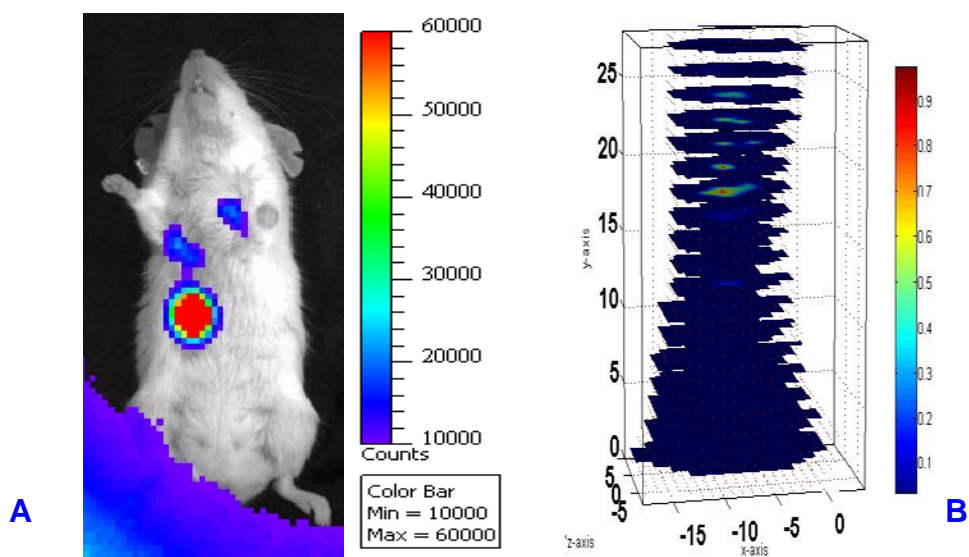


Figure 5-5. Detection of local recurrent mammary tumor and lung metastasis using reconstructed 3D images of FMT method and NIR-830-ATF peptide optical imaging probes. The primary tumor of the mouse was removed by surgery. Local recurrent tumor in the mammary fat pad and lung metastasis developed two weeks following surgery. The mouse received the tail vein delivery of 40 ug of NIR-830 ATF peptides for 72 hrs. Bioluminescence imaging showing the locations of the tumor lesions. (a) Planar fluorescent image by IVIS system. (b) Reconstructed 3D images by FMT method.

CHAPTER 6 APPLICATION IN A DROSOPHILA PUPA MODEL

Basic biologic research (e.g., genetics, epigenetics, and stem cells) often use animals such as *Drosophila*, zebrafish, and *xenopus laevis* as the study models of mesoscopic scale biological events. Characterization of molecular events in these models currently relies on time-consuming *in vitro* tissue-sectioning based microscopic techniques including fluorescence microscopy (~40 μ m depth), confocal microscopy (~200 μ m depth) and two- or multi-photon fluorescence microscopy (~500 μ m depth). In particular, the *in vitro* microscopic imaging can be performed only at certain fixed time points, making a dynamic characterization of cell events of the same animal impossible. In contrast, the emerging fluorescence molecular tomography (FMT) is capable of providing information about specific biological events of intact live animal in its natural state, and has already shown promises in imaging small animals such as mice with applications including cancer detection, drug discovery, and basic mechanism studies.

12, 13, 57, 59, 139, 140

Recently, Vinegoni *et al.* showed the possibility of *in vivo* tomographically imaging millimeter or mesoscopic scale animals where green fluorescent protein (GFP) expressing cells inside *Drosophila* pupae were imaged using a FMT approach based on Fermi simplification to the Fokker-Planck solution of photon transport theory. This simplified model is effective only in strongly forward-scattering regimes. In their study, this approximation was satisfied through the use of a polarizer to reject highly diffusive photons due to the relatively strong polarization property GFP contains, which allows to collect only 10% of the boundary photons.¹⁴¹

Compared to GFP, DsRed shows almost no polarization property since biexponential anisotropy decay reveals a fast ($211\pm 6\text{ps}$) depolarization in DsRed.^{142, 143} Thus polarization based method used for GFP is not applicable to the DsRed-bearing pupae we study here. The radiative transfer equation (RTE) is perfect to deal with such cases for mesoscopic fluorescence tomography and the RTE based FMT can be applied to imaging fluorescent dyes without polarization. In the RTE framework, since all boundary photons are collected, the laser power can be reduced to minimize possible damage the live millimeter scale animals.

Previously Klose *et al.*¹⁴⁴ implemented the RTE-based FMT reconstruction algorithm using finite difference method and demonstrated successful image reconstruction in a slab-like geometry phantom¹⁹ and *in vivo* mouse imaging in a match fluid filled slab-like container with finite difference method.¹⁴⁵ Amit Joshi *et al.*¹⁴⁶ presented the RTE-based fluorescence tomography on a computational mouse model to localize fluorophore concentration distribution. Our RTE based fluorescence reconstruction algorithm is implemented with finite element method for arbitrarily shaped objects. This algorithm is validated using a Cy5.5 dye containing-microtube embedded in a pupa. The RTE based algorithm is also tested using DsRed-bearing live pupae, and the reconstructed images are compared with images obtained from confocal microscopy.

In our platform, the FMT microscope was horizontally mounted, and the sample laid vertically on a rotation stage. A laser beam was focused to the horizontal scan positions on the pupa's surface with a plano-convex lens. The sample was rotated to collect signals from different angle and the fluorescent signals were captured with a

microscope lens mounted on a CCD camera. The vertical scanning of the laser beam was realized via a linear stage. The tomographically collected fluorescence measurements were then used to localize and quantify the signal from IRER{ubi-DsRed} through a radiative transfer equation based tomographic inverse algorithm.

Static Fluorophore Concentration Imaging

Cy5.5 Microtube Imaging

The FMT experimental system and data acquisition procedure were described in detail in our previous studies.^{28, 96} Briefly, the experiments were conducted using a continuous wave (CW) 660nm diode laser as excitation and 710nm band pass filter for emission light acquisition. The 3D shape of the pupa was obtained with volume carving method based on silhouettes of 72 projections.¹¹⁷ Signals from a total of 484 sources at 4 CCD positions and 484 detector positions at the opposite side of the source location were collected. The 3D experimental data was mapped to seven transverse slices and the 2D RTE based FMT algorithm was utilized for reconstruction.

A 3 mm long silica capillary microtube (outer diameter=150 μ m and inner diameter =100 μ m) containing Cy5.5 dye served as a target. The tube was inserted through the pupa as shown in Fig. 6-2 (a). The *Drosophila* pupa was positioned vertically on a rotation stage. Laser beam was focused to source point at the pupa's shell with a plano-convex lens. The sample was rotated to 4 projection positions and transmitted light were captured with a 1024x1024 pixels CCD camera.

Since an early stage pupa is composed of mostly fat tissue like larva, the optical properties of the pupae can then be assumed homogenous. The reconstructed FMT images (transverse slices) using both the diffusion and RTE based methods are given in Fig. 6-2b~6-2h. We see that strong boundary artifacts exist in all the images using the

diffusion-based method, while the RTE-based method shows overall much improved images. We also note that the images with the RTE based method (bottom row, Fig.6-2b~6-2h) give a target-localization error of up to 100 μ m. Fig.6-3 shows the 3D rendering of the reconstructed images obtained from these 7 transverse slices where the golden rod indicates the exact position and size of the Cy5.5-containing microtube.

DsRed Whole Body Imaging

Drosophila is a widely used model for genetic and molecular biology research. The genetic prowess of this organism allows florescent markers such as the DsRed gene to be readily inserted into interested loci as a reporter for various applications.^{147, 148} The pupa stage of *Drosophila* undergoes extensive tissue remodeling controlled by genetic cascade before it develops into an adult fruit fly. In our experiments, DsRed fluorescent reporter was inserted into the middle of IRER (Irradiation responsive enhancer region) and can only be expressed in IRER-open cells (Zhang *et al.* 2008). IRER is open in undifferentiated proliferating embryonic stem cells and is responsible for stress-induced cell death of these cells. Therefore, by monitoring the DsRed signal from different organs during development, we will be able to monitor the epigenetic status of IRER as well as follow some stem cell activities and events.¹⁴⁹

The *in vivo* experiments were conducted following exactly the same procedure as the Cy5.5 microtube experiments except that a 535nm CW diode laser was used as excitation and that a 585nm band pass filter was applied for emission light acquisition. Low laser power (6 μ W) was used during the 10 minute scanning for a full set of data collection (1 second CCD exposure time for each source position). We noticed that such a low laser power did not interrupt the undergoing biology development of the sample,

and that all the pupae were developed into normal fruit flies after the optical imaging. Confocal microscopy of certain slices from the pupae of same development stage were used to validate our reconstructed FMT results.

Fig.6-4 presents the FMT images for a typical day 2 pupa, in comparison with the confocal microscopy. In this figure, the first schematic shows the positions/sections corresponding to the FMT/confocal slices; the top row gives the FMT images, while the bottom row displays confocal microscope (bottom row a-d) and epifluorescence microscope (bottom row e & f) images. As can be seen, larger congregated DsRed-containing organs are clearly visualized (slices b and d). Major features in more complicated structure are also identifiable in the FMT images (slices a and c), although the FMT images are relatively blurred compared to the confocal images. Sagittal slices given in slices e and f were obtained through the interpolation using 9 transverse slices. We immediately note that the sagittal FMT images agree well with the corresponding images obtained from cryostat sections of fixed DsRed-expressing pupae.

Although it still needs to be verified by a tissue specific marker, it seems that at about 1 day post pupation (PP), the strong signal at the anterior corresponds to the degenerating salivary gland while the one at the posterior corresponds to the midgut. Signals from both regions were captured by the FMT images.

Dynamic DsRed Concentration Imaging

Epigenetic regulation, by limiting the accessibility of DNA and the expressivity of genes, plays a fundamental role in determining the differentiation potential of stem cells as well as the properties of differentiated cells. Deregulation of epigenetic status has been implicated in many diseases such as cancer, cardiovascular disorders, and mental diseases. In contrast to static genetic changes, epigenetic regulations are

dynamic, responsive to environmental and dietary factors, and under many circumstances, reversible. The dynamic nature of epigenetic regulation demands innovative techniques that allow continuous monitoring of epigenetic status in live animals. However, most biochemical methodologies for measuring epigenetic modification and DNA accessibility rely on homogenizing large amount of cells, which is inapplicable for monitoring dynamic epigenetic changes in live animals. In this study, we explored the applicability of using a fluorescent reporter, inserted into an epigenetically regulated region, in monitoring and semi-quantitative assessment of epigenetic status and DNA accessibility *in vivo*. Our analysis indicated that the expression of this *ubiquitin-DsRed* reporter accurately reflects the epigenetic status, i.e. the accessibility of DNA, in the tested locus. This reporter allowed us to monitor epigenetic changes of this locus during development as well as in response to histone modification compounds administrated with food. In addition, we showed that it is possible to semi-quantitatively measure DNA accessibility in live animals by measuring the fluorescence recovery after photobleaching.

Dynamic measurement of DNA accessibility in live animals via FMT.

Much cell death and proliferation occur during metamorphosis. However, the pupal shell is opaque and deflects the fluorescent signal, making it impossible for fluorescent microscopy to accurately localize and quantify the signal. To solve this problem, we have developed an initial platform for monitoring the dynamic signal from IRER {ubi-DsRed} using fluorescence molecular tomography (FMT).^{96, 150}

The main advantage of monitoring epigenetic change in live animals is that we could follow the dynamic epigenetic status during organism development, cellular differentiation and migration, and continuous response to environmental factors. To

interrogate if longitudinal observations would be possible, we followed the expression of IRRER{ubi-DsRed} over the whole pupation period (~115 hours in our setting as in Fig. 6-5) with recordings done at 2-15 hour interval. The relatively low energy required for FMT monitoring appeared to be well tolerated by the animal and did not disrupt the development process. Adult flies emerged from the pupal case at the end of recording without any noticeable defect. Repeated recordings of three pupae indicated that the dynamic pattern of IRRER{Ubi-DsRed} during pupation is highly repeatable (Fig. 6-7). The results are further confirmed by using microscope to image pupa whose shell is removed as in Fig. 6-6.

Fluorescence Recovery after Photobleaching (FRAP) and FMT

Much of the DsRed signal could be due to expression of the protein prior to the testing time. So the level of fluorescent signal monitored during development actually reflects the epigenetic status of the cell prior to the time of observation. To determine whether we could directly assay the status of epigenetic modification in live animals, we devised a scheme to monitor FRAP. Our initial data indicated that it is fully feasible to monitor the recovering of fluorescent signal, i.e. *de novo* synthesis of the reporter protein, in live animals using FRAP (bottom inlets in Fig. 6-7). The FRAP analysis was focused on the developing midgut in the posterior of the pupa, which has a very strong signal during early pupation. The overall signal in this area starts to increase at early pupation, reach its peak at about 30hr P.P. and starts to decline at about 80 hr P.P.. The FRAP analysis indicated that corresponding with the overall increase of the signal, the rate of FRAP is relatively faster at 14 hr P.P. (photobleaching done at 14 hr P.P., fluorescent signal is monitored up to 5 hour after bleaching). In contrast, FRAP was almost absent at 75 hr P.P., which is still 5 hrs prior to the precipitous decline of

fluorescent signal in this region. This result strongly suggests that FRAP measurements, in combination of monitoring overall fluorophore DsRed concentration by FMT, provide better measurement of DNA accessibility for region of interest at a given time point.

The relationship of FMT and FRAP can be further revealed with derivative FMT together with normalized FRAP in Fig. 6-8. Derivative FME indicates overall DsRed concentration change rate and normalized FRAP indicates regenerate speed proportionally to gene openings. The tendencies of two methods for salivary gland and the midgut almost overlap each other after subtracting 1.2 at 14 hour stage FRAB. The 1.2 difference is the sudden decrease of DsRed concentration which we think is due to a sudden increase in dying metabolism attributed to cell dying process naturally programmed to get rid of useless larva organ tissues and provide nutrition and space for new adult fruit fly organs at about 10% stage of pupation.

In summary, to realize *in vivo* monitoring of DsRed-expressing cell distribution In *Drosophila* pupae using fluorescence molecular tomography (FMT), the radiative transfer equation (RTE)-based FMT reconstruction algorithm is implemented using finite element method for mesoscopic millimeter scale imaging. The RTE algorithm is validated using both simulated and phantom experimental data. For the *in vivo* experiments, DsRed fluorescent reporter was inserted into the middle of IRER (Irradiation Responsive Enhancer Region) of *Drosophila* pupae and expressed only in IRER-open cells. Quantitatively accurate fluorescence images can be reconstructed from both simulated and phantom data. The *in vivo* images obtained agree well with the

in vitro images obtained from confocal microscopy both qualitatively and semi-quantitatively.

DsRed-bearing stem cells in *Drosophila* pupae can be markedly imaged using our FMT approach. Dynamic *in vivo* monitoring of biological events in mesoscopic scale animals can greatly facilitate basic biologic research such as genetics, epigenetic, and stem cells. Initial dynamic monitoring and FRAB are very promising in revealing epigenetic regulation activity during pupation, although much work lies ahead for us in order to further validate and develop the methodology.

Improvements are certainly needed especially with respect to the spatial resolution, data acquisition speed and experimental protocol. To enable cell level event monitoring, the resolution needs to be improved from the current 100 μ m to 10 μ m. Since the low resolution is most caused by scattering photons, techniques to capture early or less scattering photons^{40, 43} will provide much better boundary signal and higher resolution. High speed data acquisition will allow real-time dynamic monitoring of biologic events and can be implemented with fast Galvo scanner for light delivery and EMCCD for data collection, making a frame rate of 100 possible. Experimental protocol need to be improved for better statistic validity: the design of the reporter needs to be modified to minimize the impact of mRNA stability on FRAP analysis. The novel FMT&FRAP analysis needs to be carefully validated and improved with better resolution. Nonetheless, the *in vivo* monitoring of stem cells demonstrated in this thesis has paved the way for us to continually optimize our FMT method for improved performance.

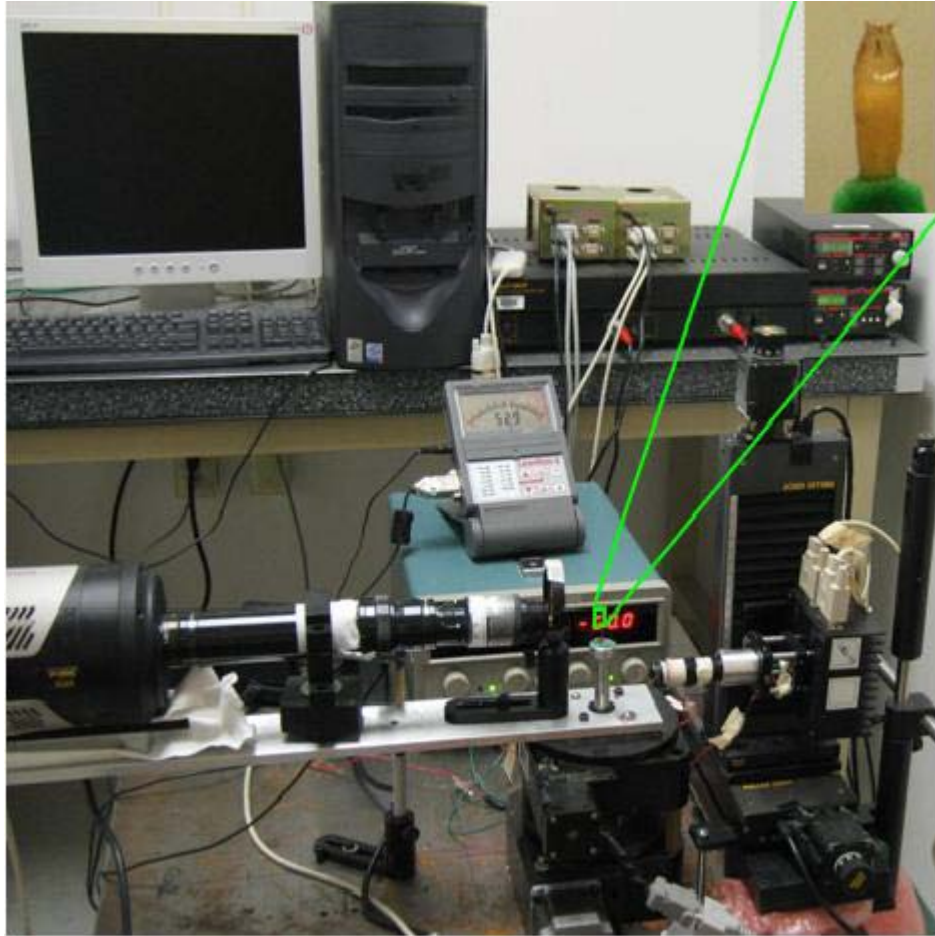


Figure 6-1. A pupa in experiment

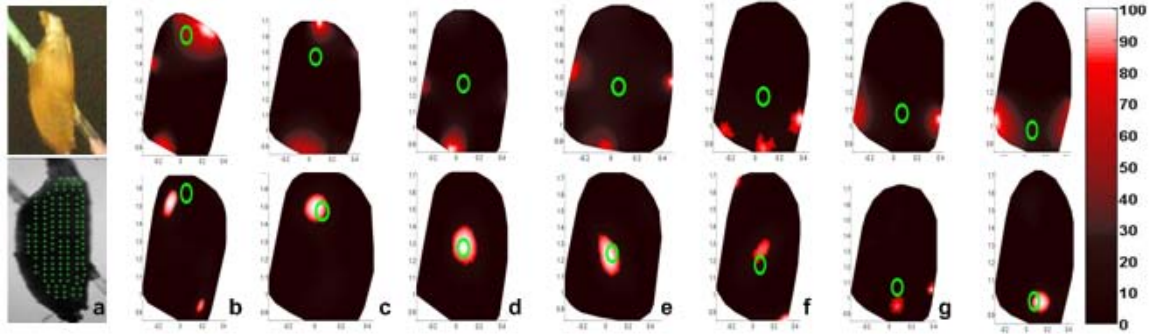


Figure 6-2. Comparative Cy5.5 tube experiment of the diffusion and RTE based FMT reconstruction for a microtube embedded pupa. a) Photograph of the pupa under test (top) and the source point/node distribution (green crosses) in coronal projection (bottom). (b)-(h): reconstructed FMT images for seven consecutive transverse slices with the diffusion based method (top row) and the RTE based method (bottom row). The green circle indicates the exact position of the dye-containing microtube.

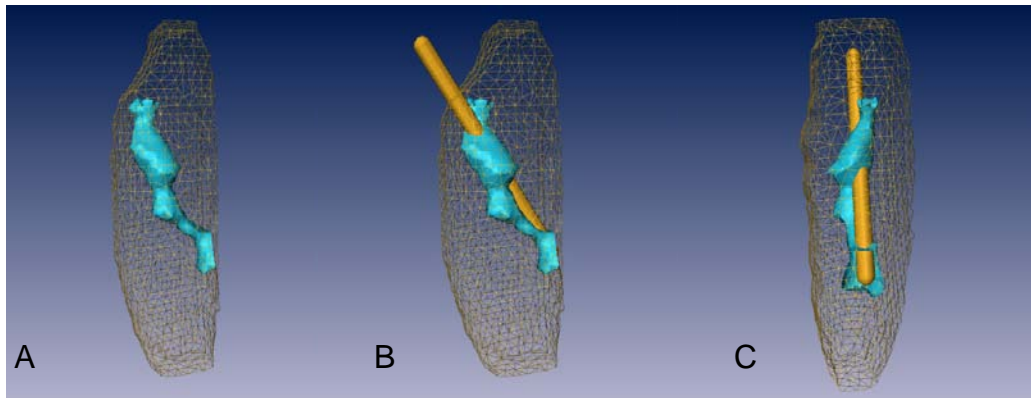


Figure 6-3. 3D view of reconstructed Cy 5.5 microtube in the pupa. A) reconstructed Cy5.5 dye-containing microtube in blue isosurface plot. B) reconstructed Cy5.5 dye-containing microtube (blue) and the exact position of the tube (golden). C) another view of the reconstructed Cy5.5 dye-containing microtube (blue) and the exact position of the tube (golden).

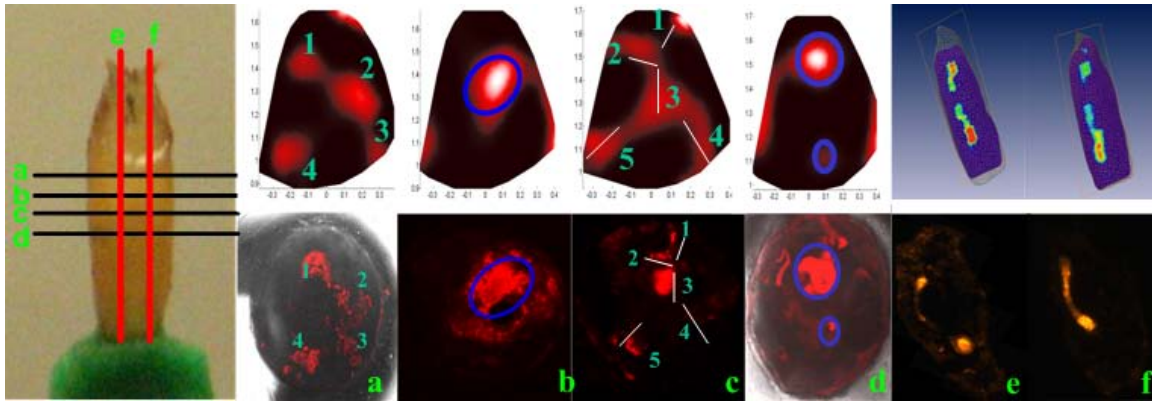


Figure 6-4. Reconstructed *in vivo* FMT (top row a-f) , *in vitro* confocal microscope (bottom row a-d) and epifluorescence microscope (bottom row e & f) images: Column a, b, c and d: transverse slices ; Column e and f : sagittal slices.

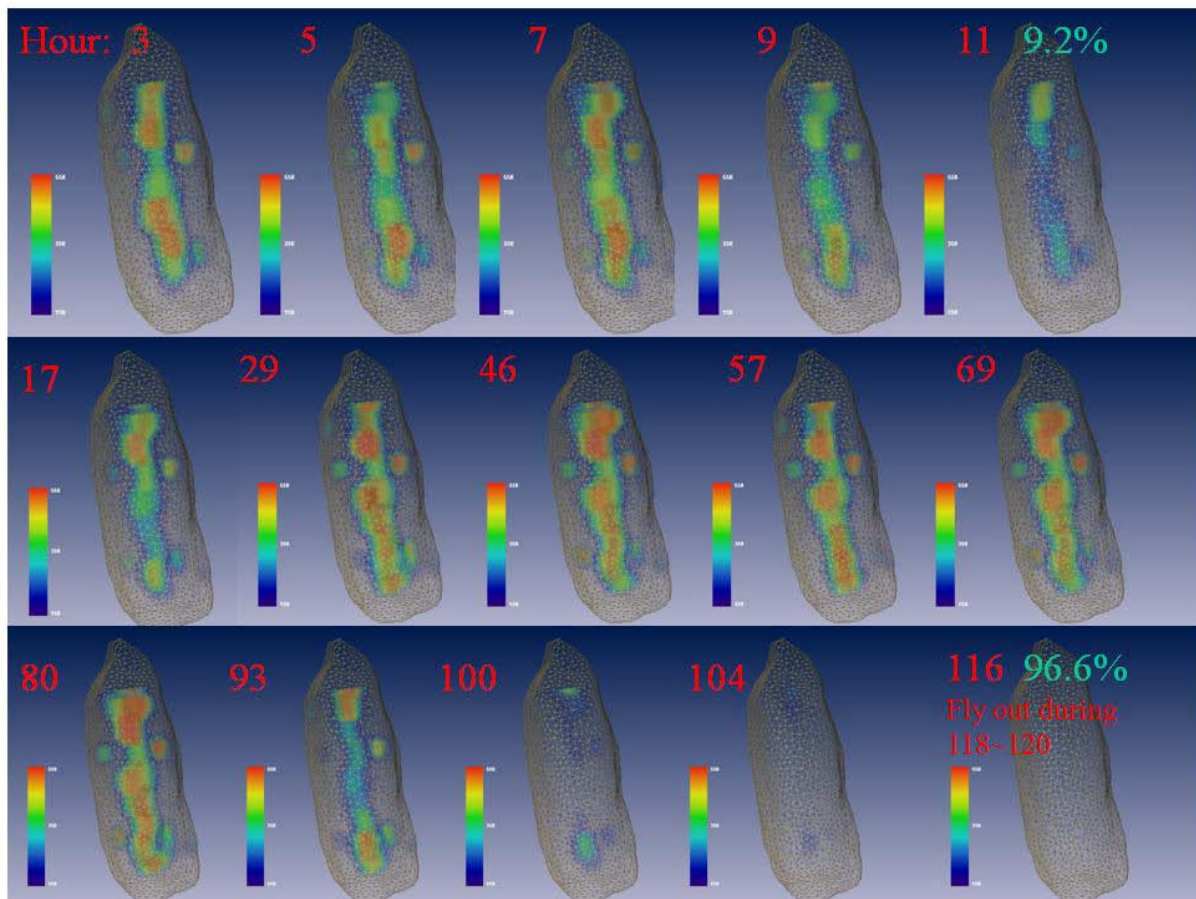


Figure 6-5. 3D FMT tomography of 15 stages during the pupation development.

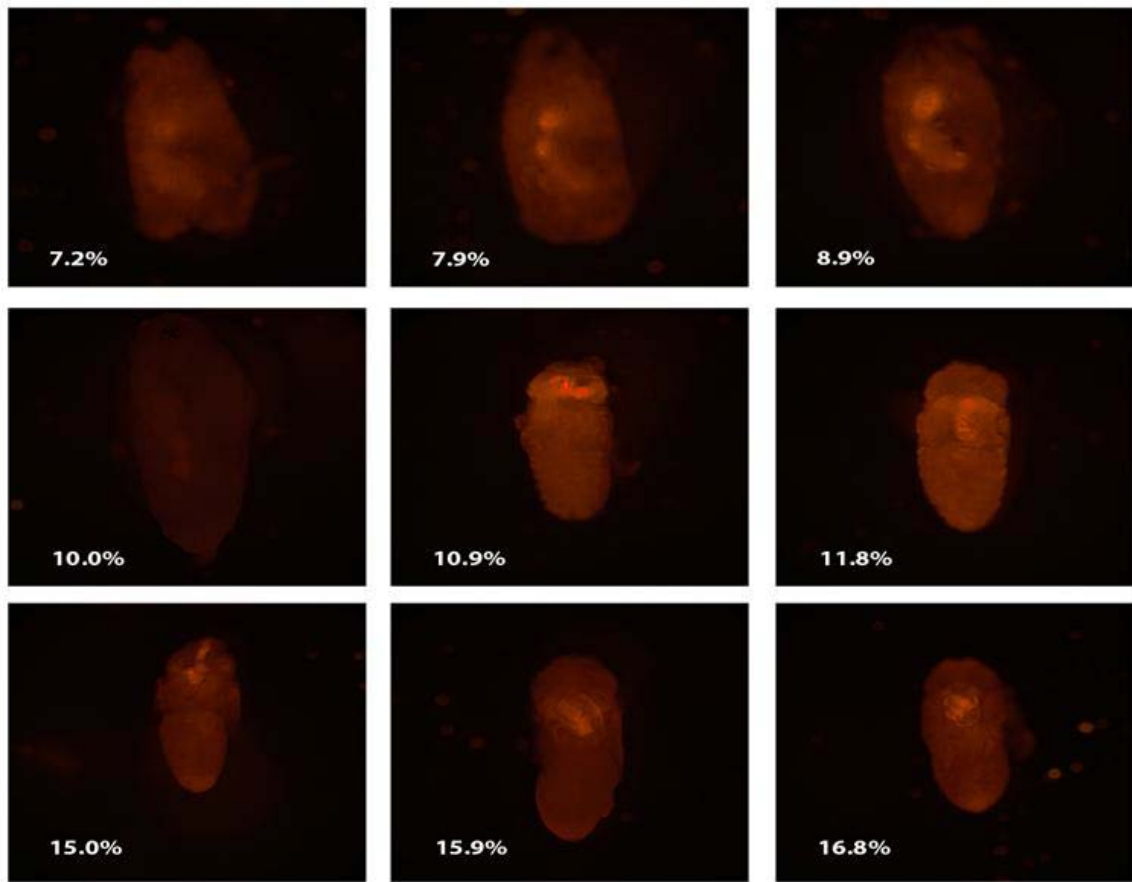


Figure 6-6. Microscope images of pupa (shell removed) in early stage. Sudden decrease in DsRed expressing at 10% stage is detected.

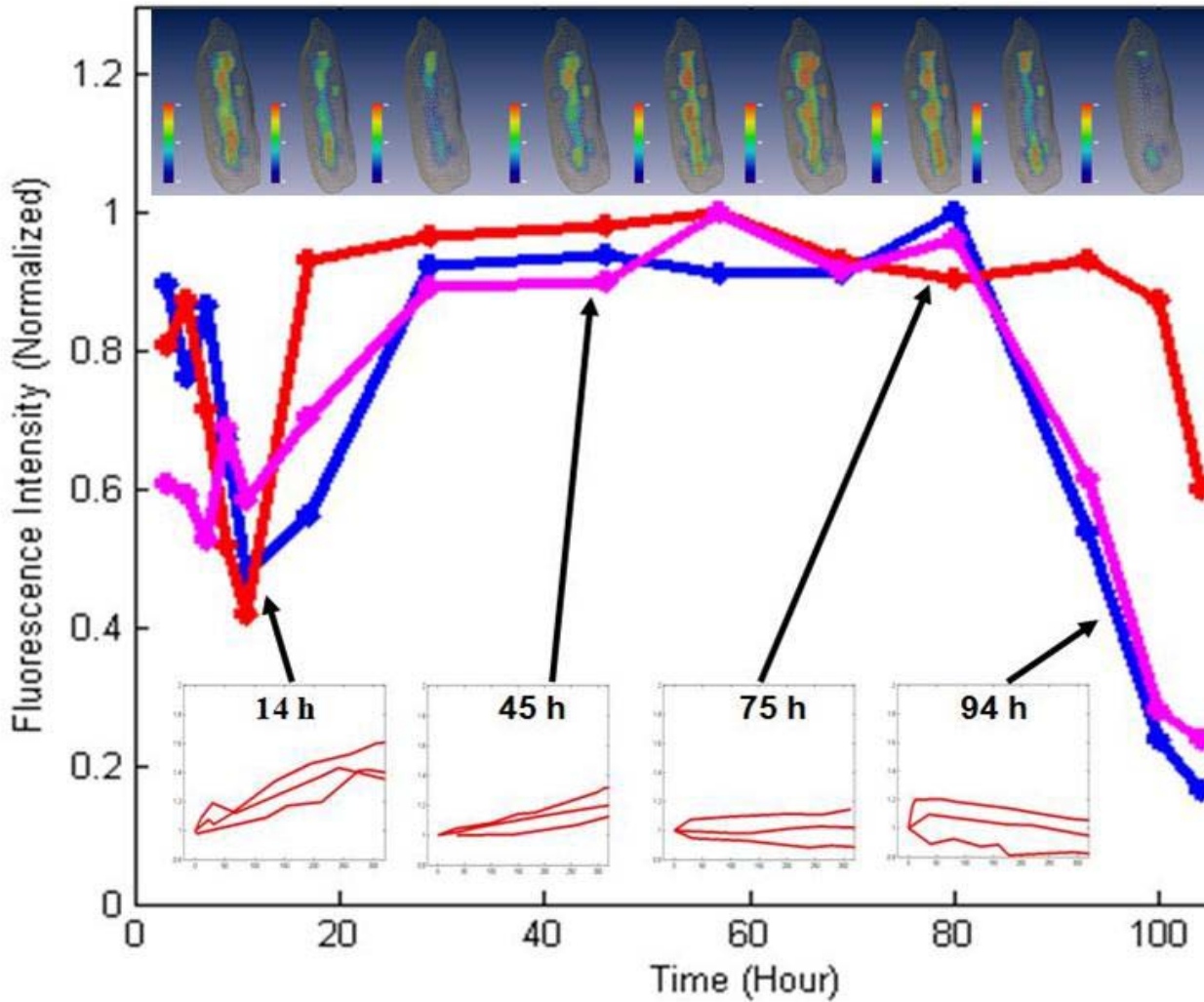


Figure 6-7. Quantifying the change of DNA accessibility in live animals with FMT and FRAP. The top insets are representative whole pupa constructions. The three lines represent the developmental change of signal level at the midgut region measured on three pupae. The insets below the lines are FRAP measurements performed at 14hr, 45hr, 75hr, and 94 hr post pupation (P.P.). For FRAP, each line represents an independent measurement on a different pupa at the same developmental stage (hours P.P.). FRAP measurements indicated that the region is already closed at about 75 hr P.P., even though the level of fluorescent signal did not start to decrease for another few hours.

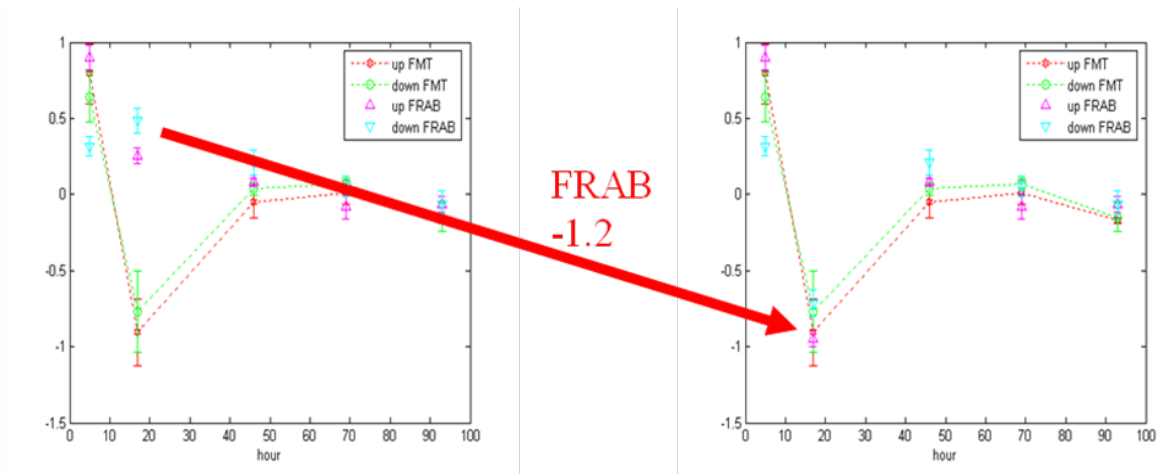


Figure 6-8. Correlation between derivative FMT together with normalized FRAP. For better comparison, the hour (x axis) are aligned and the value (y axis) are normalized. Actual sampling hour discrepancy between FMT and FRAB for each stage of five stages in plot is within ± 5 hours.

CHAPTER 7 CONCLUSIONS

In this thesis, DOT guided quantitative FMT are proposed: simulation test , experimental implementation and preclinical applications in both macro-scale and meso-scale samples are investigated. A quantitative 3D non contact FMT systems was built and continuously innovated during the investigation and it is capable of revealing dye distribution for macro-scale and meso-scale animals in their natural states. The workflow mainframe is described in Fig. 7-1.

To obtain full quantitative FMT, a DOT guided FMT approach is proposed. In this approach, reconstruction is conducted in both excitation and emission wavelength. Reconstruction in excitation wavelength can provide full optical heterogeneity information for quantitatively accurate FMT reconstruction. The simulation results in Chapter 2 and phantom experimental results in Chapter 4 show the improvement clearly. In Chapter 5, we also use our DOT guided FMT to evaluate the newly developed fluorescent dyes (NIR-830-MSA-IONP and Cy 5.5-ATF) which show great potential in accurately localizing tumor boundary to enable well defined excision region for tumor surgery. The reconstructed images in Chapter 5 also show good improvement in FMT with DOT guidance. Our study suggested that the affinity to tumor cell increased over 10 fold compared to NIR-830-MSA-IONP without ATF. Trace cancer cells in recurrent tumor and metastasis can be detected and FMT results are consistent with planar fluorescence imaging. Our results show that NIR-830-MSA-IONP nanoparticle is very suitable for preclinical cancer research. Its high specificity to tumor cell and stability after administration could help follow up pathology study, mark surgical margins more accurately and detect possible circulating cancer cells in blood; DOT guided quantitative

FMT proved be a promising tool in preclinical study such as tumor progression monitor, early stage cancer detection, chemotherapy evaluation and drug delivery.

This thesis proposed RTE based FMT reconstruction for meso-scale sample like *Drosophila* pupa. Light transportation within the object is described through two approaches (RTE and DA) according to the size of objects. In our *Drosophila* experiments, the distance between detector and source is less than 1mm so DA is no longer a good model. We implemented RTE based reconstruction and validate the method with simulation, Cy5.5 microtube experiments and DsRed dynamical monitoring experiments. The results we got in Chapter 6 shows that RTE based FMT is a good model for meso-scale animal study to provide dynamical semi-quantitative monitoring within 100 μ m localization error. The FMT image is validated by confocal microscope semi-quantitatively and qualitatively. To help study the stem cell activities, we also developed an *in vivo* Fluorescence Recovery After Photobleaching (FRAP) procedure and coordinate it with our dynamic FMT monitoring. Based on our monitoring of full developmental course of *Drosophila* pupa, we got consistent results from FRAP and RTE. There is a dramatic drop in *in vivo* FMT at 10% stage, and overall dynamic plot of FMT and FRAP are very consistent with each other. We also further confirm this phenomenon with upright fluorescent microscope. The sudden increase dying metabolism factor might be attributed to cell dying process naturally programmed to get rid of useless larva organ tissues and provide nutrition and space for developing new organs of adult fruit fly.

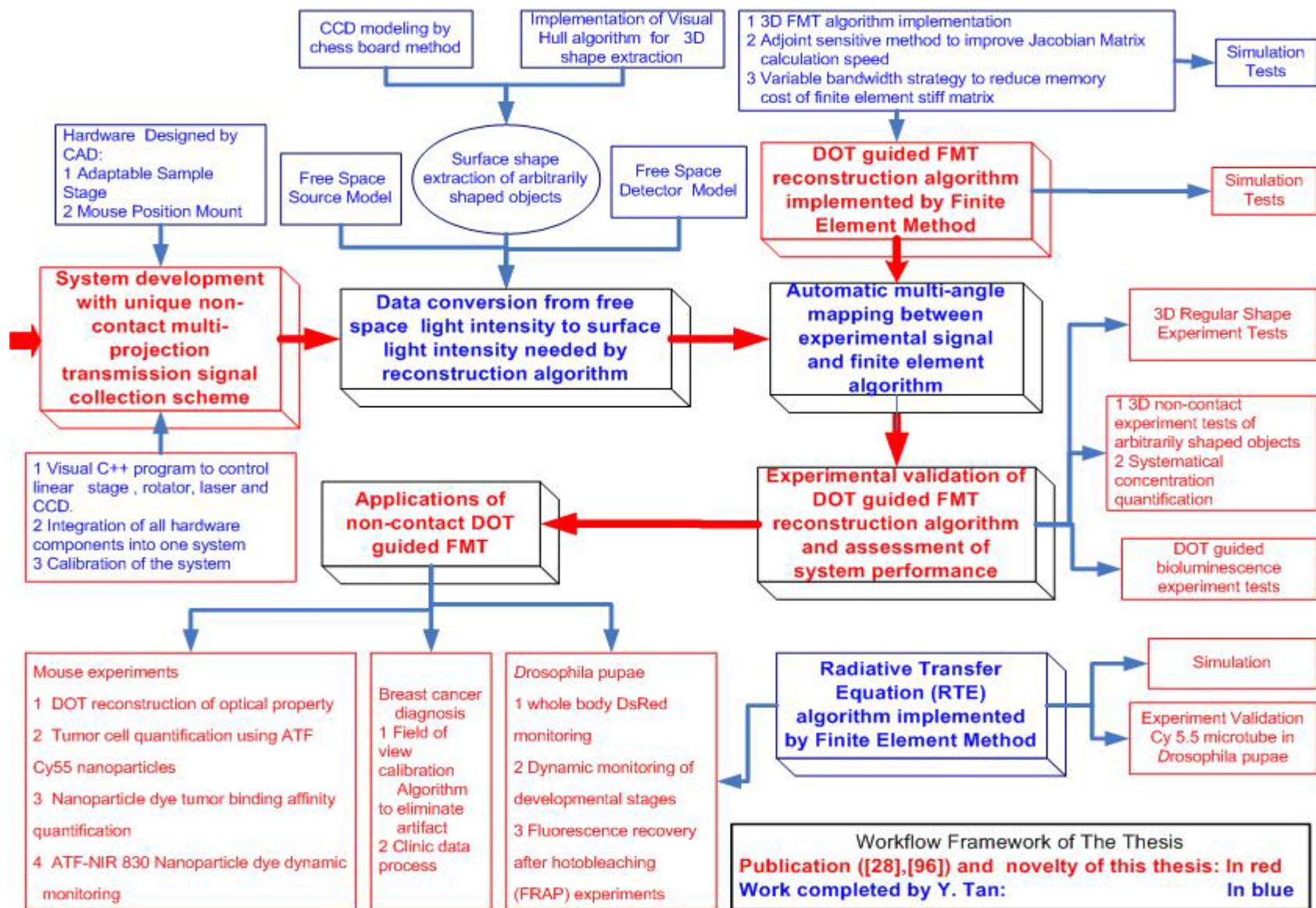


Figure 7-1. Workflow framework of the dissertation

LIST OF REFERENCES

1. J. Reynolds, T. Troy, R. Mayer, A. Thompson, D. Waters, K. Cornell, P. Snyder, and E. Sevick-Muraca, "Imaging of spontaneous canine mammary tumors using fluorescent contrast agents," *Photochem. Photobiol.* **70**, 87-94 (1999).
2. J. Grimm, D. G. Kirsch, S. D. Windsor, C. F. B. Kim, P. M. Santiago, V. Ntziachristos, T. Jacks, and R. Weissleder, "Use of gene expression profiling to direct *in vivo* molecular imaging of lung cancer," *P. Natl. Acad. Sci. USA.* **102**(40), 14404-14409 (2005).
3. A. Becker, C. Hennesius, K. Licha, B. Ebert, U. Sukowski, W. Semmler, B. Wiedenmann, and C. Grötzinger, "Receptor-targeted optical imaging of tumors with near-infrared fluorescent ligands," *Nat. Biotechnol.* **19**(4), 327-331 (2001).
4. X. Montet, J. L. Figueiredo, H. Alencar, V. Ntziachristos, U. Mahmood, and R. Weissleder, "Tomographic fluorescence imaging of tumor vascular volume in mice," *Radiology* **242**(3), 751-758 (2007).
5. H. Jiang, "Frequency-domain fluorescent diffusion tomography: a finite-element-based algorithm and simulations," *Appl. Optics.* **37**, 5337-5343 (1998).
6. J. Steinbrink, A. Liebert, H. Wabnitz, R. Macdonald, H. Obrig, A. Wunder, R. Bourayou, T. Betz, J. Klohs, and U. Lindauer, "Towards Noninvasive Molecular Fluorescence Imaging of the Human Brain," *Neurodegenerative Dis.* **5**(5), 296-303 (2008).
7. A. Corlu, R. Choe, T. Durduran, M. Rosen, M. Schweiger, S. Arridge, M. Schnall, and A. Yodh, "Three-dimensional *in vivo* fluorescence diffuse optical tomography of breast cancer in humans," *Opt. Express.* **15**(11), 6696-6716 (2007).
8. S. Roddaro, A. Fuhrer, C. Fasth, L. Samuelson, J. Xiang, and C. Lieber, "Strong g-Factor Anisotropy in Hole Quantum Dots Defined in Ge/Si Nanowires," *Arxiv. Pre.0706.2883* (2007).
9. P. Theer, M. Hasan, and W. Denk, "Two-photon imaging to a depth of 1000 m in living brains by use of a Ti: Al₂O₃ regenerative amplifier," *Opt. Lett.* **28**(12), 1022-1024 (2003).
10. L. Gao, R. Kester, and T. Tkaczyk, "Compact Image Slicing Spectrometer (ISS) for hyperspectral fluorescence microscopy," *Opt. Express* **17**, 12293-12308 (2009).
11. V. Ntziachristos, J. Ripoll, L. H. V. Wang, and R. Weissleder, "Looking and listening to light: the evolution of whole-body photonic imaging," *Nat. Biotechnol.* **23**(3), 313-320 (2005).

12. J. Rao, A. Dragulescu-Andrasi, and H. Yao, "Fluorescence imaging *in vivo*: recent advances," *Curr. Opin. Biotech.* **18**(1), 17-25 (2007).
13. F. Leblond, S. Davis, P. Valdés, and B. Pogue, "Pre-clinical whole-body fluorescence imaging: Review of instruments, methods and applications," *J Photoch. Photobio. B.* **98**(1), 77-94 (2010).
14. E. E. Graves, R. Weissleder, and V. Ntziachristos, "Fluorescence molecular imaging of small animal tumor models," *Curr. Mol. Med.* **4**(4), 419-430 (2004).
15. S. Arridge and J. Schotland, "Optical tomography: forward and inverse problems," *Arxiv. Pre.* 0907.2586 (2009).
16. A. S R, "The theoretical basis for the determination of optical pathlengths in tissue: temporal and frequency analysis," *Phys. Med. Biol* **37**(7), 1531-1560 (1992).
17. S. Arridge, M. Schweiger, M. Hiraoka, and D. Delpy, "A finite element approach for modeling photon transport in tissue," *Med. Phys.* **20**, 299-309 (1993).
18. S. Arridge and M. Schweiger, "Photon-measurement density functions. Part 2: Finite-element-method calculations," *Appl. Optics.* **34**(34), 8026-8037 (1995).
19. A. Klose, V. Ntziachristos, and A. Hielscher, "The inverse source problem based on the radiative transfer equation in optical molecular imaging," *J Comput Phys.* **202**(1), 323-345 (2005).
20. J. Culver, R. Choe, M. Holboke, L. Zubkov, T. Durduran, A. Slomp, V. Ntziachristos, B. Chance, and A. Yodh, "Three-dimensional diffuse optical tomography in the parallel plane transmission geometry: Evaluation of a hybrid frequency domain/continuous wave clinical system for breast imaging," *Med. Phys.* **30**, 235-247 (2003).
21. K. Ren, G. Abdoulaev, G. Bal, and A. Hielscher, "Algorithm for solving the equation of radiative transfer in the frequency domain," *Opt. Lett.* **29**(6), 578-580 (2004).
22. J. Ripoll and V. Ntziachristos, "Iterative boundary method for diffuse optical tomography," *J Opt. Soc. AM A.* **20**(6), 1103-1110 (2003).
23. E. Aydin, C. De Oliveira, and A. Goddard, "A comparison between transport and diffusion calculations using a finite element-spherical harmonics radiation transport method," *Med. Phys.* **29**, 2013-2023 (2002).
24. V. Markel, "Modified spherical harmonics method for solving the radiative transport equation," *Waves in Random and Complex Media* **14**(1), 13-19 (2004).

25. A. Klose, "The forward and inverse problem in tissue optics based on the radiative transfer equation: A brief review," *J Quant. Spect. Rad. Trans.* **111**(11) 1852-1853 (2010)
26. V. Ntziachristos and R. Weissleder, "Experimental three-dimensional fluorescence reconstruction of diffuse media by use of a normalized Born approximation," *Opt. Lett.* **26**(12), 893-895 (2001).
27. C. Vinegoni, D. Razansky, J. L. Figueiredo, M. Nahrendorf, V. Ntziachristos, and R. Weissleder, "Normalized Born ratio for fluorescence optical projection tomography," *Opt. Lett.* **34**(3), 319-321 (2009).
28. Y. Tan and H. Jiang, "Diffuse optical tomography guided quantitative fluorescence molecular tomography," *Appl. Opt.* **47**(12), 2011-2016 (2008).
29. R. Sevick-Muraca, "Truncated Newton's optimization scheme for absorption and fluorescence optical tomography: Part I theory and formulation," *Opt. Express* **4**, 353-371 (1999).
30. R. Sevick-Muraca, "Truncated Newton's optimization scheme for absorption and fluorescence optical tomography: Part II Reconstruction from synthetic measurements," *Opt. Express* **4**, 372-382 (1999).
31. M. Eppstein, D. Dougherty, D. Hawrysz, and E. Sevick-Muraca, "Three-dimensional Bayesian optical image reconstruction with domain decomposition," *IEEE. T. Med. Imaging.* **20**(3), 147-163 (2001).
32. M. Eppstein, D. Hawrysz, A. Godavarty, and E. Sevick-Muraca, "Three-dimensional, Bayesian image reconstruction from sparse and noisy data sets: near-infrared fluorescence tomography," *P. Natl. Acad. Sci. USA.* **99**(15), 9619 (2002).
33. A. Godavarty, E. Sevick-Muraca, and M. Eppstein, "Three-dimensional fluorescence lifetime tomography," *Med. Phys.* **32**, 992-1000 (2005).
34. V. Ntziachristos, J. P. Culver, and B. W. Rice, "Small-animal optical imaging," *J Biomed Opt.* **13**(1), 011001 (2008).
35. V. Ntziachristos, E. Graves, R. Schultz, and J. Ripoll, "Fluorescence molecular tomography: New detection schemes for acquiring high information content measurements," *I. S. Biomed. Imaging.* **2** 1475-1478 (2004).
36. V. Ntziachristos, E. A. Schellenberger, J. Ripoll, D. Yessayan, E. Graves, A. Bogdanov, L. Josephson, and R. Weissleder, "Visualization of antitumor treatment by means of fluorescence molecular tomography with an annexin V-Cy5.5 conjugate," *P. Natl. Acad. Sci. USA.* **101**(33), 12294-12299 (2004).

37. R. Roy, A. Thompson, A. Godavarty, and E. Sevick-Muraca, "Tomographic fluorescence imaging in tissue phantoms: a novel reconstruction algorithm and imaging geometry," *IEEE. T. Med. Imaging.* **24**(2), 137-154 (2005).
38. G. M. Turner, G. Zacharakis, A. Soubret, J. Ripoll, and V. Ntziachristos, "Complete-angle projection diffuse optical tomography by use of early photons," *Opt. Lett.* **30**(4), 409-411 (2005).
39. G. M. Turner, A. Soubret, and V. Ntziachristos, "Inversion with early photons," *Med. Phys.* **34**(4), 1405-1411 (2007).
40. M. J. Niedre, R. H. de Kleine, E. Aikawa, D. G. Kirsch, R. Weissleder, and V. Ntziachristos, "Early photon tomography allows fluorescence detection of lung carcinomas and disease progression in mice *in vivo*," *P. Natl. Acad. Sci. USA.* **105**(49), 19126-19131 (2008).
41. E. Hillman, O. Bernus, E. Pease, M. Bouchard, and A. Pertsov, "Depth-resolved optical imaging of transmural electrical propagation in perfused heart," *Opt. Express* **15**(26), 17827-17841 (2007).
42. E. Hillman, D. Boas, A. Dale, and A. Dunn, "Laminar optical tomography: demonstration of millimeter-scale depth-resolved imaging in turbid media," *Opt. Lett.* **29**(14), 1650-1652 (2004).
43. L. Florescu, J. Schotland, and V. Markel, "Single-scattering optical tomography," *Phys. Rev. E.* **79**(3), 36607 (2009).
44. D. Hogemann, V. Ntziachristos, L. Josephson, and R. Weissleder, "High throughput magnetic resonance imaging for evaluating targeted nanoparticle probes," *Bioconjugate. Chem.* **13**(1), 116-121 (2002).
45. M. Niedre and V. Ntziachristos, "Elucidating structure and function *in vivo* with hybrid fluorescence and magnetic resonance imaging," *P. IEEE.* **96**(3), 382-396 (2008).
46. D. E. Sosnovik, M. Nahrendorf, N. Deliolanis, M. Novikov, E. Aikawa, L. Josephson, A. Rosenzweig, R. Weissleder, and V. Ntziachristos, "Fluorescence tomography and magnetic resonance imaging of myocardial macrophage infiltration in infarcted myocardium *in vivo*," *Circulation* **115**(11), 1384-1391 (2007).
47. D. Hyde, R. de Kleine, S. A. MacLaurin, E. Miller, D. H. Brooks, T. Krucker, and V. Ntziachristos, "AOI987:Hybrid FMT-CT imaging of amyloid-beta plaques in a murine Alzheimer's disease model," *Neuroimage* **44**(4), 1304-1311 (2009).
48. D. Hyde, R. Schulz, D. Brooks, E. Miller, and V. Ntziachristos, "Performance dependence of hybrid x-ray computed tomography/fluorescence molecular

- tomography on the optical forward problem," J Opt. Soc. AM A. **26**(4), 919-923 (2009).
49. M. Nahrendorf, E. Keliher, B. Marinelli, P. Waterman, P. Feruglio, L. Fexon, M. Pivovarov, F. Swirski, M. Pittet, and C. Vinegoni, "Hybrid PET-optical imaging using targeted probes," P. Natl. Acad. Sci. USA. **107**(17), 7910-7915 (2010)
 50. D. Razansky and V. Ntziachristos, "Hybrid photoacoustic fluorescence molecular tomography using finite-element-based inversion," Med. Phys. **34**(11), 4293-4301 (2007).
 51. D. Razansky, C. Vinegoni, and V. Ntziachristos, "Multispectral photoacoustic imaging of fluorochromes in small animals," Opt. Lett. **32**(19), 2891-2893 (2007).
 52. D. Razansky, C. Vinegoni, and V. Ntziachristos, "Imaging of mesoscopic-scale organisms using selective-plane optoacoustic tomography," Phys. Med. Biol. **54**(9), 2769-2777 (2009).
 53. P. Bandettini, "What's new in neuroimaging methods?," Ann. NY. Acad. Sci. **1156**, 260-293 (2009).
 54. N. Blow, "*In vivo* molecular imaging: the inside job," Nat. Methods. **6**(6), 465-469 (2009).
 55. J. Frangioni, "*In vivo* near-infrared fluorescence imaging," Curr. Opin. Chem. Biol. **7**(5), 626-634 (2003).
 56. B. Giepmans, S. Adams, M. Ellisman, and R. Tsien, "The fluorescent toolbox for assessing protein location and function," Sci. Signaling **312**(5771), 217-224 (2006).
 57. K. Licha and C. Olbrich, "Optical imaging in drug discovery and diagnostic applications," Advanced drug delivery reviews **57**(8), 1087-1108 (2005).
 58. T. Misgeld and M. Kerschensteiner, "*In vivo* imaging of the diseased nervous system," Nat. Rev. Neurosci. **7**(6), 449-463 (2006).
 59. N. C. Deliolanis, J. Dunham, T. Wurdinger, J. L. Figueiredo, B. A. Tannous, and V. Ntziachristos, "*In-vivo* imaging of murine tumors using complete-angle projection fluorescence molecular tomography," J Biomed Opt. **14**(3), 030509 (2009).
 60. J. Baeten, J. Haller, H. Shih, and V. Ntziachristos, "*In Vivo* Investigation of Breast Cancer Progression by Use of an Internal Control," Neoplasia **11**(3), 220-227 (2009).
 61. X. Montet, V. Ntziachristos, J. Grimm, and R. Weissleder, "Tomographic fluorescence mapping of tumor targets," Cancer. Res. **65**(14), 6330-6336 (2005).

62. H. K. Choi, D. Yessayan, H. J. Choi, E. Schellenberger, A. Bogdanov, L. Josephson, R. Weissleder, and V. Ntziachristos, "Quantitative analysis of chemotherapeutic effects in tumors using *in vivo* staining and correlative histology," *Cell. Oncol.* **27**(3), 183-190 (2005).
63. C. Bremer, V. Ntziachristos, B. Weitkamp, G. Theilmeier, W. Heindel, and R. Weissleder, "Optical imaging of spontaneous breast tumors using protease sensing 'Smart' optical probes," *Invest Radiol.* **40**(6), 321-327 (2005).
64. E. A. Schellenberger, A. Bogdanov, A. Petrovsky, V. Ntziachristos, R. Weissleder, and L. Josephson, "Optical imaging of apoptosis as a biomarker of tumor response to chemotherapy," *Neoplasia* **5**(3), 187-192 (2003).
65. C. Bremer, M. Mustafa, A. Bogdanov, V. Ntziachristos, A. Petrovsky, and R. Weissleder, "Steady-state blood volume measurements in experimental tumors with different angiogenic burdens - A study in mice," *Radiology* **226**(1), 214-220 (2003).
66. C. B. Bremer, M. Mustafa, A. A. Bogdanov, V. Ntziachristos, A. Petrovsky, and R. Weissleder, "Steady-state blood volume measurements in experimental tumors with differing angiogenic burden," *Radiology* **225**, 632-633 (2002).
67. K. Licha, B. Riefke, V. Ntziachristos, A. Becker, B. Chance, and W. Semmler, "Hydrophilic cyanine dyes as contrast agents for near-infrared tumor imaging: Synthesis, photophysical properties and spectroscopic *in vivo* characterization," *Photochem. Photobiol.* **72**(3), 392-398 (2000).
68. O. Veisoh, C. Sun, C. Fang, N. Bhattarai, J. Gunn, F. Kievit, K. Du, B. Pullar, D. Lee, and R. Ellenbogen, "Specific targeting of brain tumors with an optical/magnetic resonance imaging nanoprobe across the blood-brain barrier," *Cancer. Res.* **69**(15), 6200-6207 (2009).
69. D. Abi-Haidar and T. Olivier, "Confocal reflectance and two-photon microscopy studies of a songbird skull for preparation of transcranial imaging," *J Biomed Opt.* **14**, 034038 (2009).
70. J. Klohs, M. Grafe, K. Graf, J. Steinbrink, T. Dietrich, D. Stibenz, P. Bahmani, G. Kronenberg, C. Harms, and M. Endres, "*In vivo* imaging of the inflammatory receptor CD40 after cerebral ischemia using a fluorescent antibody," *Stroke* **39**(10), 2845-2852 (2008).
71. A. Liebert, H. Wabnitz, H. Obrig, R. Erdmann, M. Moeller, R. Macdonald, H. Rinneberg, A. Villringer, and J. Steinbrink, "Non-invasive detection of fluorescence from exogenous chromophores in the adult human brain," *Neuroimage* **31**(2), 600-608 (2006).
72. T. Austin, "Optical tomography of the neonatal brain," *Eur. Radiol.* **17**, 2926-2933 (2007).

73. D. Kepshire, S. Davis, H. Dehghani, K. Paulsen, and B. Pogue, "Reflect depth experiment 2D better than 3D Fluorescence tomography characterization for sub-surface imaging with protoporphyrin IX," *Opt. Express* **16**(12), 8581-8593 (2008).
74. Y. Xu, H. Graber, and R. Barbour, "Image correction algorithm for functional three-dimensional diffuse optical tomography brain imaging," *Appl. Opt.* **46**(10), 1693-1704 (2007).
75. U. Netz, A. Scheel, A. Klose, A. Hielscher, and J. Beuthan, "Optical tomography in the diagnosis of rheumatoid arthritis—method and implementation," *Med. Laser Appl.* **22**(1), 15-22 (2007).
76. Z. Yuan, Q. Zhang, E. Sobel, and H. Jiang, "Three-dimensional diffuse optical tomography of osteoarthritis: initial results in the finger joints," *J Biomed Opt.* **12**, 034001 (2007).
77. U. Mahmood and R. Weissleder, "Near-infrared optical imaging of proteases in cancer," *Mol. Cancer. Ther.* **2**(5), 489-496 (2003).
78. S. Shen, Y. Chiou, J. Wang, M. Yen, R. Lee, C. Lai, and C. Chang, "Diffusion-weighted single-shot echo-planar imaging with parallel technique in assessment of endometrial cancer," *AM. J. Roentgenol.* **190**(2), 481-488 (2008).
79. A. Klose, U. Netz, J. Beuthan, and A. Hielscher, "Optical tomography using the time-independent equation of radiative transfer—Part 1: Forward model," *J Quant. Spect. Rad. Trans.* **72**(5), 691-713 (2002).
80. C. Wu, H. Barnhill, X. Liang, Q. Wang, and H. Jiang, "A new probe using hybrid virus-dye nanoparticles for near-infrared fluorescence tomography," *Opt. Commun.* **255**(4-6), 366-374 (2005).
81. H. Jiang, K. Paulsen, U. Osterberg, B. Pogue, and M. Patterson, "Optical image reconstruction using frequency-domain data: simulations and experiments," *J Opt. Soc. AM A.* **13**(2), 253-266 (1996).
82. J. Heino, S. Arridge, J. Sikora, and E. Somersalo, "Anisotropic effects in highly scattering media," *Phys. Rev. E.* **68**(3), 31908 (2003).
83. J. Tervo and P. Kolmonen, "Data fitting model for the kernel of integral operator from radiation therapy," *Math. Comp. Model.* **28**(3), 59-77 (1998).
84. N. Qatanani, A. Barham, and Q. Heeh, "Existence and uniqueness of the solution of the coupled conduction-radiation energy transfer on diffuse-gray surfaces," *Srvy. In Math. Appl.* **2**, 43-58 (2007).
85. T. Tarvainen, M. Vauhkonen, V. Kolehmainen, and J. Kaipio, "Hybrid radiative-transfer-diffusion model for optical tomography," *Appl. Optics.* **44**(6), 876-886 (2005).

86. G. Kanschat, "A robust finite element discretization for radiative transfer problems with scattering," *E. W. J. Numer. Math.* **6**, 265-272 (1998).
87. N. Iftimia and H. Jiang, "Quantitative optical image reconstruction of turbid media by use of direct-current measurements," *Appl. Optics.* **39**(28), 5256-5261 (2000).
88. G. Sleijpen, H. Vorst, and D. Fokkema, "BiCGstab (l) and other hybrid Bi-CG methods," *Numer. Algorithms.* **7**(1), 75-109 (1994).
89. F. Fedele, J. Laible, and M. Eppstein, "Coupled complex adjoint sensitivities for frequency-domain fluorescence tomography: theory and vectorized implementation," *J Comput. Phys.* **187**(2), 597-619 (2003).
90. M. Patterson and B. Pogue, "Mathematical model for time-resolved and frequency-domain fluorescence spectroscopy in biological tissues," *Appl. Optics.* **33**(10), 1963-1974 (1994).
91. E. Sevick-Muraca, G. Lopez, J. Reynolds, T. Troy, and C. Hutchinson, "Fluorescence and absorption contrast mechanisms for biomedical optical imaging using frequency-domain techniques," *Photochem. Photobiol.* **66**(1), 55-64 (1997).
92. A. Scheel, M. Backhaus, A. Klose, B. Moa-Anderson, U. Netz, K. Hermann, J. Beuthan, G. Müller, G. Burmester, and A. Hielscher, "First clinical evaluation of sagittal laser optical tomography for detection of synovitis in arthritic finger joints," *Ann. Rheum. Dis.* **64**(2), 239-245 (2005).
93. A. Li, Q. Zhang, J. Culver, E. Miller, and D. Boas, "Reconstructing chromosphere concentration images directly by continuous-wave diffuse optical tomography," *Opt. Lett.* **29**(3), 256-258 (2004).
94. Y. Xu, X. Gu, T. Khan, and H. Jiang, "Absorption and scattering images of heterogeneous scattering media can be simultaneously reconstructed by use of dc data," *Appl. Optics.* **41**(25), 5427-5437 (2002).
95. Y. Pei, H. Graber, and R. Barbour, "Normalized-constraint algorithm for minimizing inter-parameter crosstalk in DC optical tomography," *Appl. Opt.* **35**, 3963-3978 (1996).
96. Y. Tan and H. Jiang, "DOT guided fluorescence molecular tomography of arbitrarily shaped objects," *Med Phys* **35**(12), 5703-5707 (2008).
97. V. Ntziachristos, A. Hielscher, A. Yodh, and B. Chance, "Diffuse optical tomography of highly heterogeneous media," *IEEE Trans. Med. Imaging* **20**(6), 470-478 (2001).

98. R. Roy, A. Godavarty, and E. Sevick-Muraca, "Fluorescence-enhanced optical tomography using referenced measurements of heterogeneous media," *IEEE Trans. Med. Imaging* **22**(7), 824-836 (2003).
99. A. Sahu, R. Roy, A. Joshi, and E. Sevick-Muraca, "Evaluation of anatomical structure and non-uniform distribution of imaging agent in near-infrared fluorescence-enhanced optical tomography," *Opt. Express*. **13**(25), 10182-10199 (2005).
100. J. Rolland and H. Barrett, "Effect of random background inhomogeneity on observer detection performance," *J Opt. Soc. AM A*. **9**(5), 649-658 (1992).
101. A. Milstein, S. Oh, K. Webb, C. Bouman, Q. Zhang, D. Boas, and R. Millane, "Fluorescence optical diffusion tomography," *Appl. Optics*. **42**(16), 3081-3094 (2003).
102. E. Shives, Y. Xu, and H. Jiang, "Fluorescence lifetime tomography of turbid media based on an oxygen-sensitive dye," *Opt. Express*. **39**, 5256-5261 (2000).
103. A. Soubret, J. Ripoll, and V. Ntziachristos, "Accuracy of fluorescent tomography in the presence of heterogeneities: Study of the normalized born ratio," *IEEE Trans. Med. Imaging* **24**(10), 1377-1386 (2005).
104. L. Hervé, A. Koenig, A. Da Silva, M. Berger, J. Boutet, J. Dinten, P. Peltié, and P. Rizo, "Noncontact fluorescence diffuse optical tomography of heterogeneous media," *Appl. Optics*. **46**(22), 4896-4906 (2007).
105. C. Li and H. Jiang, "A calibration method in diffuse optical tomography," *Journal of Optics A: Pure and Appl. Optics*. **6**, 844-852 (2004).
106. R. Tsai, "A versatile camera calibration technique for high-accuracy 3D machine vision metrology using off-the-shelf TV cameras and lenses," *Radiometry*, 221-244 (1992).
107. C. Harris and M. Stephens, "A combined corner and edge detector," 1988.
108. N. Ahuja and J. Veenstra, "Generating octrees from object silhouettes in orthographic views," *IEEE. T Pattern. Anal.* 137-149 (1989).
109. A. Laurentini, "The visual hull concept for silhouette-based image understanding," *IEEE. T Pattern. Anal.* 150-162 (1994).
110. J. Hasenfratz, M. Lapierre, J. Gascuel, and E. Boyer, "Real-time capture, reconstruction and insertion into virtual world of human actors," *Vis., Video. . Graph. Conf.* 49-56 (2003).
111. W. Matusik, C. Buehler, and L. McMillan, "Polyhedral visual hulls for real-time rendering," *Eur. Workshop.Rend.*, 115-125 (2001).

112. W. Matusik, C. Buehler, R. Raskar, S. Gortler, and L. McMillan, "Image-based visual hulls," Proc. of the 27th Ann. Conf. on Comp. Graph. Inter. Tech. 369-374 (2000).
113. J. Carranza, C. Theobalt, M. Magnor, and H. Seidel, "Free-viewpoint video of human actors," ACM. T. Graphic. **22** 569-577 (2003).
114. R. B. Schulz, J. Ripoll, and V. Ntziachristos, "Noncontact optical tomography of turbid media," Opt. Lett. **28**(18), 1701-1703 (2003).
115. R. B. Schulz, J. Ripoll, and V. Ntziachristos, "Experimental fluorescence tomography of tissues with noncontact measurements," IEEE. T. Med. Imaging. **23**(4), 492-500 (2004).
116. J. Ripoll, R. B. Schulz, and V. Ntziachristos, "Free-space propagation of diffuse light: Theory and experiments," Physical Review Letters **91**(10),103901 (2003).
117. A. Mulayim, U. Yilmaz, and V. Atalay, "Silhouette-based 3-D model reconstruction from multiple images," IEEE. Trans. Sys. Man Cyber. **33**(4), 582-591 (2003).
118. Z. Zhang, "A flexible new technique for camera calibration," IEEE. T Pattern. Anal. **22**(11), 1330-1334 (2000).
119. H. Zhao, F. Gao, Y. Tanikawa, K. Homma, and Y. Yamada, "Time-resolved diffuse optical tomographic imaging for the provision of both anatomical and functional information about biological tissue," Appl. Optics. **44**(10), 1905-1916 (2005).
120. D. Razansky and V. Ntziachristos, "Hybrid photoacoustic fluorescence molecular tomography using finite-element-based inversion," Med. Phys. **34**, 4293-4301 (2007).
121. A. Serdaroglu, B. Yazici, and V. Ntziachristos, "Fluorescence molecular tomography based on a priori information." Biomed. Opt. Conf. SH46 (2006)
122. X. Song, J. Yi, and J. Bai, "A parallel reconstruction scheme in fluorescence tomography based on contrast of independent inversed absorption properties," I. J. Bio. Imaging. **2006**, 1-7 (2006).
123. H. Van Staveren, C. Moes, J. van Marie, S. Prahl, and M. van Gemert, "Light scattering in Intralipid-10% in the wavelength range of 400-1100 nm," Appl. Optics. **30**(31), 4507-4514 (1991).
124. E. Hull, M. Nichols, and T. Foster, "Quantitative broadband near-infrared spectroscopy of tissue-simulating phantoms containing erythrocytes," Phys. Med. Biol. **43**, 3381-3404 (1998).

125. S. Flock, S. Jacques, B. Wilson, W. Star, and M. van Gemert, "Optical properties of Intralipid: a phantom medium for light propagation studies," *Lasers in Surg. Med.* **12**, 510-519 (1992).
126. M. Landsman, G. Kwant, G. Mook, and W. Zijlstra, "Light-absorbing properties, stability, and spectral stabilization of indocyanine green," *J Appl. Physiology.* **40**(4), 575-583 (1976).
127. R. Philip, A. Penzkofer, W. Bäumlner, R. Szeimies, and C. Abels, "Absorption and fluorescence spectroscopic investigation of indocyanine green," *J Photoch. Photobio. B.* **96**(1-3), 137-148 (1996).
128. B. Yuan, N. Chen, and Q. Zhu, "Emission and absorption properties of indocyanine green in Intralipid solution," *J Biomed Opt.* **9**, 497-503 (2004).
129. G. Wang, W. Cong, K. Durairaj, X. Qian, H. Shen, P. Sinn, E. Hoffman, G. McLennan, and M. Henry, "*In vivo* mouse studies with bioluminescence tomography," *Biomed. Eng* **4**, 235-260 (2002).
130. Y. Lin, W. Barber, J. Iwanczyk, W. Roeck, O. Nalcioglu, and G. Gulsen, "Quantitative fluorescence tomography using a combined tri-modality FT/DOT/XCT system," *Opt. Express.* **18**(8), 7835-7850 (2010).
131. J. Mourant, A. Hielscher, A. Eick, T. Johnson, and J. Freyer, "Evidence of intrinsic differences in the light scattering properties of tumorigenic and nontumorigenic cells," *Cancer. Cytopathol.* **84**(6), 366-374 (1998).
132. A. Cerussi, D. Jakubowski, N. Shah, F. Bevilacqua, R. Lanning, A. Berger, D. Hsiang, J. Butler, R. Holcombe, and B. Tromberg, "Spectroscopy enhances the information content of optical mammography," *J Biomed Opt.* **7**, 60-71 (2002).
133. H. Van Genderen, H. Kenis, P. Lux, L. Ungeth, C. Maassen, N. Deckers, J. Narula, L. Hofstra, and C. Reutelingsperger, "*In vitro* measurement of cell death with the annexin A5 affinity assay," *Nat. Protoc.* **1**(1), 363-367 (2006).
134. C. Tamerler, E. Oren, M. Duman, E. Venkatasubramanian, and M. Sarikaya, "Adsorption kinetics of an engineered gold binding peptide by surface plasmon resonance spectroscopy and a quartz crystal microbalance," *Langmuir* **22**(18), 7712-7718 (2006).
135. M. C. Weiger, J. J. Park, M. D. Roy, C. M. Stafford, A. Karim, and M. L. Becker, "Quantification of the binding affinity of a specific hydroxyapatite binding peptide," *Biomaterials* **31**(11), 2955-2963 (2010).
136. X. Yang, C. Shi, R. Tong, W. Qian, H. Zhau, R. Wang, G. Zhu, J. Cheng, V. Yang, and T. Cheng, "Near IR Heptamethine Cyanine Dye-Mediated Cancer Imaging," *Clin. Cancer. Res.* **16**(10), 2833-2844 (2010)

137. J. Baeten, J. Haller, H. Shih, and V. Ntziachristos, "*In vivo* investigation of breast cancer progression by use of an internal control," *Neoplasia* (New York, NY) **11**(3), 220-227 (2009).
138. L. Yang, X. Peng, Y. Wang, X. Wang, Z. Cao, C. Ni, P. Karna, X. Zhang, W. Wood, X. Gao, S. Nie, and H. Mao, "Receptor-Targeted Nanoparticles for *In Vivo* Imaging of Breast Cancer," *Clin. Cancer Res.* **15**(14), 4722-4732 (2009).
139. N. C. Deliolanis, R. Kasmieh, T. Wurdinger, B. A. Tannous, K. Shah, and V. Ntziachristos, "Performance of the red-shifted fluorescent proteins in deep-tissue molecular imaging applications," *J Biomed Opt.* **13**(4), 044008 (2008).
140. C. McCann, P. Waterman, J. Figueiredo, E. Aikawa, R. Weissleder, and J. Chen, "ProSense: Combined magnetic resonance and fluorescence imaging of the living mouse brain reveals glioma response to chemotherapy," *Neuroimage* **45**(2), 360-369 (2009).
141. C. Vinegoni, C. Pitsouli, D. Razansky, N. Perrimon, and V. Ntziachristos, "*In vivo* imaging of *Drosophila melanogaster* pupae with mesoscopic fluorescence tomography," *Nat. Methods.* **5**(1), 45-47 (2008).
142. A. Heikal, S. Hess, G. Baird, R. Tsien, and W. Webb, "Molecular spectroscopy and dynamics of intrinsically fluorescent proteins: coral red (dsRed) and yellow (Citrine)," *P. Natl. Acad. Sci. USA.* **97**(22), 11996-12001 (2000).
143. M. Garcia-Parajo, M. Koopman, E. Van Dijk, V. Subramaniam, and N. Van Hulst, "The nature of fluorescence emission in the red fluorescent protein DsRed, revealed by single-molecule detection," *P. Natl. Acad. Sci. USA.* **98**(25), 14392-14397 (2001).
144. A. Klose and A. Hielscher, "Fluorescence tomography with simulated data based on the equation of radiative transfer," *Opt. Lett.* **28**(12), 1019-1021 (2003).
145. A. Hielscher, "Optical tomographic imaging of small animals," *Curr. Opin. Biotech.* **16**(1), 79-88 (2005).
146. A. Joshi, J. Rasmussen, E. Sevick-Muraca, T. Wareing, and J. McGhee, "Radiative transport-based frequency-domain fluorescence tomography," *Phys. Med. Biol.* **53**, 2069-2088 (2008).
147. D. Grover, J. Yang, D. Ford, S. Tavaré, and J. Tower, "Simultaneous tracking of movement and gene expression in multiple *Drosophila melanogaster* flies using GFP and DsRED fluorescent reporter transgenes," *BMC Res. Notes.* **2**(1), 58 (2009).
148. Y. Wang, Y. John, and S. Chien, "Fluorescence proteins, live-cell imaging, and mechanobiology: seeing is believing," *Annu. Rev. Biomed. Eng.* **10**, 1-38 (2008).

149. Y. Zhang, N. Lin, P. Carroll, G. Chan, B. Guan, H. Xiao, B. Yao, S. Wu, and L. Zhou, "Epigenetic blocking of an enhancer region controls irradiation-induced proapoptotic gene expression in *Drosophila* embryos," *Dev. Cell.* **14**(4), 481-493 (2008).
150. C. Vinegoni, C. Pitsouli, D. Razansky, N. Perrimon, and V. Ntziachristos, "*In vivo* imaging of *Drosophila melanogaster* pupae with mesoscopic fluorescence tomography," *Nat Methods* **5**(1), 45-47 (2008).

BIOGRAPHICAL SKETCH

Yiyong Tan got a Bachelor of Engineering (2000) and Master of Engineering (2003) in precision instrument engineering in Wuhan University, China. He later studied at University of Utah, USA and got Master of Science in bioanalytical chemistry (2005). Yiyong Tan began his Ph.D. program in biomedical engineering department of University of Florida in 2005 and worked on fluorescence molecular tomography for the past five years and he expects to obtain his Ph.D. degree in the end of 2010.